# METHODS FOR PROCESSING 3D IMAGES FOR BREAST MORPHOLOGY

---

A Dissertation Presented to

the Faculty of the Department of Computer Science

University of Houston

---

In Partial Fulfillment

of the Requirements for the Degree

Doctor of Philosophy

---

By

Lijuan Zhao

May 2015

**METHODS FOR PROCESSING 3D IMAGES FOR BREAST MORPHOLOGY**


Lijuan Zhao


APPROVED:

Dr. Fatima A. Merchant, Chair
Dept. of Engineering Technology
Dept. of Computer Science

Dr. Shishir K. Shah
Dept. of Computer Science

Dr. Gregory P. Reece, MD
The Univ. of Texas MD Anderson Cancer Center

Dr. Jaspal S. Subhlok
Dept. of Computer Science

Dr. Edgar Gabriel
Dept. of Computer Science

Dean, College of Natural Sciences and Mathematics

# Acknowledgements

I would first like to thank my advisors Prof. Fatima A. Merchant and Prof. Shishir K. Shah. They have been supportive of my Ph.D. process from very beginning to the end point. They have always provided constructive suggestions on my research.

I really appreciate Dr. Gregory P. Reece for his great help in my research, especially in my understanding medical concepts correctly. He has been more than a member of my dissertation committee.

Many thanks are given to my dissertation committee Prof. Edgar Gabriel and Prof. Jaspal S. Subhlok for their advice and suggestions on my doctoral research.

This work was supported by a NIH grant 1R01CA143190-01A1 (PI: Mia K. Markey). The 3D images used in this research were generously provided by the Department of Plastic Surgery at The University of Texas MD Anderson Cancer Center and stored in the database which is maintained by the Biomedical Informatics Laboratory (BMIL) at The University of Texas at Austin. I would like to give my thanks to Prof. Mia K. Markey's BMIL team and Dr. Michelle C. Fingeret's team in the Department of Behavioral Science at the University of Texas MD Anderson Cancer Center to provide me the demographic and characteristic information of patients.

# METHODS FOR PROCESSING 3D IMAGES FOR BREAST MORPHOLOGY

An Abstract of a Dissertation
Presented to
the Faculty of the Department of Computer Science
University of Houston

In Partial Fulfillment
of the Requirements for the Degree
Doctor of Philosophy

By
Lijuan Zhao
May 2015

# Abstract

In this research, two novel algorithms are developed to facilitate quantitative evaluation of breast aesthetics for preoperative planning and postoperative outcome assessment in breast reconstruction surgery in cancer patients. First, an algorithm is presented for registering 3D images of individual patients from multiple clinical visits. Registration is performed to eliminate differences in object coordinate systems between images due to variations in patient positioning and posture, thereby facilitating longitudinal comparison of morphological changes in the reconstructed breasts. Second, an algorithm to detect from 3D images the lowest breast contour, an important attribute for breast aesthetics, is presented. The algorithm allows detection of the lowest breast contour, for ptosis grades of 0, 1, 2, and 3. Most importantly, the algorithm operates independent of the presence of fiducial points such as the nipple, making it robust for applicability to images of breasts at intermediate time points during reconstructive surgery that are devoid of nipples.

The applicability of the two algorithms is demonstrated in a multi-view 3D data fusion technique for visualization of the inframammary fold (IMF) in upright images from women with ptotic breasts. The IMF, a critical landmark for breast surgery and morphometry, is typically occluded for ptotic breasts in upright images, which is conventionally used for evaluation of breast aesthetics. Multi-view 3D images taken at two different positions (upright and supine) are employed in a data fusion approach to superimpose the IMF position, on 3D images of women with ptotic breasts wherein only the lowest breast contour is visible.

Contributions of this research: (1) The registration algorithm is more effective

for multiple-visit images than traditional registration methods. This algorithm outperforms existing ICP algorithms and is robust to variations in body mass index (BMI). (2) The lowest breast contour detection algorithm, which computes contours in 3D images directly, is more effective than current methods, which detect contours in 2D images. (3) Multi-view 3D data fusion technique is a first attempt to visualize the IMF in upright images for women with ptotic breasts, which enables physicians to visualize the IMF position in upright images of women with high breast ptosis degrees ($\geq 2$).

# Contents

# List of Figures

# List of Tables

# Chapter 1

# Introduction

## 1.1 General Introduction

Breast reconstruction is an important surgical component for many women undergoing breast cancer treatment [1]. Breast cancer remains one of the most common malignancies in women and is one of the leading causes of cancer-related mortality. Despite the current emphasis on breast conservation, mastectomy rates remain at 30%. Mastectomy is often associated with significant psychological stress due to distorted body image. The purpose of breast reconstruction is to recreate a breast form that is satisfying to the patient, facilitating her psychosocial adjustment to living as a breast cancer survivor [2, 3].

Breast reconstructive surgery encompasses a range of surgeries performed immediately after mastectomy, or as separate procedures at a later date. The reconstructed breast can be formed using a breast tissue expander/implant [4, 5], autologous tissue [6] (i.e., living tissue from another part of the patient), or a combination of the two. In addition, surgical modifications are typically made to both breasts, even if only one breast had cancer, in order to maintain a symmetrical appearance. Thus, breast reconstruction is a complex process usually not achieved in a single procedure, and can take up to a year or longer, depending on the type of reconstructive procedures selected and other factors affecting surgical outcome, including postoperative complications and adjuvant cancer treatment.

Breast aesthetic assessment plays an important role in evaluating the final outcome of breast reconstruction surgery. Subjective, qualitative assessment of breasts morphology is measured by human observers. This methodology is primarily based on the evaluator's experience and his/her visual assessment and evaluation. The main problem of subjective and qualitative assessment is that it has inherent low inter- and intra-rater agreement which decreases the accuracy of breast aesthetic measurement. A quantitative assessment, direct anthropometry, is performed on the patient's body using a measuring tape which is both time consuming and invasive to patients. Photogrammetry involves measurements on two-dimensional (2D) clinical photographs which is less invasive. However, 2D photographs cannot capture the three-dimensional (3D) nature of the human torso. To address these issues, a reliable and reproducible method is needed to objectively and quantitatively analyze breast morphometry (preoperatively and postoperatively) causing minimal discomfort to the patient.

Recently, stereophotogrammetry has emerged as a strong new alternative for breast morphology analysis. This methodology can capture the entire breast surface topology in human torso virtually in a single snapshot and without any direct contact with the patient, thus causing minimal discomfort. A 3D torso image enables a 360-degree panoramic visualization of the actual 3D breast morphology by permitting rotation of the imaged torso about the three coordinate axes. With the 3D torso images, it is now feasible to obtain accurate quantitative 3D breast measurements [7].

Objective and quantitative analysis (morphometry) of the patient's breast is critical for preoperative planning and postoperative assessment of outcomes in breast reconstruction for a variety of reasons, a few of which are [1, 7]:

- Preoperative evaluation of breast morphology is essential to determine the correct type and size of implant and tissue expander.
- Preoperative determination of the amount tissue to be recruited from the donor sites is required in the autologous tissue-based breast reconstruction.
- Preoperative evaluation of the degree of breast ptosis is required for planning the procedure of mastopexy.
- Postoperative assessment of the breast symmetry is needed to evaluate the success of the surgery and to subsequently plan for a corrective procedure if necessary.
- Postoperative tracking of the changes in breast morphology after breast surgery is essential for subsequent detection and quantification of complications.

## 1.2 Current Problems

Many methods for assessing breast aesthetics using 3D images of patients have emerged [7–17]. In this study, two novel algorithms for semi-automated analysis of 3D images are presented with the ultimate goal for facilitating computerized breast morphometric analysis.

1. Current quantitative assessments of breast morphology provide a global evaluation of breast morphology at a given time point such as breast ptosis [8], breast symmetry [9, 10], and breast volume [7, 11–17]. But few works are available to correlate local morphological changes in breast over time, which is valuable to better assess the surgical outcomes. In order to compare changes in breast morphology occurring during the time course of several reconstructive procedures, one needs to longitudinally analyze 3D multiple-visit images (Fig. 1.1) acquired at successive time points from the same patient undergoing the multiple surgeries of her breast reconstructive course. The multiple-visit images acquired at different clinical visits may not be in the same coordinate system due to differences in patient positioning and posture. The coordinate system difference should be removed by registering the multiple-visit images before analyzing breast morphology changes caused by breast cancer treatments and reconstruction.

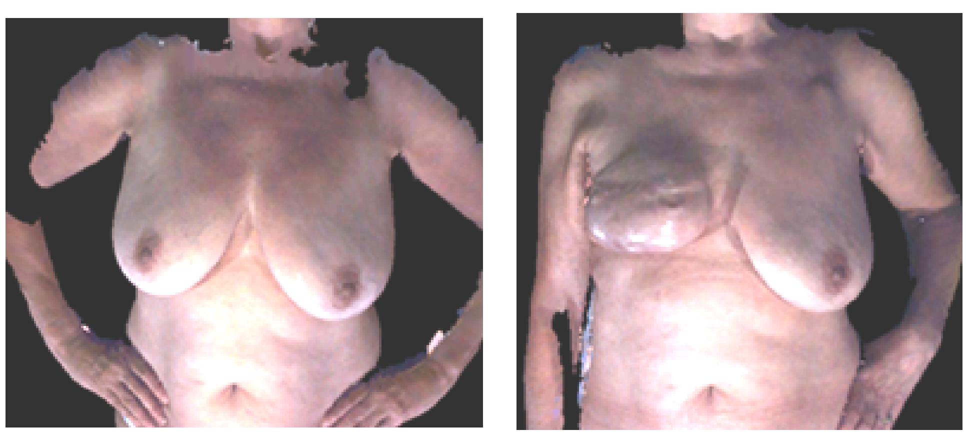

(a) (b)

Figure 1.1: Example of 3D multiple-visit images. (a) Image from initial visit (pre-operative). (b) Image from subsequent visit (post-operative).

2. Breast contour is an important component in breast aesthetic evaluation. It

enables computation of morphological measures such as volume [7, 18–20] and ptosis. Current contour detection methods focus on searching for the breast boundary in 2D planes, which do not directly mirror the 3D breast contours in the 3D images of patients. This work presents a novel algorithm for the detection of the lowest breast contours in 3D images of the female torso.

## 1.3 Objectives

Work completed as a part of this research is described below:

1. **Multiple-visit images registration:** Register 3D surface scans of individual patients from multiple-visits to achieve correspondence between the images. In addition to breast surgery related anatomical changes (see Fig. 1.1), the multiple-visit images from the same patient acquired at different clinical visits may also change as a result of variations in the (a) object coordinate systems due to differences in patient positioning and posture; and (b) patient's BMI due to physiological weight changes. Registration of the multiple-visit images can remove the differences in object coordinate systems between images, thereby facilitating longitudinal quantification of morphological changes in the operated breasts during breast reconstruction.

2. **Lowest breast contour detection:** Detect the lowest contour where breast touches abdomen. This facilitates other measurements such as volume, and identification of relevant features such as IMF.

   The above two algorithms were applied to achieve multiple-view 3D data fusion as described below:

3. **Multiple-view 3D data fusion:** Conventionally, upright view images are used for surgical planning and outcome assessment in breast reconstruction. An inherent limitation of stereophotography is the inability to capture areas that are occluded. For example, the IMF is occluded and cannot be visualized in the upright position when acquiring images of patients with large and ptotic breasts (Fig. 1.2a). Delineation of the anatomical IMF on the upright view image is critical since the IMF is a defining element in the shape and structure of the female breast. Evaluation of the IMF and its position in 3D upright images is an important aesthetic consideration for breast reconstruction.

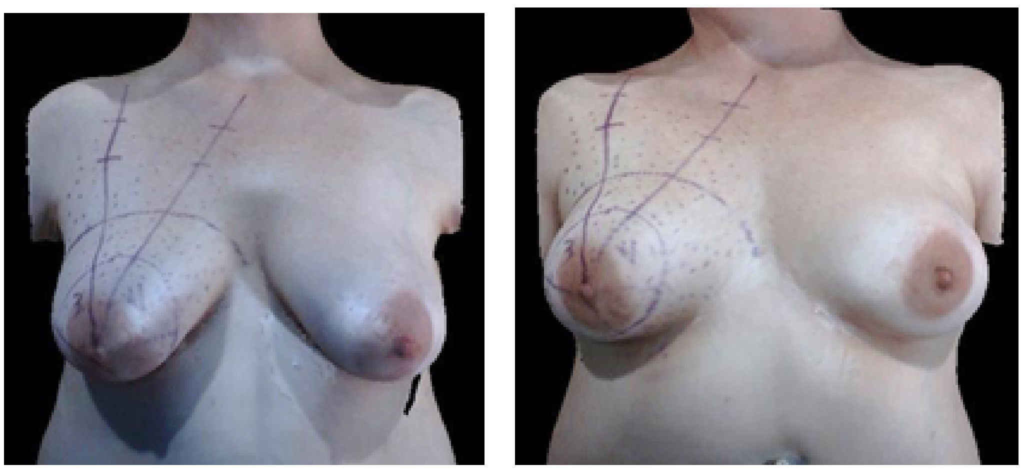

(a) (b)

Figure 1.2: Example of 3D multiple-view images for patient with ptotic breast (grade 2). (a) Upright image (anatomical IMF not visible). (b) Supine image (anatomical IMF visible).

The image registration and lowest breast contour detection algorithms developed in this study were combined to design a data fusion technique with 3D multiple-view (upright and supine) images to visualize the anatomical IMF which is typically occluded from the upright view for women with large and ptotic breasts. The detected lowest breast contours from the supine image (Fig. 1.2b) are transformed and superimposed onto the upright image. The anatomical IMF is visible in the supine position for breasts which are ptotic in the upright position. So the detected lowest breast contours in the supine images correspond to the anatomical IMF and the superimposed contours from the supine image represent IMF position in the upright image.

## 1.4 Layout of the Dissertation

The dissertation is composed of a total of 7 chapters. Chapter 2 briefly introduces the background information on the use of mastectomy for breast cancer patients, followed by breast reconstruction. Then, the literature on the various aesthetic assessment methods for breast reconstruction is reviewed. Chapter 3 describes the 3D image acquisition system for multiple-visit images from the same patient taken at different clinical visits and multiple-view (upright and supine) images used for data fusion. Chapter 4 gives our proposed algorithm that allows registration of 3D multiple-visit images, such that the differences in image-coordinate systems between images are removed. In Chapter 5, we present an approach for the detection of the lowest breast contour in 3D images which employs shape index and minimum principle curvature analysis of the 3D surface. Chapter 6 describes our data fusion technique with 3D upright and supine images to visualize the anatomical IMF which is typically occluded from the upright view for women with ptotic breasts. The summary and future work for this research are given in Chapter 7.

# Chapter 2

# Background

## 2.1 Mastectomy

Mastectomy is a surgery to remove breast tissue from a breast as a way to treat or prevent breast cancer. During the procedure, not only the known tumor but also some of the surrounding breast skin and tissue are removed to ensure that all cancer cells are removed. Currently, there are several surgical approaches to mastectomy such as simple mastectomy (or "total mastectomy"), radical mastectomy (or "halsted mastectomy"), skin-sparing mastectomy, nipple-sparing mastectomy and prophylactic mastectomy. The difference between the mastectomy types is the amount of breast tissue removed during the procedure. The mastectomy type that a patient decides to undergo depends on factors such as the size, location, and behavior of the tumor [21–24]. Fig. 2.1 shows a sample of patient undergoing mastectomy. The right breast tissue of the patient is removed during the mastectomy surgery.

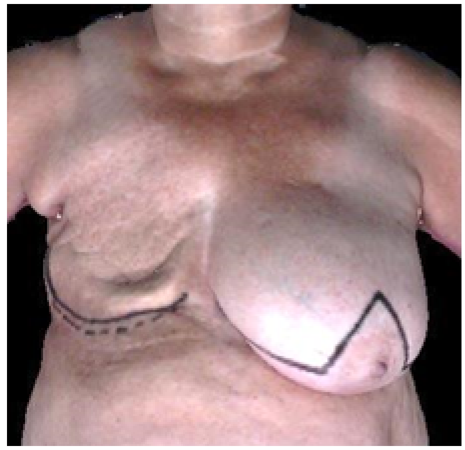

Figure 2.1: 3D sample image of mastectomy. The right breast tissue of the patient is removed

## 2.2 Breast Reconstruction

Breast reconstruction is an integral part of the breast cancer treatment for women who must undergo mastectomy. The surgery physically restores the entire excised breast, or the portion of the breast removed. The goal of breast reconstruction is to restore the patients body to normal or as close to their original physical state as possible. After breast reconstruction, the patients who underwent mastectomy can regain their quality of life by improving their psychosocial well-being such as self-confidence and self-esteem [2, 25].

Breast reconstruction surgery can be performed either at the time of mastectomy or at some point after the initial mastectomy is completed, according to the patient factors and the need for post-mastectomy radiation therapy. For patients with low risk of needing post-mastectomy radiation, immediate reconstruction is preferable to achieve the optimal aesthetic outcome. For patients with high risk of needing post-mastectomy radiation, delayed reconstruction is typically used to optimize both radiation delivery and aesthetic result. If the risk of needing post-mastectomy radiation is increased, "delayed-immediate" reconstruction is a suitable approach, which involves placing a tissue expander at the time of mastectomy and awaiting pathology results to determine the need for radiation and guide reconstruction scheduling [26].

Breast reconstruction surgery is categorized as follows: implant reconstruction, flap (autologous) reconstruction, or a combination of both. Decision of reconstruction type depends on patient's factors such as overall health, the stage of breast cancer, the size of natural breast, and the amount of tissue available (for example, very thin women may not have enough extra body tissue to make flap grafts) [27].

In implant reconstruction, one-stage immediate breast reconstruction may be performed with direct placement of an implant at the time of mastectomy. The implant may be put in the space created during the breast tissue removal with extra support. Two-stage reconstruction or two-stage delayed reconstruction is the most commonly used implant reconstruction. It typically involves the placement of a tissue expander at the time of mastectomy. The tissue expander is gradually filled with fluid over 4 to 6 months to stretch the skin and create a pocket for the implant. Once this process is complete, the expander is removed in a second step and the permanent gel/saline implant is placed. Sometimes, the two-stage reconstruction is called delayed-immediate reconstruction because it allows time for other treatments. If radiation is needed, the next operations may be delayed until after radiation treatment is complete. If radiation is not needed, the surgeon can start immediately with the tissue expander and second surgery [4, 5, 27].

Flap (autologous) reconstruction involves using patient's own tissue from the abdomen, back, thighs, or buttocks to reconstruct the breast. The tissue is called a "flap" and the area it is taken from is called the "donor site". This type of breast reconstruction is very natural and is also the preferred technique for patients who require radiation as part of their therapy. However, the surgery is more involved, and the recovery is usually longer.

The two most common types of flap reconstruction are the TRAM flap (transverse rectus abdominis muscle flap) and the latissimus dorsi flap. The TRAM flap procedure uses tissue from the lower abdominal area. The skin, fat, blood vessels, and at least one abdominal muscle are moved from the abdomen to the chest. The tissue from this area alone is often enough to rebuild the breast, so that an implant may not be needed. The latissimus dorsi flap uses tissue from the upper back. The flap consists of skin, fat, muscle, and blood vessels. It's tunneled under the skin to the front of the chest to create a pocket for an implant [6, 27].

Usually, breast reconstruction cannot be achieved in a single procedure. It is a complex process which can consist of multiple procedures and take up to a year or longer for completion, depending on the type of reconstructive procedures selected and other factors affecting surgical outcome, including postoperative complications and adjuvant cancer treatment. Fig. 2.2 shows a sample of 3D images for a patient undergoing multiple-visit breast reconstruction. In the image of visit 1 (Fig. 2.2a), the left breast tissue of the patient is removed during the mastectomy surgery. In the images of visits 2-4 (Fig. 2.2b-d), the left breast is reconstructed in a multiple procedures. The scar in the abdomen shows that tissue from the lower abdominal area is used to reconstruct the left breast.

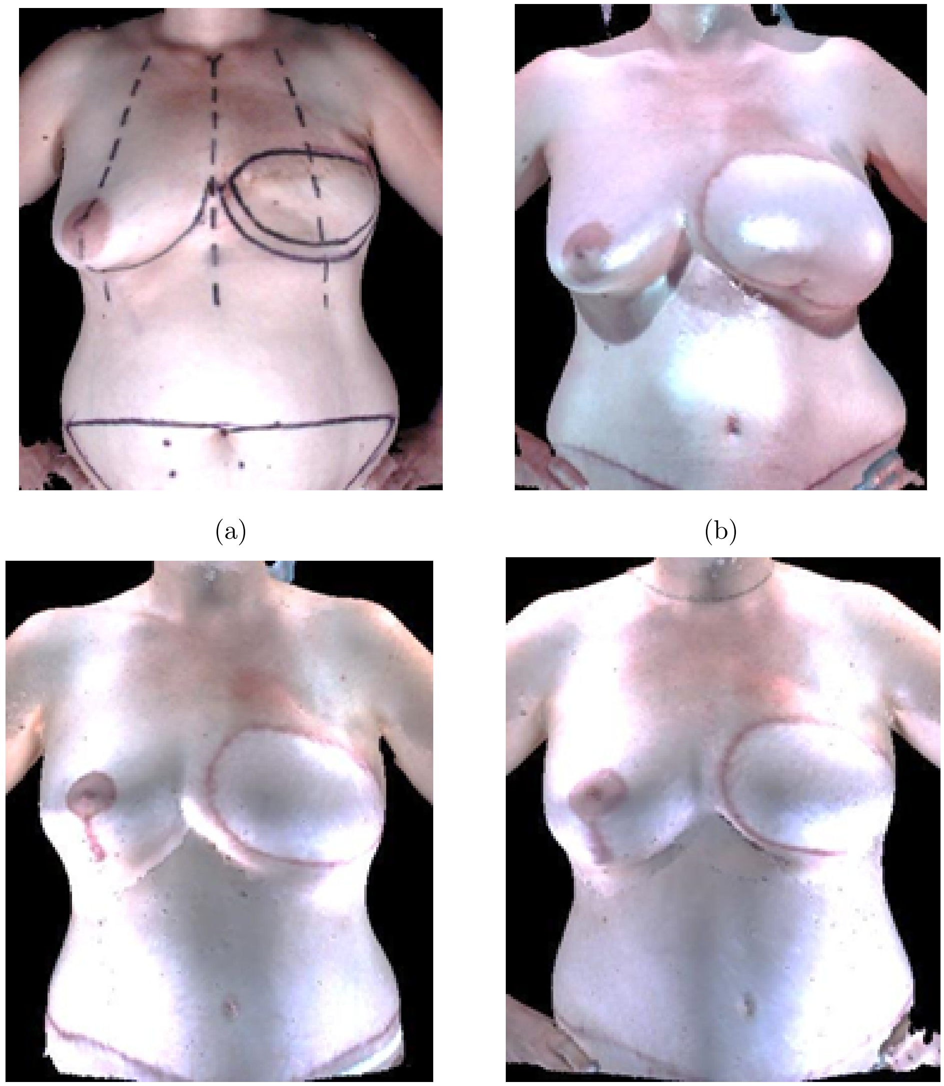

(a) (b)

(c) (d)

Figure 2.2: Representative 3D images for a patient undergoing multiple-visit breast reconstruction. (a) Visit 1, the left breast tissue of the patient is removed. (b) Visit 2. (c) Visit 3. (d) Visit 4. (b)-(d) show that the left breast is reconstructed in a multiple procedures using tissue from the lower abdominal area.

## 2.3 Aesthetic Assessment of Breast Reconstruction

Breast reconstructive surgery starts with a deformed or completely absent breast as following mastectomy, and restores a breast shape that is close to normal in appearance. Patient's satisfaction with breast appearance is without doubt the key factor in determining the success of breast reconstruction. Breast aesthetic assessment can facilitate: (1) preoperative patient education [28]: women who are well informed preoperatively about the surgery may report greater postoperative satisfaction and perceive better quality of life; (2) surgical planning for surgeon [29]: three-dimensional outcome simulation and assessment can be used to predict and plan the operation which aims to achieve a successful reconstructive surgery; (3) documentation of breast metrics for outcomes analysis [7,30]: tracking of the changes in breast morphology after breast reconstruction is essential for subsequent detection and quantification of complications, and for meaningful comparisons between competing surgical techniques.

Breast aesthetics evaluates breast factors such as size, shape, proportion, ptosis, symmetry, skin quality, and nipple location [31, 32]. Current assessment approaches of breast aesthetics can be divided into six categories: subjective assessments by human observers [33–36]; measurements on the patient's body (anthropometry) [7, 37–41]; measurements on 2D photographs (photogrammetry) [8, 42]; measurements using $2\frac{1}{2}D$ images (depth-map) [43–49]; measurements using 3D images of the breasts (stereophotogrammetry) [10, 12–17, 29, 33, 50, 51]; and measurements using other multi-dimensional imaging approaches [52–55].

### 2.3.1 Subjective Assessment of Breast Aesthetics

Traditionally breast assessments are conducted by subjective methods, which include visual assessment and typically employ a crude gradation scale. Subjective assessments are inherently qualitative and lack accuracy and reproducibility. However, subjective assessments of breast aesthetics are still widely used in the clinical applications, due to its simplicity and the low cost [33].

Global scales of four gradations (i.e., rating the overall cosmetic results into four scale scores such as excellent, good, fair, and poor) of aesthetic changes are commonly used in subjective assessment of the breast [35]. It has been argued that global scales suffer from vague terminology. Subscales with more explicit criteria for each aesthetic component (e.g., size, shape) have been recommended [34]. However, the concordance between observers was still reported to be low when such subscales were used [35]. In [35], subscales of four gradations have been employed to rate the difference between treated and untreated breasts in terms of size, shape, skin color and firmness, as well as the visibility of surgical scar. Changes in each aesthetic component are graded as none, mild, moderate, and severe. It shows that low to moderate concordance between observers ($k = 0.24 \sim 0.40$), where $k$ is the Cohen's Kappa statistical measure. $k = 1$ means "perfect agreement" and $k = 0$ means "chance agreement only". The authors also show that the different observer groups also lack concordance. The levels of correspondence were found very low between patients' and professional observers' ratings ($k < 0.10$).

Cohen et al. [36] applied a global five-point scale (i.e. rating the overall cosmetic results into five scale scores: excellent, good, satisfactory, poor, and unacceptable) on assessment of the breast aesthetic appearance using 2D photographs of autologous breast reconstruction patients. In their study, higher reliability was reported among patients ($\alpha = 0.92$) than professional observers ($\alpha = 0.74 \sim 0.89$), where $\alpha$ is the Cronbach's alpha statistic which ranges in value from 0 to 1. The higher the score, the more reliable the assessment is. Inter-rater agreement was poor among both patients and professional observers ($k = 0.0 \sim 0.39$). And weak correlation was found between professional observers and patients ($\rho = 0.36 \sim 0.53$), where $\rho$ is the Spearman's Rho in statistic, wherein a value of 1 means a perfect positive correlation.

To overcome the low intra- and inter- observer agreement, data averaged from a panel rather than individual observers are often employed. In this method, four to six 2D photographs are usually taken of the patient from different angles and then shown to an expert panel. The panel usually consists of healthcare professionals familiar with breast reconstruction. This approach is time and labor consuming, and although calculating an average between observers may reduce variability, it is not necessarily improve accuracy. In Henseler's study [33], the panel of six experts accessed the symmetry of breasts underwent latissimus dorsi flap reconstruction using the four-point grading scale (i.e., giving a mark of 1-4 for a poor to excellent result). They obtained the inter-observer reliability of $k = 0.646$. The agreement between observers is improved but still not optimal.

The subjective assessment of breast reconstruction highlights two major disadvantages. The first one is low intra- and inter-observer agreement which indicates the lack of accuracy and reproducibility. The second one is the lack of a standardized, explicit scale. A crude scale with four or five categories is imprecise for identifying individual aesthetic components. Quantitative, objective measures with high reliability are needed in order to meaningfully analyze the aesthetic outcomes of breast reconstruction [34].

### 2.3.2 Anthropometry

Direct anthropometry refers to measurements performed on the patient's body using a measuring tape. It is based on linear measurements between surface landmarks such as the sternal notch, nipple, inframammary fold, and the lowest visible point of the breast mound. Anthropometry usually measures breasts scaled "normal" or "aesthetically perfect" to provide a useful tool to appraise breast aesthetics, facilitate planning preoperatively, and assess the outcome of surgical procedures to the breast. Aesthetically perfect breast is defined as a non-ptotic breast in which no common aesthetic procedure would be considered appropriate (excluding augmentation) to enhance the breast's form [37].

In Penn's classic article [38], "aesthetically perfect" breasts of 20 women were studied, which has been adopted by many as normative. The parameters studied by Penn are "ideal nipple plane", midclavicle to "ideal nipple plane", midclavicle to nipple, nipple to nipple, nipple to submammary, and manubrium to nipple distances. Many techniques for breast surgery base their preoperative measurement plans and nipple positioning on the distances published by Penn [39].

In another study [40], anthropometry was performed to measure breast values in Turkish female students in order to help in comparing the anthropometric breast values of young Turkish women with those of women in other countries, and also to help either in planning aesthetic and reconstructive breast surgery or in designing breast augmentation accessories. The study included 385 female undergraduate student volunteers between the ages of 18 and 26 years with no physical or developmental deformity. A total of 19 parameters such as sternal notch to nipple, nipple to nipple distances, and breast volume were measured in a standing position. The ideal external view of the breasts with equal volume for both sides and no ptosis was observed in 35.1% of the volunteers.

Liu et al. [41] determined ideal anthropomorphic values of the female breast by measuring the normal breasts of 109 female volunteers to try to obtain useful values in achieving quantitative breast surgery. The ideal sternal notch to nipple, nipple to base, base to inframammary fold distances and other ideal anthropomorphic measurements were calculated and compared with previously published values. For each volunteer, five standardized upright 2D photographs were taken and arranged into a computerized survey, and plastic surgeons, cosmetic breast surgery patients, and reconstructive breast surgery patients were interviewed for aesthetic feedback. Their results show that ideal anthropomorphic values were similar among plastic surgeons and patients.

Anthropometry can be a useful tool for quantifying and interpreting the desired outcomes by establishing standard values of breast. However, this method has several limitations. First, studies to determine ideal anthropometric values of the female breast have relied on subjective aesthetic judgments of one surgeon alone or have conveyed no aesthetic judgment and instead used average linear measurements of the breast [41]. Second, Anthropometry is complicated and time consuming. To establish the standard values of "aesthetically perfect" breast, a considerable number of patients are required and a large number of measurements are needed on each patient. Third, anthropometry is invasive to patients since it is directly performed on patient's body, which can cause discomfort to the patients [7].

### 2.3.3 Photogrammetry (2D)

Photogrammetry makes measurements from photographs of the breasts. Photographs are captured using a single digital camera and contain 2D information of the breasts for the patients.

Limbergen et al. [42] calculated four measurements on anterior-posterior photographs of 142 patients who were treated with tumor excision and external radiotherapy. The four measurements for each breast were: the vertical distance from the level of the sternal notch to the nipple, the vertical distance from the level of sternal notch to the inferior pole of the breast, the horizontal distance from the midline to the nipple, and the horizontal distance from the midline to the lateral breast contour. The differences in each measurement between the left and right breasts were used to determine the symmetry of the two breasts.

Kim et al. [8] investigated quantitative, objective measurements of breast ptosis for patients who underwent breast reconstruction. Their study based on ratios of distances between fiducial points manually identified in oblique and lateral clinical photographs. Breast ptosis refers to the extent to which the nipple is lower than the inframammary fold. Vertical displacements from lateral terminus and the nipple to the sternal notch (or the lowest visible point) of the breast were calculated and used to estimate breast ptosis. They compared their results to ratings made using an existing subjective four-point scale. The intra- and inter-observer variability in the objective measurements related to marking fiducial points was shown to be equivalent to less than one point on the subjective ptosis scale.

Photogrammetry has advantages over anthropometry since a photograph is more efficient and less invasive to the patient. It is possible to make a variety of measurements manually or automatically on digital/digitized photographs. The disadvantages are that some fiducial points may not be visible and the measurements that involve these points cannot be obtained. The fiducial points which have same position in 2D photographs may vary in real 3D space, thus the aesthetic assessment of breasts based on fiducial points measurements in 2D photographs may introduce some error.

### 2.3.4 Depth-map ($2\frac{1}{2}D$)

Cardoso's group [43–49] performed breast measurements using $2\frac{1}{2}D$ images (depth-map) acquired from Kinect. Kinect is a motion sensing device developed by Microsoft and includes one RGB camera and one depth sensor. In depth-map images, the pixels are in color or gray scales which represent depth information. They automatically calculated nipple height (i.e., distance between nipple and chest) and ratio of left and right nipple heights. The measurements showed less error than real ratios manually obtained by physician. This group also presented a method simultaneously detecting breast peak point and contour in depth-map images [47,48]. Peak point is the area in breast closest to camera and was determined based on the gradient vector field and convergence filter. Breast contour was found as the solution to the shortest-path problem in the graph theory framework, after modeling the image as a weighted graph using gradient.

Beside the 2D information, depth-map also contain depth information for each pixel, thus some 3D measurements can be performed in depth-map images. However, depth-map still cannot capture the overlapped regions in the patient, e.g., the area beneath the breast with high ptosis degree. In fact, Cardoso's group detected a breast boundary same as in (2D) photographs, rather than the 3D breast contour in the surface image.

### 2.3.5 Stereophotogrammetry

Stereophotogrammetric assessment of breast aesthetics relies on the simultaneous capture of the breast surface by two or more pairs of cameras, followed by build-up of a natural life-like 3D image that has advantages in the analysis of breast 3D structures [33]. 3D images permit accurate and objective assessment of breast aesthetics such as volume, surface area, shape, and symmetry. A single 3D image yields more information regarding breast structures than multiple conventional 2D photographs, thus allowing better assessment of some measures such as volume and surface area which cannot be accurately assessed using 2D photographs [50].

Kawale et al. [10] evaluated symmetry of breasts in 3D images using the Percentage Breast Retraction Assessment (3D $pBRA$) index in two different poses: (1) hands-on-hip and (2) hands-down. Three fiducial points, sternal notch and left and right nipples were annotated by naive observers in both 3D image and 2D photographs. Two reference points were automatically calculated based on the coordinates of the three fiducial points. Geodesic distances along surface (or Euclidean distances) between the fiducial point and reference points were used to calculate 3D (or 2D) $pBRA$ index. They validated that the 3D $pBRA$ index is linearly correlated with the 2D $pBRA$ for both of the poses, and is independent of the localization of fiducial points within a tolerance limit of 7 mm. The quantitative assessment of 3D symmetry was found to be invariant of subject pose, while problems with pose were inherent in 2D photographs. Their study further corroborates the advantages of 3D stereophotogrammetry over 2D photography.

Breast volume is an extremely useful component for the correction of breast asymmetry in breast reconstruction. For example, the calculated volumes of the two breast for a patient could facilitate the selection of the amount of implant/tissue that would provide improved symmetry. Many methods have been proposed to determine breast volume: water displacement, the Grossman-Rounder device, biostereometric analysis, thermoplastic casting, and radiographic techniques [12–16]. Most of them are inaccurate, time consuming, or expensive. Stereophotogrammetry overcomes these limitations, permitting semi-automated and automated calculation of breast volume. Passalis et al. [17] developed an automated measurement of breast volume from 3D image. Four landmarks near the boundary of the breast were automatically identified and connected to create the optimum path along the surface. The breast lies inside these four optimum paths. The optimum path is the geodesic path along the surface between two landmarks and created by determining the shortest path in weighted 3D mesh using Dijkstra's algorithm. An interpolating "Coons Patch" surface was built using the four optimum paths. This surface represents the chest wall that is beneath the breast. The breast volume was then computed as the volume from the Coons patch to the skin surface of the breast by integration.

Galdino et al. [29] analyzed 3D images of over 50 patients who underwent breast reconstruction. They estimated the expander and implant volumes to preoperatively decide the type of breast reconstruction surgery, and assessed breast asymmetry to postoperatively plan subsequent revisions. Their application demonstrated that 3D imaging is very helpful in providing objective information about the breast for use in preoperative planning and postoperative outcome assessments.

Stereophotogrammetry has tremendous potential for analysis of breast aesthetics. The fiducial point identification is made easier by being able to panoramically rotate the 3D surface enabling views from any desired angle. Breast volume can be estimated accurately and non-invasively. However, the technique does have limitations, particularly, 3D images acquired form patients with large and ptotic breasts may have occluded area, and the inability to visualize and capture these areas can adversely affect measurements. Nevertheless, 3D systems may offer the most accurate of currently available approaches to quantify numerous components of breast aesthetics [51].

### 2.3.6 Other Multi-Dimensional Imaging Approaches

4D imaging [52–55] is used to refer to the mechanism of 3D imaging plus automation. This automation was accomplished by the following methodology: A point cloud arising out of the structured light-based image capture system was converted to a 3D mesh reconstruction of the form of the patient. Onto this mesh, the individual texture images were registered to generate a life-like and recognizable rendering. Besides point cloud, 3D mesh, and texture which are same as the widely-used 3D images, a separate color contour map was generated from the relationships between adjacent minima and maxima of the 3D mesh contour. Key fiducial points were recognized by virtue of being minima and maxima within this color contour map using the proprietary software developed specifically for breast imaging.

Based on the key fiducial points, the point-to-point (Euclidean) distance measurements and surface (geodesic) distance measurements were calculated. Point-to-point distance measurements are: midline of torso; breast base width; nipple to midsternal line; nipple-to-nipple distance; intermammary distance; inferior breast radius; midclavicle to nipple distance; and breast height. Surface (contour) distance measurements are: sternal notch to nipple distance; nipple to inframammary fold distance; and midclavicle to nipple distance. Breast asymmetry was measured based on sternal notch to nipple distance and nipple to inframammary fold distance [52,54].

The volume of the soft tissues of the breast can also be measured based on the previously described key fiducial points. The boundaries of what constituted the breast were automatically determined based on the key fiducial points IMF, midpoint, armpit, mid clavicle, and nipple. A construction of the underlying chest wall was rendered on the basis of peripheral boundaries, with a spline interpolation method. The breast volume was calculated as the 3D integral between the 3D breast surface and the underlying chest wall [52].

To demonstrate their software, the authors compared manual and 4D automated measurements. The overall correlation of manual to automated measurements was 91%. The repeatability of the automated measurements ($R = 0.996$) compared favorably to inter-observer variability with manual measurements ($R = 0.993$). $R$ is the Pearson correlation coefficient, where 1 is total positive correlation, 0 is no correlation, and $-1$ is total negative correlation [52].

The 4D imaging system also provided algorithm to simulate the postoperative breast appearance. They constructed the chest wall based on the fiducial points IMF, midpoint, armpit, mid clavicle, and nipple. After calculating the volume of the breast form's soft tissue, the volume of the breast implant was added and, to a varying degree, a percentage of volume was subtracted, depending on the existing volume of breast and the size of implant chosen. The original breast form was removed from the image and the breast mound with modified volume was added on to the chest wall [53, 55].

The 4D images include 3D point cloud, mesh, and texture information, similar to the 3D images. This method has same limitations as 3D imaging. For example, the measurements will be influenced due to occluded area in images from patients with large and ptotic breasts. Nevertheless, 4D imaging is more convenient to use due to its proprietary software which can automatically identify key fiducial points, measure Euclidean distances and geodesic distances between two key fiducial points, measure breast asymmetry, and estimate breast volume.

## 2.4 Summary

The goal of breast reconstruction is to improve the breast morbidity due to deformity caused by mastectomy and to maximize the life quality of the breast cancer survivors. Developing objective, quantitative methods to assess breast aesthetics is important to understand the impact of deformity on patients' life quality, guide selection of breast reconstruction type, and evaluate reconstructed breast form.

Current subjective assessments of breast aesthetics are plagued with poor reproducibility and are influenced by observer rating interpretations. Anthropometry, which yields more objective data based on physical measurements, is time consuming and invasive to patients. 2D photogrammetry is time and labor intensive. And many measurements cannot be conducted on 2D photogrammetry due to its lack of 3D information.

Stereophotogrammetry and 3D imaging offers clinical potential for assessment of breast aesthetics due to reproducibility and accuracy. Some important elements such as anatomical IMF cannot be visible in the 3D upright views acquired from patients with large and ptotic breasts. In this case, measurements related to anatomical IMF will not be conducted in the upright images which are conventionally used in breast aesthetic assessments. Thus, new methods on breast aesthetic measurements should be developed to overcome these problems and to make sereophotogrammetry have better performance.

# Chapter 3

# Image Acquisition

The 3D images used in this research are captured using a custom-designed imaging system. This imaging system is composed of two parts. The first part is a commercially available system, namely, 3dMDtorso$^{\mathrm{TM}}$ Imaging System [18] manufactured by 3dMD Inc., Atlanta, Georgia. The second part is a Tri W-G TG2732 bariatric motorized tilt table manufactured by Tri W-G, Valley City, North Dakota. The tilt table is mounted to enable acquisition of 3D images of the patient's breasts in a range of positions from standing upright to supine, and any reclining angles in between.

## 3.1 3dMDtorso$^{\mathrm{TM}}$ Imaging System

The 3dMDtorso$^{\mathrm{TM}}$ imaging system incorporates four Modular Camera Units. Each Modular Camera Unit incorporates a pair of stereo cameras to serve as the foundation for generating the 3D surface shape information. The pair of stereo cameras is synchronized using a random white light projector. A color camera located in the center of each Modular Camera Unit, which is fired by the external white light flash unit, is used to capture the 2D texture photograph.

When acquiring a 3D image, the four Modular Camera Units are positioned around the patient's frontal torso region at four viewpoints to achieve optimal patient's torso surface coverage. All four of the Modular Camera Units are synchronized at a 1.5 millisecond capture speed in that the four random white light projectors simultaneously trigger all of the four pairs of stereo cameras to start together. A half millisecond later the four color cameras are triggered simultaneously to capture the photographs from the four viewpoints.

The 3dMDtorso$^{TM}$ imaging system utilizes a sophisticated software-driven technique to create a unique 3D surface feature by integrating a series of individual features from the four pair of stereo cameras simultaneously. Once the 3D surface shape information has been generated, the software algorithm maps on the color texture information. The system automatically generates a single highly precise 3D surface image which has the following structure: (a) Point cloud: the set of vertices on the 3D surface. All points have x, y, and z coordinates in a single coordinate system (Fig 3.1a); (b) Polygon surface mesh: the points are connected to create a polygon (usually triangular) surface mesh (Fig 3.1b); (c) Texture information: the 2D texture photographs are mapped onto the 3D surface mesh (Fig 3.1c).

## 3.2 Tilt Table

The width, length, and height of the bariatric motorized tilt table are 31 inches, 81.5 inches, and 34.5 inches respectively when the table is at 0 degree (with the patient in the supine position). A footplate is attached to the table for standing when the table is tilted to the 90 degree (with the patient in the standing upright position)

(Fig. 3.2a).

In order to acquire images of the patient's torso at various inclines without needing to recalibrate the tilt table after each change in table position, a 3 inch tubular steel frame was designed, fabricated, and installed on the table (Fig. 3.2b). The Modular Camera Unit is positioned and adjusted at each corner of the frame so that the patient's breasts could be optimally viewed and imaged from viewpoints of the stereo cameras.

The customized imaging system can change the patient's position before image capture from supine (0 degrees) to standing upright (90 degrees) and any position in between. Changes in tilt table position are controlled by a handheld switch that activates an electric motor to tilt the table through a range of angles, and indicated with the tilt angle indicator (Fig. 3.2c).

The multiple-visit images are captured from the individual patient with upright position at different clinical visits. The multiple-view images are acquired from the individual patient with upright and supine positions at the same clinical visit by the aid of the tilt table.

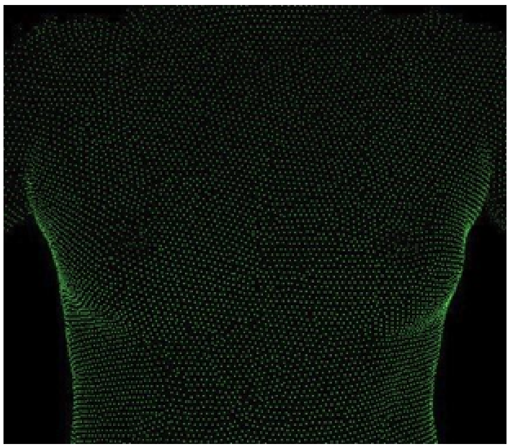

(a)

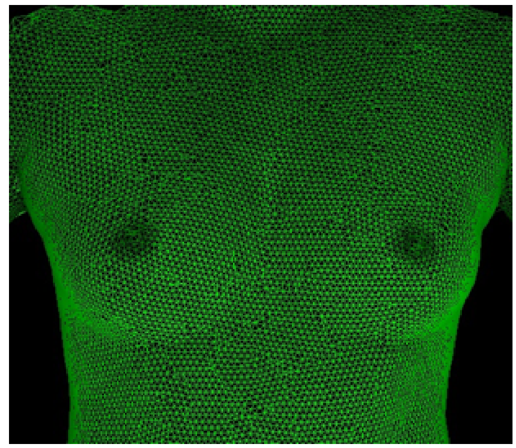

(b)

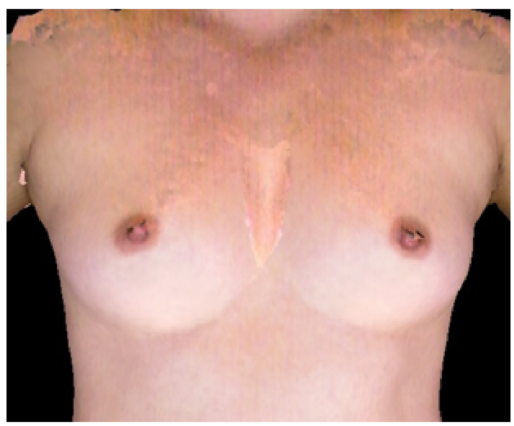

(c)

Figure 3.1: Example of a 3D surface image. (a) Underlying 3D point cloud. (b) Underlying 3D triangular mesh surface geometry. (c) 2D texture photograph overlaid onto the 3D triangular mesh surface geometry.

(a)

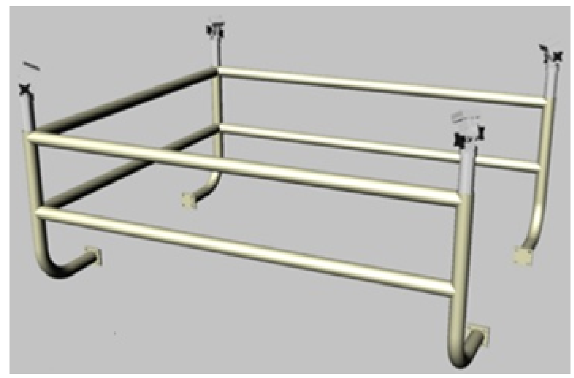

(b)

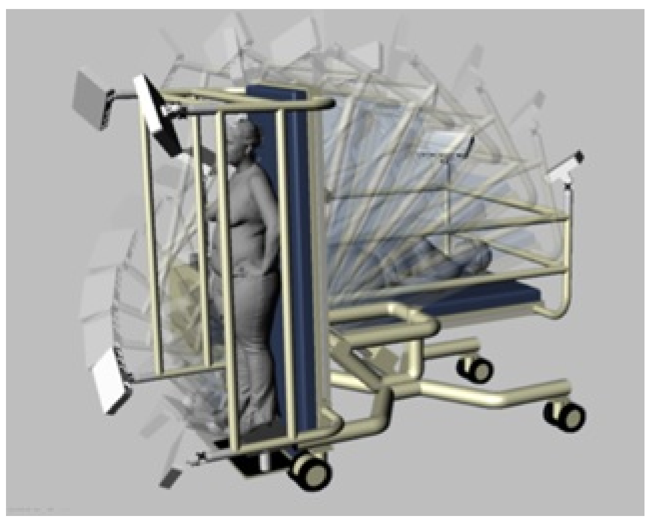

(c)

Figure 3.2: Custom designed 3D imaging system from 3dMD Inc. (Atlanta, Georgia). (a) Tri W-G TG2732 bariatric motorized tilt table. (b) Tubular steel frame, the Modular Camera Unit is positioned at each corner of the frame. (c) Customized imaging system can position the patient from supine (0 degrees) to standing (90 degrees), and any angles in between.

# Chapter 4

# 3D Registration of Multiple-visit Images

## 4.1 Introduction

In addition to breast-cancer treatment or surgery related anatomical changes (see Fig. 4.1a and Fig. 4.1b), the multiple-visit images for a patient acquired from different clinical visits may also change as a result of variations in the (1) object coordinate systems due to differences in patient positioning and posture; and (2) patient's BMI due to physiological weight changes. As a first step, registration of the multiple visits images is thus required in order to remove spatial variations between images and to monitor and quantify the morphological changes occurring in the breasts.

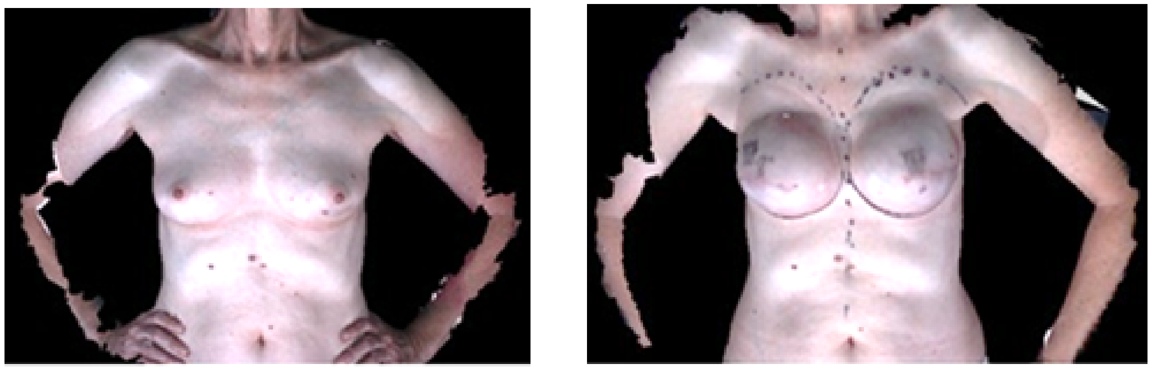

(a) (b)

Figure 4.1: 3D multiple-visit images. (a) Image from the initial clinical visit (pre-operative). (b) Image from a subsequent clinical visit (post-operative).

### 4.1.1 Introduction to Registration

Image registration is a process that seeks to achieve the best correspondence to map or transform one image (target) to the other image (reference) [56]. Image registration methods are broadly classified into two main categories: rigid registration and non-rigid registration.

Rigid registration encompasses linear transformation, wherein the coordinates of points in the target image are linearly transformed to achieve correspondence with those in the reference image. Rigid registration is categorized into rigid (body) registration and affine registration. Rigid (body) transformation includes only translations and rotations, while affine transformation involves the combination of translations, rotations and scaling.

Non-rigid registration constitutes a deformable transformation. The deformation is shaped either through biological differences or image acquisition or both. Correspondence between structures in two images cannot be achieved without some localized stretching of the images. The non-rigid transformation can include either linear elastic transformation, viscous fluid transformation or other complicated forms.

Our objective is to use the torso correspondence achieved between the multiple-visit images to view and analyze images in the same coordinate system. Our overarching goal is to use multi-visit registration to facilitate quantification of morphological changes in breast appearance over time in an individual. Non-rigid registration may introduce warping changes, which would introduce artificial changes in surface geometry and lead to artifacts in quantification of the local breast morphology. The 3D image reflects the real size of the patient's torso, so an affine registration is not necessary. Thus, we use a rigid registration procedure, which only includes translations and rotations to implement 3D torso surface scan correspondence in order to remove coordinate system differences between the multiple-visit images.

### 4.1.2 Related Work

Rigid registration of 3D surface images has been extensively studied in computer graphics and depending on the driving application, many different automated, semi-automated, and interactive approaches exist for registering two surfaces with each other [57, 58].

The Iterative Closest Point (ICP) algorithm is most commonly used for registration [59–61], and for the integration of multiple range images for generating a 3D surface model [62, 63]. ICP methods determine a set of rigid transformation parameters by minimizing the cost function between the corresponding points in the target image to a given set of control points from the reference image obtained using random or uniform sampling.

Besl et al. [59] proposed a method that found the corresponding points in the target image by first creating a simplex-based approximation, and then computing the exact corresponding points using the approximate corresponding points estimated from solving point-to-triangular set distance problem. Blais et al. [60] determined the corresponding points based on reversing the rangefinder calibration process. Dorai et al. [62] calculated the corresponding points by finding the intersection of the target image and the surface normals for the control points in reference image. In [59], [60], and [62], the transformation parameters were optimized by iteratively minimizing the cost functions-mean squared Euclidean distance, the sum of Euclidean distances, and the sum of squared Euclidean distances between control points and corresponding points respectively. Masuda et al. [61] defined the corresponding points in target image as the points with the shortest Euclidean distances to the control points from the reference image, which were found using a brute-force search. In other work of Masuda's group [63], the corresponding points were determined by searching the closest triangle in the reference image using kDtree. Both [61] and [63] achieved the optimization of the transformation parameters by finding the least median of squared Euclidean distances between control points and corresponding points.

The ICP method is useful and efficient for registration, but one of its major drawbacks is that it may report convergence to an incorrect local minimum. To address the local convergence problem of ICP, close initialization using feature extraction and matching techniques is usually required before refinement using ICP-based algorithms.

Many methods have been designed for feature extraction which can be used as close initialization for ICP algorithms. Sun et al. [64] generated a feature carrier, a 2D point fingerprint by projecting geodesic circles on the tangent plane. The point fingerprint was able to carry curvature, color, and other information. Corresponding points on images from different views were then found by comparing their fingerprints. Zou et al. [65] developed a salient point-based shape description wherein the saliency-driven key points were extracted as local extrema of the difference of Gaussian function defined over a curved surface in geodesic scale space and used to achieve correspondence. Similarly, Wen [66] suggested a medical image registration method using points, contours and curves. The features were extracted from the images semi-automatically. In [67], salient points, which were identified as corners, were used to estimate the transformation parameters.

All the above methods extracted features from image areas where salient changes are observed. Our multiple-visit image registration focuses on matching the 3D torsos along the chest wall, which is relatively smooth and anatomically does not exhibit salient features that can be extracted. Although anatomically the breast mounds exhibit characteristic morphology, such as nipples that can be used as features for surface mapping, in our study the multiple-visit images differ in the region of the breast mounds due to surgical deformations, thereby eliminating the possibility of using algorithms that rely on features extracted from images.

Boughorbel et al. [68–71] developed a rigid registration method based on Gaussian fields which was used to measure both the spatial proximity and visual similarity of points belonging to two multiple-view range images. This method can extend the size of the convergence region such that a close initialization is not needed, thus overcoming local convergence problems of ICP algorithms. Extending the width of the convergence region was done by increasing a parameter $\sigma$, which controls the decay with distance between points. However, this relaxation comes at the price of decreasing the localization accuracy of the criterion. And also, this method is not robust when considering high level of noise. Li et al. [72] proposed a rigid registration method, which can provide global matching. They introduced a Gauss map of the surface and measured the distribution of surface curvature by projecting spherical surface texture to a bifacial plane. The shortcoming of this method is that it is not robust and can only solve the rotation parameters.

Most of the existing rigid registration algorithms have drawbacks that preclude their application to our multiple-visit images from breast reconstruction surgery. Thus we previously reported a registration method for multiple-visit images [73], in which two fiducial points, the sternal notch (SN) and umbilicus (UM) were manually identified as two control points and other thirteen control points were automatically selected based on the location of SN and UM. Registration was achieved by maximizing the correspondence between the fifteen pair of control points from the two images. This method solved the local convergence problem of ICP algorithms. However, any operator bias caused by manual fiducial point selection, and anatomical location change of the UM between multiple-visit images caused by breast reconstruction surgery would likely introduce registration error. To address this problem, we improved our previous registration method in [73] by optimizing the best locations of SN and UM, and thereby the selection of the remaining thirteen control points in the target image. The new rigid registration algorithm for 3D multiple-visit images is described in section 4.2.

## 4.2 Algorithm

### 4.2.1 Assumption

Our approach builds on the assumption that while the soft tissues of the patient's body may change over time due to BMI variation or breast reconstruction surgery, the skeleton is relatively stable. Thus the skeletal frame can be treated as being rigid, i.e., involving only translational and rotational transformations. Selecting points with reference to the skeletal frame in the torsos of the two images and maximizing the correspondence between these points can then achieve 3D image registration.

### 4.2.2 Overview

The overview of our algorithm is illustrated in Fig. 4.2. In the reference image (image from the initial clinical visit), we select fifteen control points, in which two fiducial points SN and UM are manually identified, and other thirteen control points are automatically calculated from the surface of the 3D image based on the coordinates of SN and UM. The thirteen control points are selected from the area of the patient's torso where bony structures corresponding to the skeletal framework are perceptible, while the presence of soft tissue is minimal.

In the target image (image from a subsequent clinical visit), we also manually identify SN and UM. But instead of directly serving as the corresponding points in the target image, the two fiducial points are used as the initialization for optimizing the selection of the SN and UM location in the target image. The SN and UM locations corresponding to those in the reference image are searched around the initialized SN and UM locations (i.e., manually identified fiducial points locations) in the target image in the pre-specified regions. In this research, we use the region size as $50mmX50mm$. It is large enough to avoid operator bias since the reported intra- and inter- variation for manual fiducial point identification is less than $15mm$ [10].

For each selection of a new pair of candidates locations for the SN and UM, the remaining thirteen control points are automatically calculated from the target image. We iteratively register the fifteen pair of control points from the two images by minimizing the value of a cost function (described in subsection 4.2.7), to obtain the optimized transformation parameters. The final cost value from each iteration is compared with that from all others. The iteration with the minimum final cost value will be the optimized output.

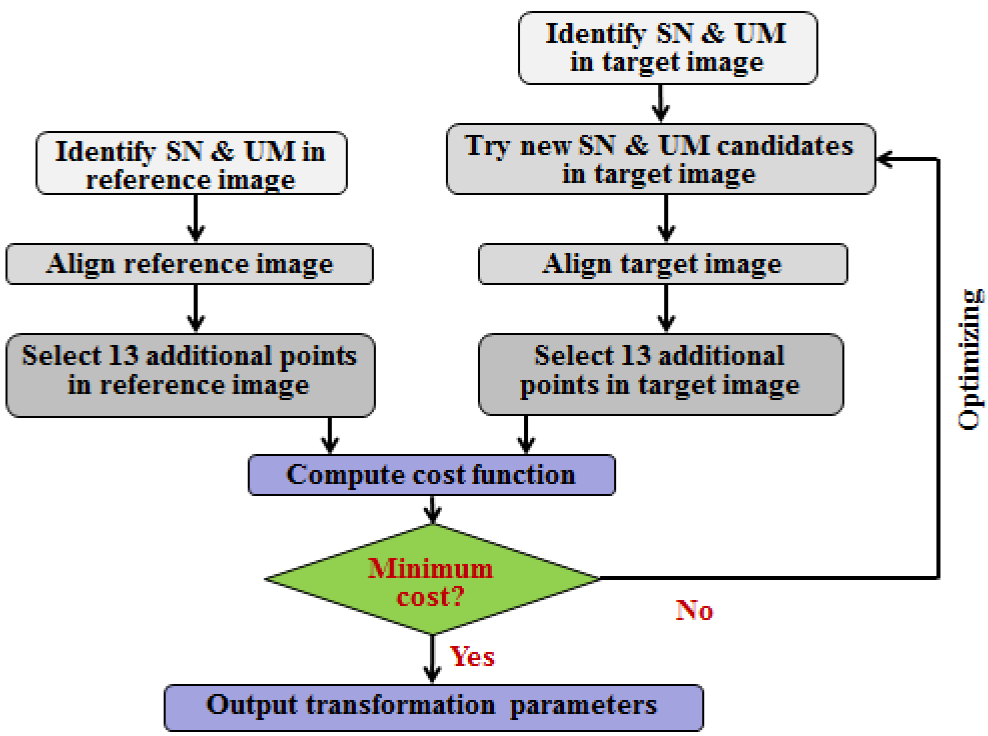


Figure 4.2: Overview of the 3D registration algorithm for multiple-visit images

### 4.2.3 Control Points Selection

Based on the locations of SN and UM in the surface image, the other thirteen control points are automatically selected in the $y$-direction along a vertical (midline) axis and in the $x$-direction along the horizontal axis perpendicular to the midline, from the two fiducial points giving a total of fifteen control points in each image (see Fig. 4.3). Let d represent the straight-line distance between SN and UM after image alignment (image alignment is described in subsection 4.2.4). The other thirteen control points are equally spaced ($0.1d$) along $x$ and $y$ directions (Fig. 4.3). The $x$ and $y$ coordinates of the $i$th control point ($x_i$,$y_i$) are:

$$\big(0,-\tfrac{d}{10}\big),\big(0,-\tfrac{2d}{10}\big),\big(0,-\tfrac{3d}{10}\big),\big(0,-\tfrac{4d}{10}\big),\big(0,-\tfrac{5d}{10}\big),\big(\tfrac{d}{10},-\tfrac{d}{10}\big),\big(-\tfrac{d}{10},-\tfrac{d}{10}\big)$$

$$\big(\tfrac{2d}{10},-\tfrac{d}{10}\big),\big(-\tfrac{2d}{10},-\tfrac{d}{10}\big),\big(\tfrac{d}{10},-\tfrac{2d}{10}\big),\big(-\tfrac{d}{10},-\tfrac{2d}{10}\big),\big(\tfrac{2d}{10},-\tfrac{2d}{10}\big), and\big(-\tfrac{2d}{10},-\tfrac{2d}{10}\big)$$

Interpolation is used to determine the $z_i$ coordinate for each of the thirteen- $i$th control point (subsection 4.2.5). $0.1d$ is used to uniformly select the five points in the area of the sternum, and four points above each breast and in the area near the sternum and the clavicle. These areas have underlying bony structures with minimal soft tissues. Although three points, which are not in a line, are enough to determine the position of torso in 3D coordinate system, we need more points to obtain the optimal transformation parameters due to the variation of patient's posture and BMI. Considering the running time, we choose fifteen control points.

The algorithm is robust to operator bias caused by manual fiducial points identification and location change of UM between multiple-visit images caused by breast reconstruction surgery, due to the optimization process employed during the registration algorithm described in subsection 4.2.6. We used mannequin images to demonstrate the robustness of the optimization (subsection 4.6.1). To improve precision in the automatic selection of the control points, we initially adjust the surface image to be forward facing upright position as described in the next subsection.

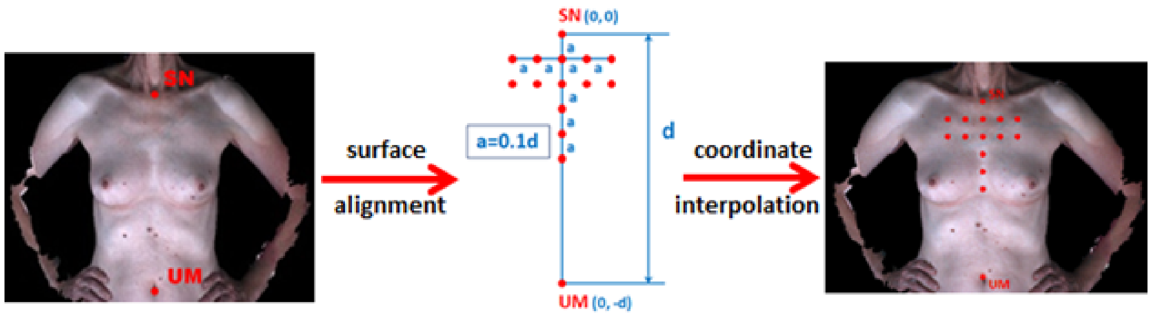


Figure 4.3: Control points selected on the torso for 3D correspondence.

### 4.2.4 Image Alignment

The 3D images acquired from participants typically vary from the forward facing upright position (i.e., alignment along the X and Y-axis) ranging anywhere from $0 - 90°$ due to variations in patient positioning across the multiple clinical visits. These variations tend to introduce large discrepancies in the automatically selected thirteen control points. To mitigate this effect, for both the images to be registered, we initially align the median (midsagittal) axis of the torso along the line joining SN-UM to be coincident with Y-axis of the 3D image coordinate axes, and the 3D torso to be forward facing upright position (Fig. 4.4) as follows.

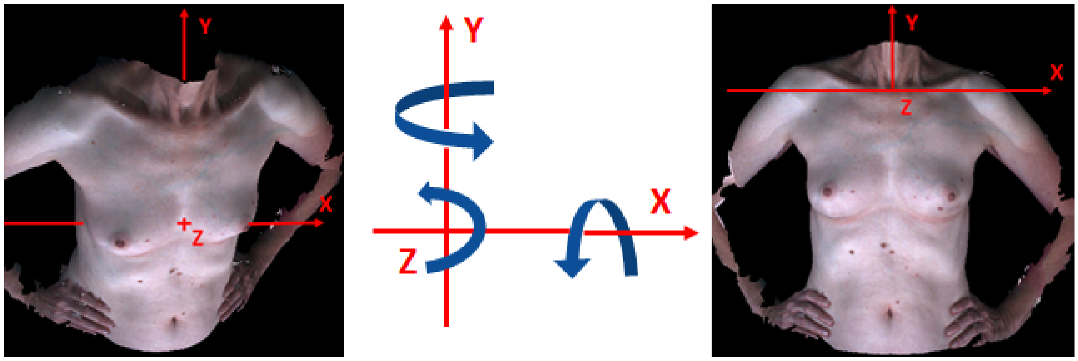

Figure 4.4: Image alignment: align the median (midsagittal) axis of the torso along the line joining SN-UM to be coincident with Y-axis of the 3D image co-ordinate axes, and the 3D torso to be forward facing upright position

First, we transform the image such that SN and UM have the same $x$ coordinate, i.e., the image is translated such that the SN is at the origin and then rotated about the Z-axis. The rotation angle $\gamma$ about the Z-axis and the transformation matrix are given as:

$$\gamma = \sin^{-1}\left(\frac{-x_2}{\sqrt{x_2^2 + y_2^2}}\right) \tag{4.1}$$

$$\begin{bmatrix} 1 & 0 & 0 & 0 \\ 0 & 1 & 0 & 0 \\ 0 & 0 & 1 & 0 \\ -x_1 & -y_1 & -z_1 & 0 \end{bmatrix} \begin{bmatrix} \cos\gamma & \sin\gamma & 0 & 0 \\ -\sin\gamma & \cos\gamma & 0 & 0 \\ 0 & 0 & 1 & 0 \\ 0 & 0 & 0 & 1 \end{bmatrix} \tag{4.2}$$

where $x_1$, $y_1$, $z_1$ represent the $x$, $y$, and $z$ coordinates of SN (before translation); $x_2$ and $y_2$ represent the $x$ and $y$ coordinates of the UM (after translation).

Next, we rotate image about the X-axis such that median axis along SN-UM coincides with the Y-axis. The rotation angle $\alpha$ about the X-axis and the transformation matrix are:

$$\alpha = \sin^{-1}\left(\frac{z_2^{'}}{\sqrt{y_2^{'2} + z_2^{'2}}}\right) \tag{4.3}$$

$$\begin{bmatrix} 1 & 0 & 0 & 0 \\ 0 & \cos\alpha & \sin\alpha & 0 \\ 0 & -\sin\alpha & \cos\alpha & 0 \\ 0 & 0 & 0 & 1 \end{bmatrix} \tag{4.4}$$

where $y_2^{'}$ and $z_2^{'}$ represent the $y$ and $z$ coordinates of UM (following rotation about the Z-axis in the previous step).

Finally, we rotate the image about the Y-axis to achieve surface forward facing. Two symmetric points $S_r(-x_m, y_m, z_r)$ and $S_l(x_m, y_m, z_l)$ (Fig. 4.5) are determined on the surface based on the predefined $x_m$ and $y_m$ values. $z_r$ and $z_l$ are calculated using the interpolation method described below in subsection 4.2.5. Let two vectors $\overrightarrow{a}$ and $\overrightarrow{b}$ be the projections for vectors $\overrightarrow{OS_r}$ and $\overrightarrow{OS_l}$ on the XZ plane, where $O$ is the origin of the image's coordinate system. Then $\overrightarrow{a} = (-x_m, 0, z_r)$ and $\overrightarrow{b} = (x_m, 0, z_l)$. The internal angle bisector between $\overrightarrow{a}$ and $\overrightarrow{b}$ is defined as $\overrightarrow{c} = \frac{\overrightarrow{a}}{\left|\overrightarrow{a}\right|} + \frac{\overrightarrow{b}}{\left|\overrightarrow{b}\right|}$. The angle of rotation about the Y-axis and the transformation matrix are determined as:

$$\beta = \tan^{-1}\left(-\frac{x_c}{z_c}\right) \tag{4.5}$$

$$\begin{bmatrix} \cos\beta & 0 & -\sin\beta & 0 \\ 0 & 1 & 0 & 0 \\ \sin\beta & 0 & \cos\beta & 0 \\ 0 & 0 & 0 & 1 \end{bmatrix} \tag{4.6}$$

where $x_c$ and $z_c$ represent the $x$ and $z$ components of $\overrightarrow{c}$.

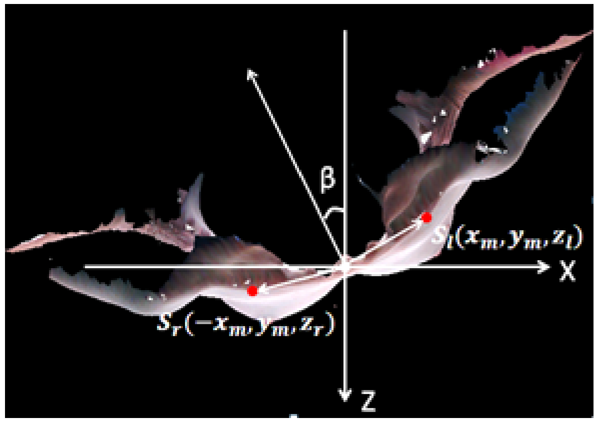


Figure 4.5: Illustration for calculation of rotation angle $\beta$ (top-down view)

### 4.2.5 Coordinate Interpolation

To improve the accuracy of registration, we use interpolation in triangular mesh of 3D image to compute the coordinates of the other thirteen control points based on the location of SN and UM, for both the images to be registered.

To determine the $z_i$ coordinate for $i$th of the thirteen control point. The surface triangles of the 3D mesh (Fig. 4.6a) are first projected onto the XY plane, i.e., only $x$ and $y$ coordinates for the vertices of the triangles are considered. For all projected triangles, we next determine the triangle that encloses the point $(x_i, y_i)$ as follows. In a 2D plane, if a point D is in a triangle $\Delta$ABC (see Fig. 4.6b). then the area of $\Delta$ABC equals the sum of areas of $\Delta$ABD, $\Delta$BCD, and $\Delta$ADC. Otherwise, point D is not in $\Delta$ABC. For a point D that is enclosed in $\Delta$ABC, we determine $z_i$ using linear interpolation based on the corresponding 3D coordinates of 3 vertices of the triangle and $x_i$ and $y_i$ values for point D:

$$z_i = z_{p1} + (z_{p2} - z_{p1})\frac{x_i - x_{p1}}{x_{p2} - x_{p1}} \tag{4.7}$$

where

$$x_{p1} = x_A + (x_B - x_A)\frac{y_i - y_A}{y_B - y_A}$$

$$z_{p1} = z_A + (z_B - z_A)\frac{y_i - y_A}{y_B - y_A}$$

$$x_{p2} = x_A + (x_C - x_A)\frac{y_i - y_A}{y_C - y_A}$$

$$z_{p2} = z_A + (z_C - z_A)\frac{y_i - y_A}{y_C - y_A}$$

where $x_A, y_A, z_A, x_B, y_B, z_B, x_C, y_C, z_C$ are coordinates of vertices A, B, and C respectively.

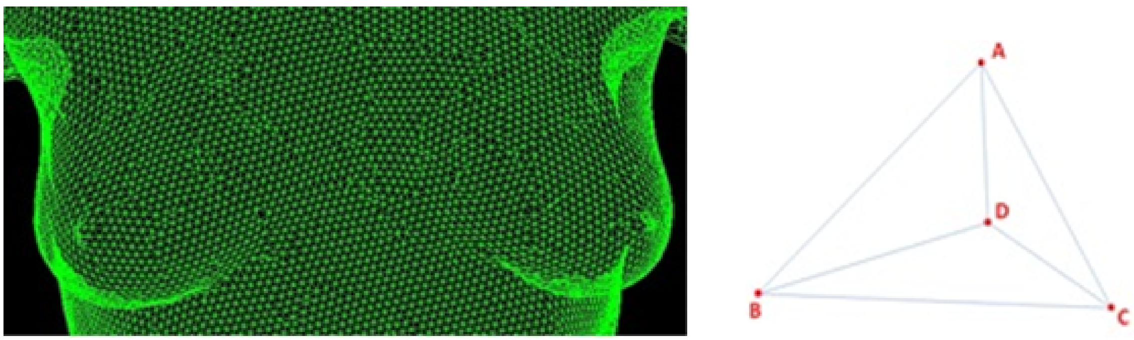


(a) (b)

Figure 4.6: (a) Triangular surface mesh for 3D image. (b) A point enclosed within a triangle in a 2D plane.

### 4.2.6 Optimization of SN and UM

To avoid operator bias introduced by manual fiducial points identification and location change of UM between multiple-visit images caused by breast reconstruction surgery, we optimize the registration of the SN and UM by searching for the most optimal corresponding points within a pre-determined neighborhood of $50mmX50mm$. The search region is $50mm$ along $x$ and $y$ directions respectively (Fig. 4.7). We select the size of the search region based on the reported intra- and inter- variation for manual fiducial point identification less than $15mm$ [10]. $50mmX50mm$ is large enough to avoid operator bias caused by manual fiducial points identification. The control points in the reference image are unchanged during optimization, whereas the thirteen control points in the target image are reselected based on the candidate locations of SN and UM in each iteration. For optimization, the SN and UM locations are updated synchronously. For each iteration, the 3D correspondence is determined by minimizing the cost function between control points from two images. The final SN and UM locations and transformation parameters are obtained from the iteration with the minimum cost value.

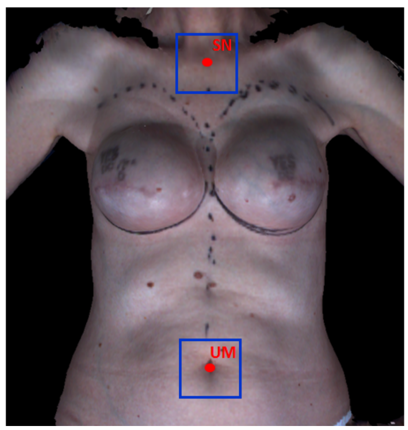


Figure 4.7: Search regions (shown by blue square frames, $50mmX50mm$) for SN and UM optimization in the target image

### 4.2.7 Rigid Registration

In rigid registration without scaling, only six transformation parameters are considered: ($\theta_x$,$\theta_y$,$\theta_z$,$t_x$,$t_y$, $t_z$), where $\theta_x$, $\theta_y$, and $\theta_z$ are rotation angles about X-, Y-, and Z-axes, respectively; and $t_x$, $t_y$, $t_z$ are the displacements (i.e., translation) along X-, Y-, Z-axes, respectively. During the registration, the transformation parameters are optimized iteratively.

Let $(x_i, y_i, z_i)$ and $(x_i^{'}, y_i^{'}, z_i^{'})$ be the coordinates for the $i$th point in the 3D images before and after transformation, then the transformed coordinates are determined as the product of matrices:

$$\begin{bmatrix} x_i' & y_i' & z_i' & 1 \end{bmatrix} = \begin{bmatrix} x_i & y_i & z_i & 1 \end{bmatrix} M_1 M_2 M_3 M_4 \tag{4.8}$$

where

$$M_1 = \begin{bmatrix} \cos\theta_z & \sin\theta_z & 0 & 0 \\ -\sin\theta_z & \cos\theta_z & 0 & 0 \\ 0 & 0 & 1 & 0 \\ 0 & 0 & 0 & 1 \end{bmatrix}$$

$$M_2 = \begin{bmatrix} 1 & 0 & 0 & 0 \\ 0 & \cos\theta_x & \sin\theta_x & 0 \\ 0 & -\sin\theta_x & \cos\theta_x & 0 \\ 0 & 0 & 0 & 1 \end{bmatrix}$$

$$M_3 = \begin{bmatrix} \cos\theta_y & 0 & -\sin\theta_y & 0 \\ 0 & 1 & 0 & 0 \\ \sin\theta_y & 0 & \cos\theta_y & 0 \\ 0 & 0 & 0 & 1 \end{bmatrix}$$

$$M_4 = \begin{bmatrix} 1 & 0 & 0 & 0 \\ 0 & 1 & 0 & 0 \\ 0 & 0 & 1 & 0 \\ t_x & t_y & t_z & 1 \end{bmatrix}$$

For the fifteen control points selected from each image, we create a complete graph in which each pair of points is connected by an edge (see Fig. 4.8b). Images from multiple clinical visits are then registered by determining the parameters for rigid transformation using the following cost function:

$$f = \sum_{i=1}^{n} d_i^2 + \frac{2}{(n-1)} \sum_{j=1}^{m} (\theta_j * l)^2 \tag{4.9}$$

Where $d_i$ is the Euclidean distance between the $i$th pair of control points in the two images. $\theta_j$ is the angle between $j$th pair of edges in two complete graphs. $n = 15$, is the total number of control points, $m = C_n^2$, which is the number of edges in one complete graph, and $l$ is the average edge length for all edges in two complete graphs. In the cost function, $\theta_j * l$ is the arc length. There are $n - 1$ edges in the complete graph for each point and two points share one edge, so the second term is normalized by a coefficient $\frac{2}{(n-1)}$. The second term represents the arc length of the angle between the corresponding edges in two images.

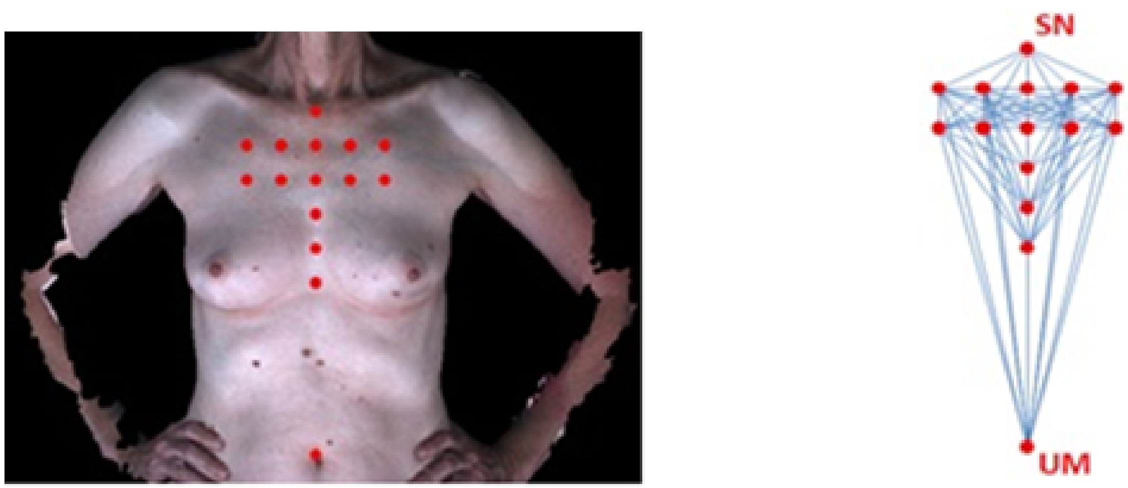


(a) (b)

Figure 4.8: (a) Control points selected on the torso for 3D correspondence. (b) Complete graph illustrating the fifteen selected control points.

The transformation parameters are optimized when the cost function is minimized. The optimization of the cost function is performed using the built-in optimization function *fminunc* which is a unconstrained nonlinear multivariable function in Matlab (Mathworks, Natick, MA). Since the Matlab functions may return a local optimum value, two methods are used to find the global optima: (1) Implementation of an iterative optimization process, by using the result of the previous iteration as the initial value for the next iteration, and (2) Implementation using the large scale option in Matlab for determining the next value during optimization, by computing the gradient, i.e., the partial differential for the 6 transformation parameters $[\frac{\partial f}{\partial \theta_x}, \frac{\partial f}{\partial \theta_y}, \frac{\partial f}{\partial \theta_z}, \frac{\partial f}{\partial t_x}, \frac{\partial f}{\partial t_y}, \frac{\partial f}{\partial t_z}]$.

## 4.3 Evaluation Metrics

To assess the performance of the proposed rigid registration algorithm for 3D multiple-visit images, we use the following evaluation metrics: (1) standard deviation to evaluate the convergence of SN and UM optimization; (2) root mean squared (RMS) distances; (3) angle between surface normal; (4) mutual information; (5) point fingerprint; and (6) $t$-test. The evaluation metrics are described as follows:

### 4.3.1 Standard Deviation

Let $\{x_i : i = 1, ...q\}$ be a collection of data. Then the mean $\mu$ and standard deviation $\sigma$ of the data set are defined as:

$$\mu = \frac{1}{q} \sum_{i=1}^{q} x_i \tag{4.10}$$

$$\sigma = \sqrt{\frac{\sum_{i=1}^{q} (x_i - \mu)^2}{q - 1}} \tag{4.11}$$

### 4.3.2 Root Mean Squared (RMS) Distance

The RMS distance $E_1$ between a set of points from the reference image and the set of corresponding points from the target image can be calculated using equation 4.12:

$$E_1 = \sqrt{\frac{1}{p}\sum_{i=1}^{p} d_i^2} \tag{4.12}$$

where $p$ is the number of points in the point set from one image, $d_i$ is the Euclidean distance between $i$th pair of points from the two point sets.

Given a point $P_0(x_0, y_0, z_0)$ from the reference image, its corresponding point in the target image can be defined as the nearest perpendicular foot in the 3D surface of the target image to $P_0$. The perpendicular foot is the intersection of the perpendicular passing through $P_0$ and the 3D surface of the target image. We determine the corresponding point by computing the perpendicular foot on the line, which passes through $P_0$ and is perpendicular to each triangle of the 3D mesh of the target image. The perpendicular foot, which locates inside the triangle and is nearest to $P_0$ is identified as the corresponding point. The method is described as follows:

Let $A(x_1, y_1, z_1), B(x_2, y_2, z_2), C(x_3, y_3, z_3)$ be the three vertices of a triangle $\Delta ABC$ and $(l, m, n)$ be the normal of the plane that $\Delta ABC$ lies in. Then:

$$\begin{cases} l = (y_2 - y_1)(z_3 - z_1) - (y_3 - y_1)(z_2 - z_1) \\ m = (z_2 - z_1)(x_3 - x_1) - (z_3 - z_1)(x - x_1) \\ n = (x_2 - x_1)(y_3 - y_1) - (x_3 - x_1)(y_2 - y_1) \end{cases} \tag{4.13}$$

Let $Q(x_q, y_q, z_q)$ be the perpendicular foot on the line passing through $P_0$ and perpendicular to the plane that $\Delta ABC$ lies in. Then the coordinates $x_q, y_q, z_q$ can be computed by equation 4.14:

$$\begin{cases} x_q = x_0 + tl \\ y_q = y_0 + tm \\ z_q = z_0 + tn \end{cases} \tag{4.14}$$

where $t = \frac{l(x_1-x_0)+m(y_1-y_0)+n(z_1-z_0)}{l^2+m^2+n^2}$

We project the $\Delta ABC$ to the plane, which is perpendicular to the largest component of normal $(l, m, n)$, i.e., the plane that has the largest projected area of $\Delta ABC$. The perpendicular foot $Q$ is checked inside or outside $\Delta ABC$ using method described in subsection 4.2.5. If $Q$ is inside $\Delta ABC$, then the Euclidean distance between $P_0$ and $Q$ is calculated using equation 4.15 and compared to those from other triangles of the mesh of the target image. The perpendicular foot, which lies inside the triangle and has the shortest Euclidean distance to $P_0$ is identified as the corresponding point.

$$|P_0Q| = \sqrt{(x_q - x_0)^2 + (y_q - y_0)^2 + (z_q - z_0)^2} \tag{4.15}$$

### 4.3.3 Angle between Surface Normals

The angle between surface normals of two registered 3D images is also used to evaluate the registration accuracy in this research. Given a set of points $P\{P_i : i = 1, \ldots p\}$ from a 3D image and a radius $R$, the surface normal of the image can be calculated as follows:

For each point $P_i$ in the set P, we extract a patch $T_i$ from the mesh of the 3D image, in which all the points have Euclidean distances to $P_i$ less than R. For each triangle $\Delta_j$ in $T_i$, we calculate the normalized normal $\overrightarrow{n_j}$ and area $s_j$ of the triangle. Let $A$, $B$, and $C$ be the three vertices of the triangle $\Delta_j$, then

$$\overrightarrow{n_j} = \frac{\overrightarrow{AB} X \overrightarrow{AC}}{|\overrightarrow{AB} X \overrightarrow{AC}|} \tag{4.16}$$

where "$X$" means cross product of vectors, "||" is the 2-norm, i.e., the length of the vector.

$$s_j = \sqrt{u(u-a)(u-b)(u-c)} \tag{4.17}$$

where $a$, $b$, and $c$ are length of the three edges of the $\Delta_j$, $u = \frac{1}{2}(a+b+c)$.

The total normal of the patch $T_i$ is the weighted sum of the normalized normals for all triangles in the patch, where the weights are the triangle areas. The normalized total normal $\overrightarrow{N_i}$ and the total area $S_i$ for the patch $T_i$ are:

$$\overrightarrow{n_i} = \frac{\sum_{j=1}^{k} s_j \overrightarrow{n_j}}{|\sum_{j=1}^{k} s_j \overrightarrow{n_j}|} \tag{4.18}$$

$$s_i = \sum_{j=1}^{k} s_j \tag{4.19}$$

where $k$ is the number of triangles in patch $T_i$.

The total normal $\overrightarrow{N}$ of the 3D image is the weighted sum of the normalized total normals of all patches for points in set $P$, where the weight is the total areas of the patches.

$$\overrightarrow{N} = \sum_{i=1}^{p} S_i \cdot \overrightarrow{N_i} \tag{4.20}$$

where $p$ is the number of points in set $P$.

Let $\overrightarrow{N}$ and $\overrightarrow{N'}$ be total surface normals of two 3D images respectively, the angle $E_2$ between surface normals can be calculated using the dot product of them.

$$E_2 = \cos^{-1} \frac{\overrightarrow{N} \cdot \overrightarrow{N'}}{|\overrightarrow{N}||\overrightarrow{N'}|} \tag{4.21}$$

### 4.3.4 Mutual Information

The mutual information [74] of the two images is computed to evaluate the correspondence achieved following the registration of two 3D images. After registration, the two 3D surface images are projected onto XY, XZ, and YZ planes respectively. In each plane, two intensity-based 2D images corresponding to the two 3D images are created as follows: First, the 2D projections of each of the two images in the selected plane (i.e., XY, YZ, or XZ) are examined, and the dimensions of a bounding box that entirely encloses both the 2D projections are determined. Next, two new images at the size of the bounding box are created. For each pixel in the new image, the projected points from the corresponding 3D image are counted and normalized by the total number of the points in the 3D image. These normalized values are the intensities of the 2D image. For each 2D image, the intensities are scaled to be $0 \sim 255$ so that the gray level intensities are integers. The mutual information for the two intensity-based 2D images is computed using the following equation:

$$M(A;B) = H(A) + H(B) - H(A,B) \tag{4.22}$$

where $A$ and $B$ represent the two 2D images, $H(A)$ and $H(B)$ are the marginal entropies, and $H(A,B)$ is the joint entropy of $A$ and $B$. The 3 entropies for 2D intensity-based images are defined as:

$$H(A) = -\sum_{i=0}^{255} P_A(i) \log_2 P_A(i) \tag{4.23}$$

$$H(B) = -\sum_{i=0}^{255} P_B(i) \log_2 P_B(i) \tag{4.24}$$

$$H(A,B) = -\sum_{i=0}^{255} \sum_{j=0}^{255} P_{A,B}(i,j) \log_2 P_{A,B}(i,j) \tag{4.25}$$

where $P_A(i)$ and $P_B(i)$ are probabilities of pixels which contain the intensity value $i$ in image $A$ and $B$ respectively, and $P_{A,B}(i,j)$ is the probability of intensity pair $(i,j)$ where $i$ is the intensity value for a pixel in $A$ and $j$ is the that for the corresponding pixel in $B$. The total number of intensity pairs is $256X256$. $P_A(i)$, $P_B(i)$, $P_{A,B}(i,j)$ can be calculated as:

$$P_A(i) = \frac{f(i)}{N} \tag{4.26}$$

$$P_B(i) = \frac{g(i)}{N} \tag{4.27}$$

$$P_{A,B}(i) = \frac{f(i,j)}{N^2} \tag{4.28}$$

Where $N$ is the total number of pixels in image $A$ (or $B$). $f(i)$ and $g(i)$ are numbers of pixels with intensity value $i$ in $A$ and $B$ respectively. $f(i,j)$ is the number of intensity pair $(i,j)$, where $i$ is the intensity value for a pixel in $A$ and $j$ is that for the pixel in $B$.

The mutual information of the two 3D images can be calculated as:

$$M = \sqrt{M_{xy}^2 + M_{xz}^2 + M_{yz}^2} \tag{4.29}$$

where $M_{xy}$, $M_{xz}$, and $M_{yz}$ are mutual information for projections onto XY, XZ, and YZ planes respectively.

### 4.3.5 Point Fingerprint

A 3D surface representation scheme called point fingerprints is used to qualitatively evaluate the results achieved from 3D image registration. A point fingerprint is a set of 2D contours that are projections of geodesic circles onto a given tangent plane in local/global coordinate system [64]. In this study, planes along Z-axis, which are parallel to XY plane are used to cut the surface of the 3D image to get a series of parallel circles. The point fingerprint contours are obtained by projecting the points of circles onto the XY plane (Fig. 4.9). To compare the torso matching result, the point fingerprints of two related images are overlaid in a single 2D graph. The z-buffer algorithm is used to display overlapping points from the two point fingerprints, whereby if two points in different images project onto the same pixel, the one with larger z-coordinate is plotted [75].

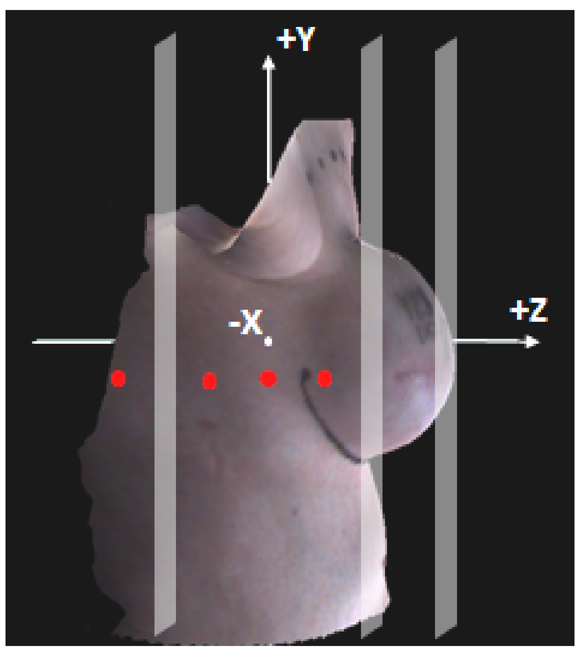


Figure 4.9: Parallel planes spaced at equal intervals placed depth-wise (Z-axis) along the surface of 3D image.

### 4.3.6 $t$-test

A paired $t$-test can be used to compare two different registration algorithms that applied to the same datasets and shows whether the registration errors from the two algorithms are significantly different or not. The $t$ value can be calculated by:

$$t = \frac{\bar{d}}{S_d/\sqrt{n}} \tag{4.30}$$

where $\bar{d}$ is the mean of difference between registration errors for the two compared algorithms , $S_d$ is the standard deviation, $n$ is the size of the dataset.

## 4.4 Existing Algorithm for Comparison

An ICP algorithm [76] is used as a control (i.e., current approach) in order to provide a benchmark for comparison with the proposed algorithm. This ICP method took root mean squared distances between a set of control points in the reference 3D image and the set of corresponding points on the target one as the cost function, and used the kDtree method for nearest neighbor search to find the corresponding points during registration.

The nearest neighbor search using kDtree in [76] was done in the following algorithmic way:

1. kDtree construction: Points cloud of the target image can be sequentially divided into two equally sized sets based on their $x$, $y$ and $z$ coordinates in turn. The point cloud is split by finding the median of all points' $x$ coordinates. The median point becomes the root of the tree. Next, the two resulting subsets are split based on the median of their $y$ coordinates. Then, the four resulting

subsets are split based on the median of their $z$ coordinates, and so on. The process, known as binary space paritioning, generates a balanced binary tree containing all points of the points cloud in the target image.

2. Corresponding point search (nearest neighbor search): Locating the nearest neighbor to a control point $p$ from the reference image within points cloud of the target image can be done as follows:

   (a) Move down the kDtree starting at the root comparing coordinates according to the actual splitting dimension until a leaf is reached.

   (b) Mark the point at the located leaf node as current best, and calculate the distance $d$ between $p$ and current best.

   (c) Move up one level in the tree and determine the distance from $p$ to the current node. If the distance is shorter than $d$, update current node as current best and the distance to it as $d$.

   If the distance from $p$ to the current nodes' splitting plane is longer than $d$, exclude current nodes' other side branch and continue moving upwards. Otherwise the nodes' other side branch is searched through just like the whole tree.

   (d) When the root is reached and all necessary side branches have been searched, choose the shortest of all candidates from the main search and eventual sub branch searches.

## 4.5 Datasets

The algorithm was validated using images of a plastic mannequin, and following validation the algorithm was applied to multi-visit images acquired from patients undergoing breast reconstruction surgery at The University of Texas MD Anderson Cancer Center (MDACC). A representative mannequin image is shown in Fig. 4.10. The mannequin was placed on the tilt table of the custom-designed imaging system described in Chapter 3. The reclining angle of the tilt table was changed and five images were acquired in positions upright (90 degrees), 60 degrees, 45 degrees, 30 degrees, and supine (0 degree). Since the cameras were fixed on the tilt table, there is no angle change between the originally acquired mannequin images. The only difference between them is the noise (Fig. 4.10b). We rotated the mannequin images acquired at tilt table reclining angles 60 degrees, 45 degrees, 30 degrees, and supine (0 degree) using BR software [77] to obtain the images at 60 degrees, 45 degrees, 30 degrees, and supine (0 degree) positions (Fig. 4.11) to validate our proposed algorithm. Multiple-visit images from the same patient were acquired at different clinical visits during their treatment process. Female patients undergoing breast reconstruction surgery at the University of Texas MD Anderson Cancer Center were recruited under an Institutional Review Board (IRB) approved protocol. 3D images from 34 patients were used in this study. The ethnicity, race, age, and BMI information for the 34 patients are listed in Table 4.1.

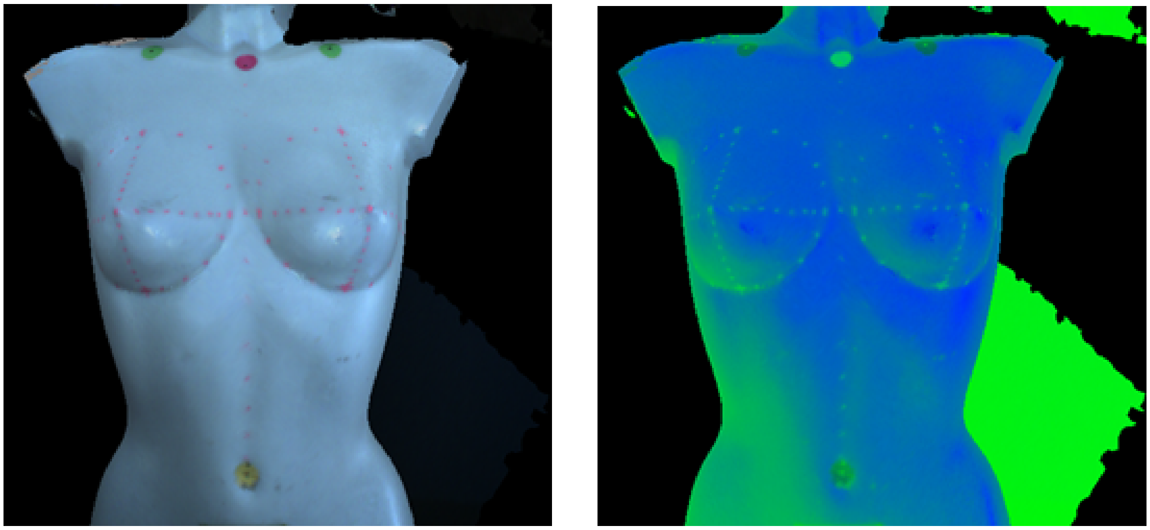

(a) (b)

Figure 4.10: Example of mannequin images. (a) Mannequin image with original texture. The color points were manually annotated by a plastic surgeon prior to imaging. (b) Mannequin image with modified texture to display the noise (green areas out of the boundary of mannequin)

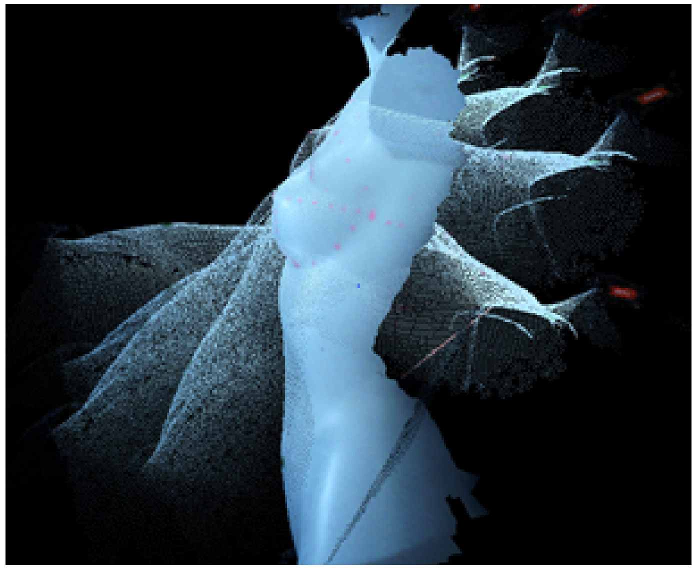

Figure 4.11: Lateral view of upright (90°), 60°, 45°, 30°, and supine (0°) mannequin images. Mannequin images with 60°, 45°, 30°, and supine (0°) were created using BR software by rotating images acquired from the custom-designed imaging system and only displayed the point clouds for better visualization.

Table 4.1: Demographics of 34 patients

| **No.** | **Patient ID** | **Ethnicity** | **Race** | **Age** | **BMI** | | | |
|---|---|---|---|---|---|---|---|---|
| | | | | | **Visit1** | **Visit2** | **Visit3** | **Visit4** |
| 1 | 7 | NotHispanic_Latino | White | 54 | 21.5 | 20.6 | NA | NA |
| 2 | 15 | NotHispanic_Latino | White | 55 | 33.7 | 33.8 | NA | NA |
| 3 | 24 | NotHispanic_Latino | BAA | 51 | 34.7 | 33.3 | NA | NA |
| 4 | 38 | NotHispanic_Latino | White | 36 | 26.9 | 19.6 | NA | NA |
| 5 | 42 | NotHispanic_Latino | White | 49 | 28.2 | 27.7 | 28.4 | 28.4 |
| 6 | 48 | NotHispanic_Latino | White | 49 | 24.3 | 24.6 | NA | NA |
| 7 | 52 | NotHispanic_Latino | BAA | 47 | 29.9 | 33.6 | 35.3 | NA |
| 8 | 56 | NotHispanic_Latino | White | 54 | 25.9 | 25.9 | 27.4 | 26.3 |
| 9 | 57 | NotHispanic_Latino | White | 63 | 24.8 | 25.6 | 26.4 | NA |
| 10 | 67 | Hispanic_Latino | White | 50 | 23.4 | 25.6 | 26.4 | NA |
| 11 | 68 | NotHispanic_Latino | White | 54 | 22.4 | 21.9 | 22.3 | 22.8 |

| | | | | | | | | |
|---|---|---|---|---|---|---|---|---|
| 12 | 70 | NotHispanic_Latino | White | 52 | 39.6 | 35.4 | NA | 35.1 |
| 13 | 76 | Hispanic_Latino | White | 43 | 20.6 | 19 | NA | NA |
| 14 | 78 | NotHispanic_Latino | White | 40 | 21.9 | 21.8 | 21.8 | NA |
| 15 | 81 | NotHispanic_Latino | White | 46 | 38.4 | 39.2 | NA | NA |
| 16 | 82 | NotHispanic_Latino | White | 59 | 31.6 | 32.4 | 33 | NA |
| 17 | 83 | NotHispanic_Latino | White | 51 | 23.3 | 26 | NA | NA |
| 18 | 86 | NotHispanic_Latino | White | 53 | 32.9 | 35.7 | 34.3 | NA |
| 19 | 91 | NotHispanic_Latino | White | 41 | 21.1 | 19.1 | NA | NA |
| 20 | 101 | NotHispanic_Latino | BAA | 40 | 25.3 | 24.9 | NA | NA |
| 21 | 103 | NotHispanic_Latino | White | 52 | 30.2 | 30 | NA | NA |
| 22 | 109 | NotHispanic_Latino | White | 52 | 30.7 | 31.1 | NA | NA |
| 23 | 113 | NotHispanic_Latino | White | 54 | 35.2 | 25.9 | 25.8 | NA |
| 24 | 117 | NotHispanic_Latino | White | 58 | 30.2 | 31.6 | 28.7 | NA |
| 25 | 126 | Hispanic_Latino | White | 34 | 25.4 | 25.4 | 24 | NA |
| 26 | 127 | NotHispanic_Latino | White | 55 | 31.1 | 31.7 | 31.7 | NA |
| 27 | 131 | NotHispanic_Latino | White | 51 | 20.4 | 19.5 | 18.8 | NA |
| 28 | 133 | NotHispanic_Latino | White | 46 | 34.4 | 30.3 | NA | NA |
| 29 | 139 | NotHispanic_Latino | White | 39 | 33.7 | 35.5 | 38 | NA |
| 30 | 159 | NotHispanic_Latino | White | 30 | 23.9 | 24.6 | 23.8 | NA |
| 31 | 163 | NotHispanic_Latino | White | 37 | 26.2 | 26.3 | 24 | 25 |
| 32 | 177 | NotHispanic_Latino | White | 55 | 25.5 | NA | 26.2 | NA |
| 33 | 182 | NotHispanic_Latino | White | 43 | NA | 25.7 | 23.9 | NA |
| 34 | 193 | NotHispanic_Latino | White | 54 | 32.7 | 32 | 32.4 | NA |

Note: BAA - Black_AfricanAmerican

## 4.6 Results

### 4.6.1 Convergence of SN and UM Optimization

The initial manual selection of the fiducial points, SN and UM can influence the registration process due to: (1) operator bias introduced by manual fiducial points identification, and (2) location change of UM between images caused by breast reconstruction surgery. The location of UM can change between preoperative imaging and postoperative imaging for patients undergoing TRAM or DIEP flaps types of autologous tissue breast reconstruction. We optimize the SN and UM locations in the target image to avoid registration error caused by SN and UM location differences in the two multiple-visit images.

To demonstrate the convergence of our optimization method, we simulate the SN and UM location changes in mannequin images as follows: the target image of the registration has significant changes, i.e., as large as $20mm$ in the locations of the SN and/or UM. The location of UM is clear on the torso and it is in a small area. Consider the size of the neck, the SN is not very difficult to identify. So $20mm$ is large enough to simulate the largest possible operator bias in SN and UM. In the simulation, each of the two points, SN and UM have five different relocations: original location (manually identified location), up, down, left and right at a displacement of $20mm$ from the original location respectively (Fig. 4.12). One of the SN relocations and one of the UM relocations are combined to be one simulation case. A total of twenty-five cases are evaluated.

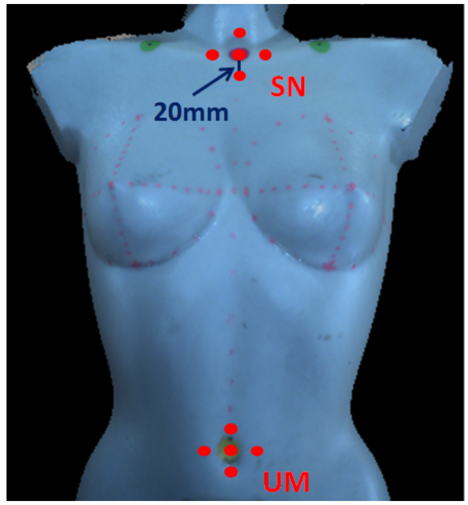


Figure 4.12: Simulation of operator bias and breast reconstruction caused changes on SN and UM. The intermediate points among the five points are original locations of SN and UM respectively. The relocated places are up, down, left and right at a $20mm$ distance from the original location.

Registration was performed for each pair of the five mannequin images (upright, 60 degrees, 45 degrees, 30 degrees, and supine). There are $C_5^2 = 10$ pair of images in total. Experimental results for twenty-five cases are provided for each pair of images. We use the manually identified SN and UM in the target image as the ground truth to demonstrate the convergence of our SN and UM optimization method. Table 4.2 presents the means and standard deviations computed using equations 4.10 and 4.11. Mean represents the average Euclidean distance from the optimized SN/UM locations to the ground truth for twenty-five cases. Standard deviation measures the amount of variation to the mean based on the Euclidean distance. From Table 4.2, we can see that the optimization error for SN is no more than $1.406 \pm 0.0008mm$, and that for UM is no more than $1.0668 \pm 0.0021mm$ for all ten registrations. For all 250 cases of ten registrations, each of the 250 optimized SN (or UM) locations has a distance to its ground truth. We computed the percentage of optimized SN (or UM) over 250 cases within different radius (distance) to the ground truth and displayed in Fig. 4.13. In Fig. 4.13a, we can see that the percentage of optimized SN approach 1 when the radius is great than 1.4$mm$. In Fig. 4.13b, the percentage of optimized UM approach 1 when the radius is great than 1.0$mm$.

Table 4.2: Mean and standard deviation for optimized SN and UM for twenty-five simulation cases

| **Images for Registration** | **SN** | | **UM** | |
|---|---|---|---|---|
| | **Mean (mm)** | **Standard Deviation** $(mm)$ | **Mean (mm)** | **Standard Deviation** $(mm)$ |
| Upright vs Supine | 1.406 | 0.0008 | 0.9541 | 0.0015 |
| Upright vs $30^o$ | 0.1959 | 0.00089 | 0.5305 | 0.00073 |
| Upright vs $45^o$ | 0.1793 | 0.00072 | 0.4582 | 0.00026 |
| Upright vs $60^o$ | 0.4115 | 0.00125 | 0.6775 | 0.00044 |
| $30^o$ vs $45^o$ | 0.1522 | 0.00089 | 0.1231 | 0.00043 |
| $30^o$ vs $60^o$ | 0.3138 | 0.00071 | 0.4675 | 0.00253 |
| $30^o$ vs Supine | 1.233 | 0.00019 | 0.938 | 0.00146 |
| $45^o$ vs $60^o$ | 0.2016 | 0.001 | 0.6067 | 0.00258 |
| $45^o$ vs Supine | 1.0274 | 0.00058 | 1.0668 | 0.0021 |
| $60^o$ vs Supine | 0.8864 | 0.05126 | 0.607 | 0.08295 |

### 4.6.2 Comparison with Existing ICP Algorithm

#### 4.6.2.1 Results Comparison for Mannequin Images

The proposed algorithm is validated using the mannequin images. For each pair of the five mannequin images (upright, 60 degrees, 45 degrees, 30 degrees, and supine), we do the registration using our proposed algorithm and an existing ICP algorithm [76].

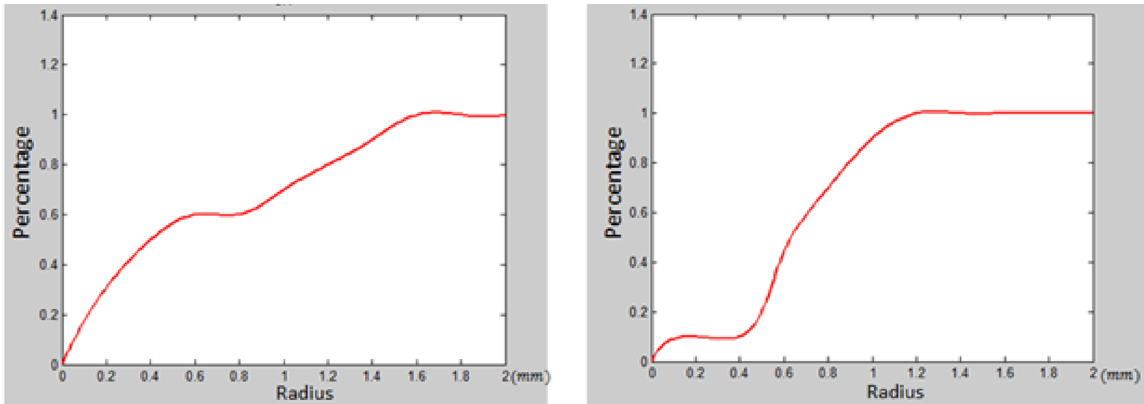


(a) (b)

Figure 4.13: Percentage of optimized SNs and UMs within a radius of sphere centered at ground truth. (a) Plot for SN.(b) Plot for UM. Where horizontal axis shows the radius of a sphere centered on the ground-truth location, and the vertical axis shows percentage of solution locations within the radius of a sphere for all 250 cases of ten registrations

The torso transformation between mannequin images is rigid, but the noise in the two images may not match and can cause registration error. Thus we run the ICP algorithm for three different worst rejection rates: 0 (without worst rejection), 30%, and 60%. The worst rejection means to reject a given percentage of the control point pairs, which have large Euclidean distances between them, from the two images as the outliers before computing the cost function.

Data for representative mannequin images (upright and 60 degrees) is presented in Fig. 4.14- 4.17. Fig. 4.14 shows 3D torsos of the two images. Fig. 4.15- 4.17 shows the data before registration and those achieved following rigid transformation using our proposed algorithm and existing ICP algorithm respectively. The upright image is reference image and untransformed, and the image with 60 degrees is the target image and transformed to the reference image during the registration. To facilitate viewing, the 3D torso images are cropped to display only the area of the upper torso encompassing the breast mounds. The upright image is shown in red, and the image with 60 degrees is shown in blue. Fig. 4.15 represents the point clouds of the two images (bottom-up-view of breasts). There are 108 surgeon-annotated points on the mannequin (Fig. 4.14). We use this set of points to evaluate the registration error for mannequin images. Fig 4.16 presents the surgeon annotated points (from upright image) and their corresponding points (calculated from 60 degrees image using method described in subsection 4.3.2). Fig. 4.17 shows the 2D point fingerprints. Original data for images before registration are displayed in Fig. 4.15- 4.17(a). Data achieved following rigid transformation using our proposed algorithm are presented in Fig. 4.15- 4.17(b). Those achieved from registration using existing ICP algorithms with worst rejection rates 0, 30%, 60% are listed in Fig. 4.15- 4.17 (c)-(e) respectively.

As seen in Fig. 4.15- 4.17(a), the original surfaces from upright mannequin image (red) and mannequin image with 60 degrees (blue) are not matched. Following the implementation of the proposed registration algorithm, correspondence is achieved between the two images (Fig. 4.15- 4.17(b)). The existing ICP algorithm without worst rejection (Fig. 4.15- 4.17(c)) has much larger registration error than both with worst rejection rates 30% (Fig. 4.15- 4.17(d)) and 60% (Fig. 4.15- 4.17(e)) due to the noise in the 3D mannequin images. By visualization, the experimental results in Fig. 4.15- 4.17(b), (d) and (e) show that our proposed algorithm and existing ICP algorithm with both of worst rejection rates 30% and 60% can achieve perfect registration due to the absolutely rigid transformation between torsos in 3D mannequin images. And by value, our proposed algorithm has less registration error: the RMS distance $E_1$ between surgeon marked points from the upright image and their corresponding points from the transformed 60 degrees image for our proposed algorithm, existing ICP algorithm with worst rejection rates 30% and 60% are $0.1515mm$, $0.1942mm$, and $0.1974mm$ respectively.

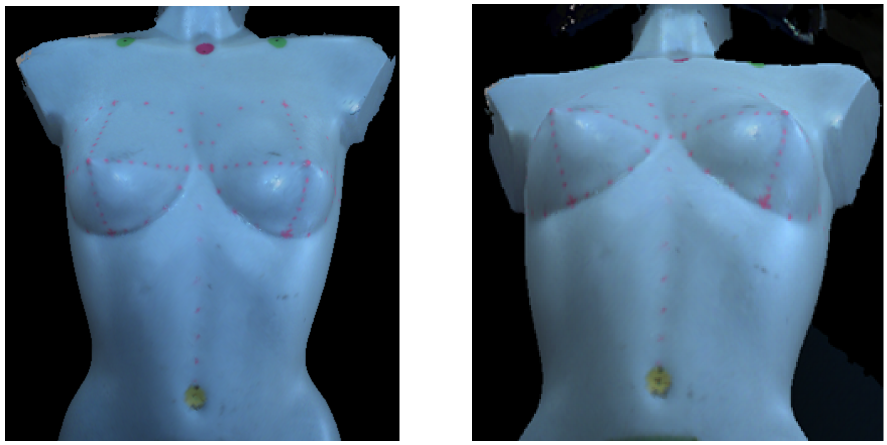

(a) (b)

Figure 4.14: Example of mannequin images used for algorithm validation. (a) Upright image. (b) Image with 60 degrees. The color points were manually annotated by a plastic surgeon prior to imaging, which can be used to evaluate registration error.

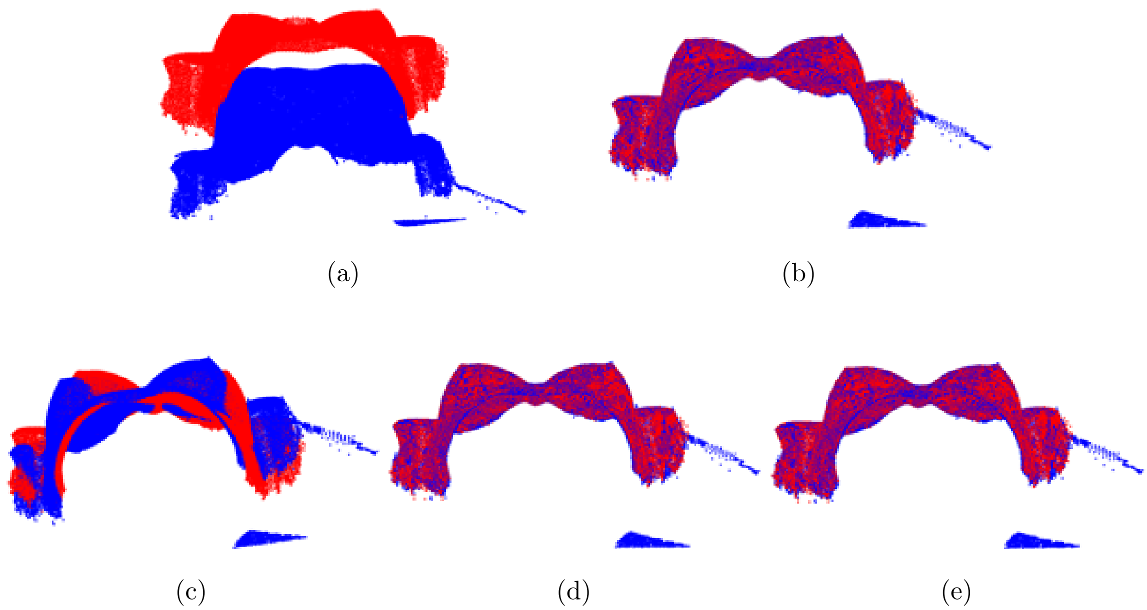

Figure 4.15: Example of registration for mannequin images (upright vs $60^o$, upright image is in red, $60^o$ image is in blue). (a) Original point clouds (bottom-up-view of breasts) showing unmatched images (before registration). (b) 3D correspondence of point cloud achieved following rigid transformation using the proposed algorithm. (c) 3D correspondence of point cloud achieved using the existing ICP algorithm without worst rejection. (d) 3D correspondence of point cloud achieved using the existing ICP algorithm with worst rejection rate 30%. (d) 3D correspondence of point cloud achieved using the existing ICP algorithm with worst rejection rate 60%.

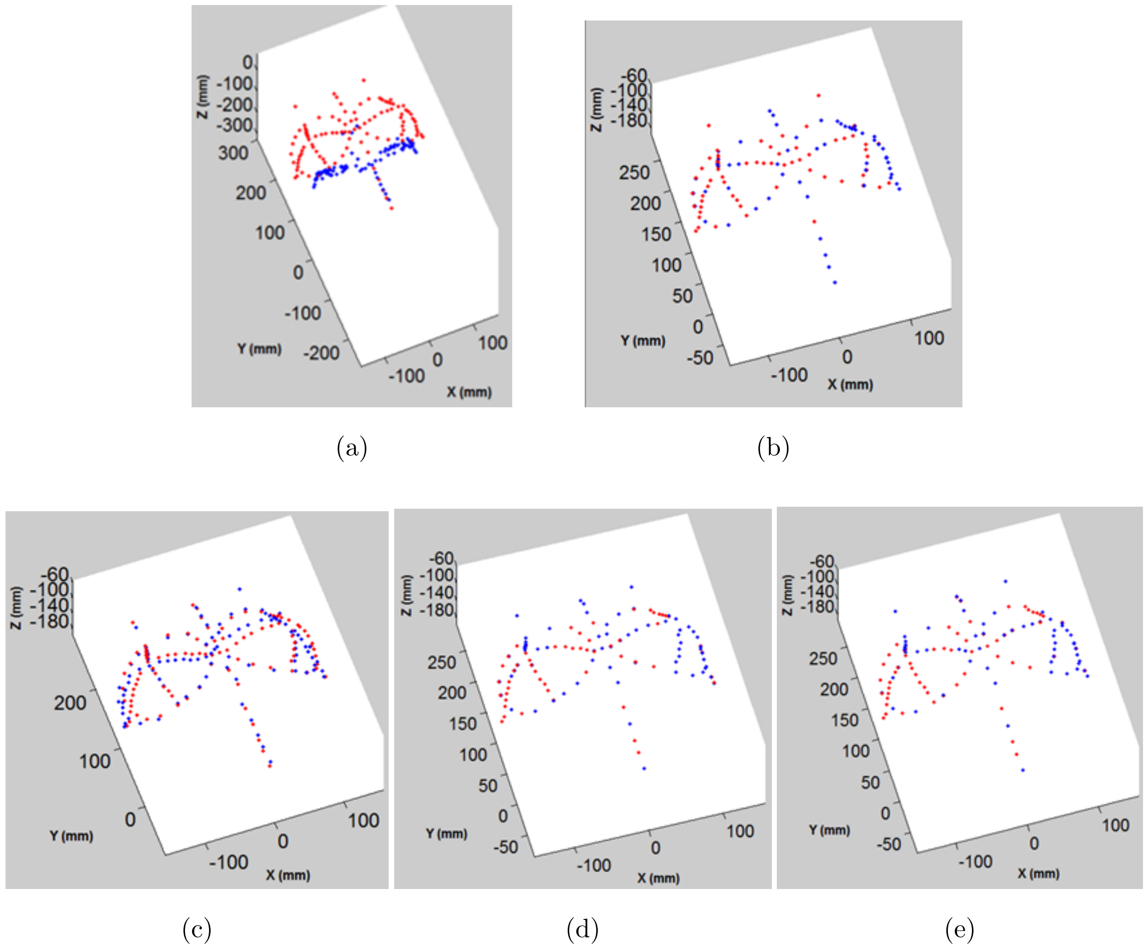


Figure 4.16: Example of registration for mannequin images (upright vs $60^o$), Surgeon annotated points from upright image are in red color. Corresponding points from $60^o$ image are in blue color. (a) Surgeon annotated points and corresponding points from unmatched images. (b) Surgeon annotated points and corresponding points from registered images achieved using the proposed algorithm. (c) Surgeon annotated points and corresponding points from registered images achieved using the existing ICP algorithm without worst rejection. (d) Surgeon annotated points and corresponding points from registered images achieved using the existing ICP algorithm with worst rejection rate 30%. (d) Surgeon annotated points and corresponding points from registered images achieved using the existing ICP algorithm with worst rejection rate 60%.

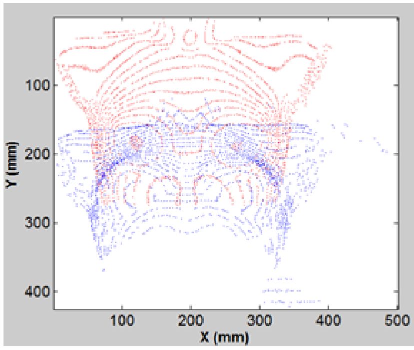


(a)

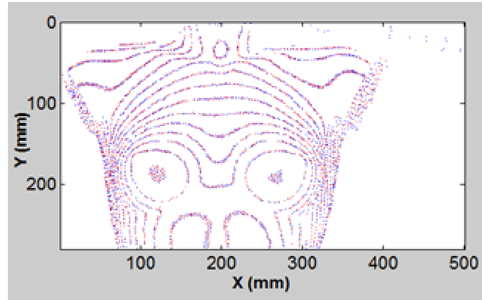


(b)

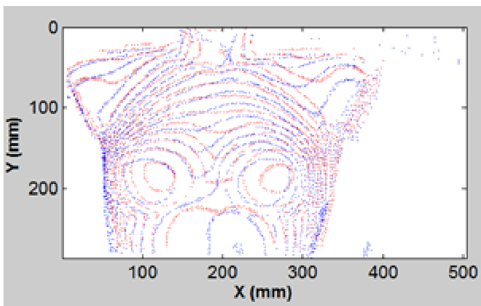


(c)

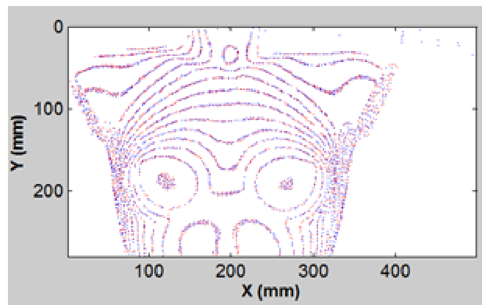


(d)

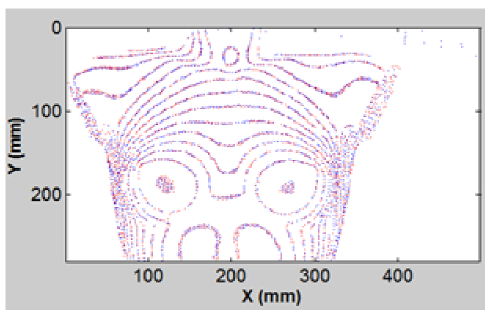


(e)

Figure 4.17: Example of registration for mannequin images (upright vs $60^o$, upright image is in red, $60^o$ image is in blue). (a) 2D point fingerprints showing unmatched images. (b) 2D point fingerprints for registered images achieved using the proposed algorithm. (c) 2D point fingerprints for registered images achieved using the existing ICP algorithm without worst rejection. (d) 2D point fingerprints for registered images achieved using the existing ICP algorithm with worst rejection rate 30%. (d) 2D point fingerprints for registered images achieved using the existing ICP algorithm with worst rejection rate 60%.

The average data of the ten registrations for the five mannequin images are shown in Table 4.3. For each pair of registered images, $E_1$ is the RMS distance between 108 surgeon annotated points from the reference mannequin image and their corresponding points from the transformed target mannequin image. $E_2$ is the angle between surface normals for two images calculated from surgeon annotated points and their corresponding points using method described in subsection 4.3.3. The surface normals are computed from patches around points with radius $10mm$ and $15mm$ respectively, which are large enough to evaluate the orientation of the surface around the points. The relative error $E_r$, which is calculated by equation 4.31, is employed to further observe the improvement of our proposed algorithm.

$$E_r = \frac{E_{ICP} - E_{our}}{E_{our}} * 100\% \tag{4.31}$$

where $E_{ICP}$ is the registration error of the existing ICP algorithm, and $E_{our}$ is that of our proposed algorithm for the ten registrations.

From Table 4.3, we can see that our proposed algorithm outperforms the existing ICP algorithm with all of the three worst rejection rates: 0, 30%, and 60%. The ICP algorithm without worst rejection has the worst performance: the relative error of average $E_1$ is 1592.86% comparing to the proposed algorithm. This is caused by the noise in the mannequin images, which are used for registration. Without worst rejection, all the image points and noise are considered for registration. The registration results are similar when the worst rejection rates are 30% and 60% (average $E_1$ are $0.2227 \pm 0.0467mm$ and $0.2219 \pm 0.0439mm$ respectively), while our proposed algorithm is a little better than ICP with both of these two rejection rates: relative error of average $E_1$ is 3.03% and 2.66%; improvement for average $E_2$ is between 8.91% and 18.91% with both patch radius $10mm$ and $15mm$; and also, the proposed algorithm has the largest mutual information value $M$. The negative relative error $E_r$ for $M$ means that average mutual information value $M$ for our proposed algorithm is larger than those from ICP algorithm. Larger mutual information value represents better registration.

Table 4.3: Registration error comparison for Mannequin images

| **Algorithms** | | **Average $E_1$** | **Average $E_2$** | | **Average M** |
|---|---|---|---|---|---|
| | | | $R = 10mm$ | $R = 15mm$ | |
| **Proposed Algorithm** | | (0.2162 ±0.0588) mm | (0.0874 ±0.0479)° | (0.0762 ±0.0286)° | 5.5736 ±0.4381 |
| **Existing ICP Algorithm** | $WR = 0$ | (3.6599 ±5.7140) mm | (1.7804 ±2.7310)° | (1.7455 ±2.6521)° | 5.3982 ±0.6006 |
| | $WR = 30\%$ | (0.2227 ±0.0467) mm | (0.0953 ±0.0629)° | (0.0840 ±0.0350)° | 5.5600 ±0.4349 |
| | $WR = 60\%$ | (0.2219 ±0.0439) mm | (0.0952 ±0.0659)° | (0.0906 ±0.0471)° | 5.5595 ±0.4346 |
| **Relative Error $E_r$** | $WR = 0$ | 1592.86% | 1936.40% | 2189.84% | −3.15% |
| | $WR = 30\%$ | 3.03% | 8.96% | 10.18% | −0.24% |
| | $WR = 60\%$ | 2.66% | 8.91% | 18.91% | −0.25% |

$WR$: worst rejection.

#### 4.6.2.2 Results Comparison for Multiple-Visit Image

Following algorithm validation using mannequin images, the proposed algorithm was tested using multiple-visit images from patients. Comparisons were performed for each pair of multiple-visit images of the same patient. Images from 34 patients were processed for a total of 83 registrations. Representative data for a pair of multiple-visit images from one patient is presented in Fig. 4.18- 4.21. The image from the initial visit (Fig. 4.18a) was the reference image and the image from the subsequent visit (Fig 4.18b) was the target image and registered to the image from the initial visit. The reference image is shown in red, and the target image is shown in blue. Fig. 4.19 represents the point clouds of the two images (bottom-up-view of breasts). Fig 4.20 presents the fifteen control points (two manually selected fiducial points SN and UM and thirteen automatically calculated control points) from the reference image and their corresponding points from the target image. Fig. 4.21 shows the 2D point fingerprints. Original data for images before registration are displayed in Fig. 4.19- 4.21(a). Data achieved following rigid transformation using our proposed algorithm are presented in Fig. 4.19- 4.21(b). Those achieved from registration using existing ICP algorithms with worst rejection rates 0, 30%, 60% are listed in Fig. 4.19- 4.21 (c)-(e) respectively.

As seen in the Fig 4.19- 4.21(b), the proposed algorithm achieved 3D correspondence as is evident by the overlap of the chest walls. Note that the mismatches in the poses of the patient can be visualized in the areas of the arms. Further the mismatches are noted in the region of the left breast due to the surgical deformations present. The existing ICP algorithm (Fig. 4.19- 4.21(c)-(e)) show relatively poor performance. From Fig. 4.20(c)-(e), we can see that the ICP with 30% rejection achieved better registration than other two worst rejection rates. Comparatively, our proposed algorithm can outperform the existing ICP algorithm with all three worst rejection rates: the RMS distance $E_1$ between the fifteen control points and their corresponding points in the registered images using the proposed algorithm, existing ICP algorithm with worst rejection rates 30% (showing best registration result in all three worst rejection rates) are $0.7253mm$ and $1.4483mm$ respectively; and the mutual information M are 5.9276 and 5.9175 respectively.

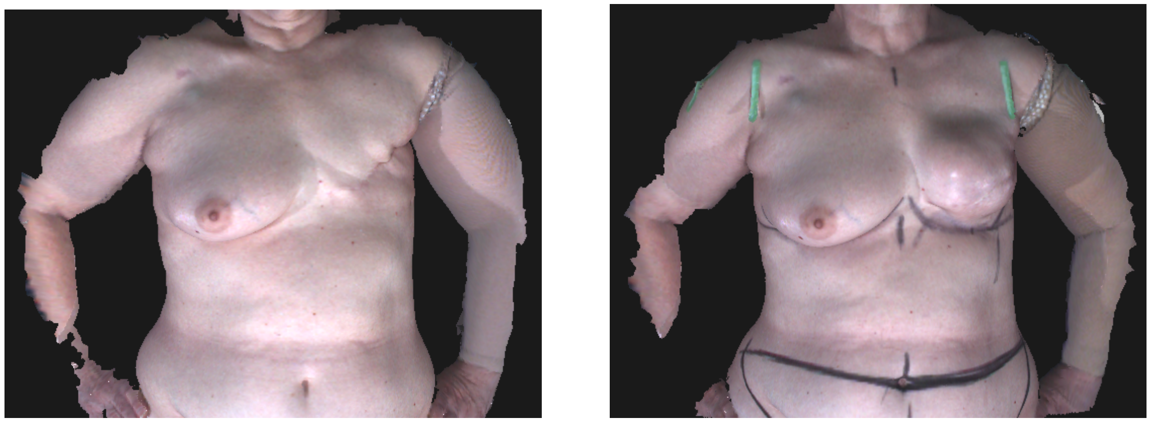

(a) (b)

Figure 4.18: Example of multiple-visit images from individual patient used for algorithm validation. (a) 3D torso from initial visit (reference image). (b) 3D torso from subsequent visit (target image).

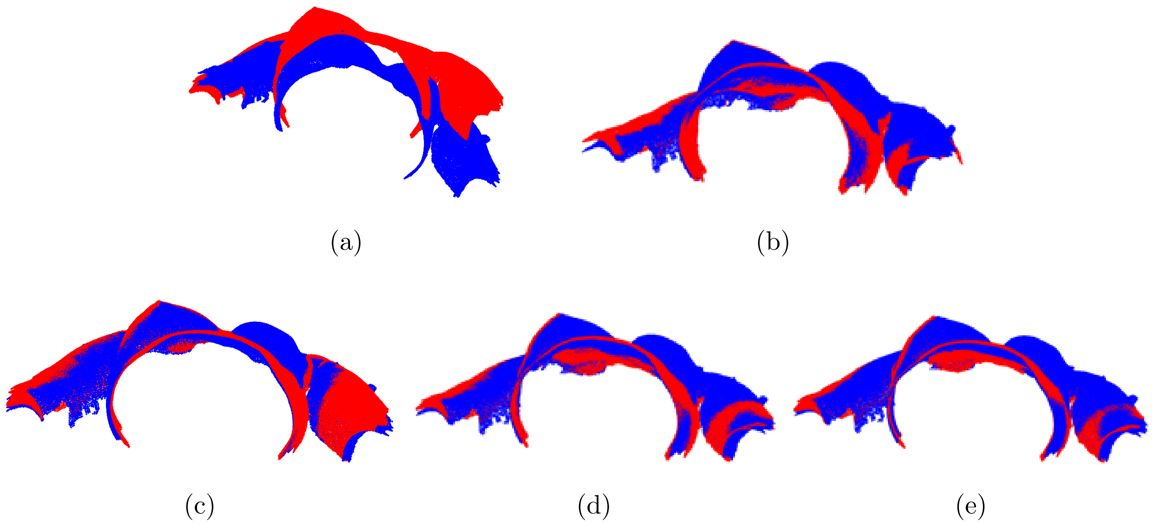

Figure 4.19: Example of registration for multiple-visit images from individual patient (initial visit vs subsequent visit). Reference image (initial visit) is in red, and target image (subsequent visit) is in blue. (a) Original point clouds (bottom-up-view of breasts) showing unmatched images (before registration). (b) 3D correspondence of point cloud achieved following rigid transformation using the proposed algorithm. (c) 3D correspondence of point cloud achieved using the existing ICP algorithm without worst rejection. (d) 3D correspondence of point cloud achieved using the existing ICP algorithm with worst rejection rate 30%. (d) 3D correspondence of point cloud achieved using the existing ICP algorithm with worst rejection rate 60%.

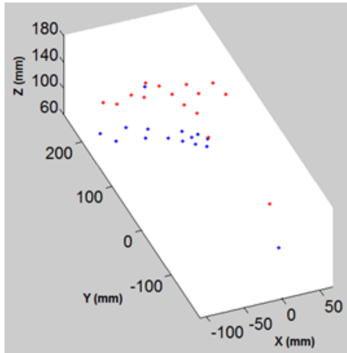


(a)

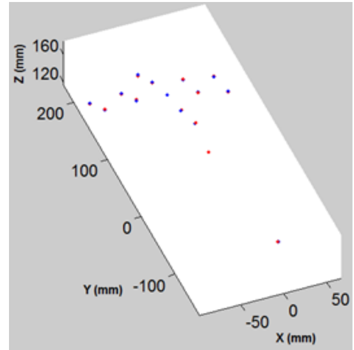


(b)

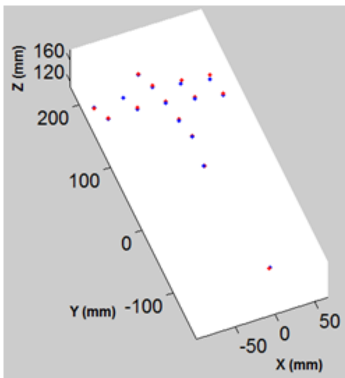


(c)

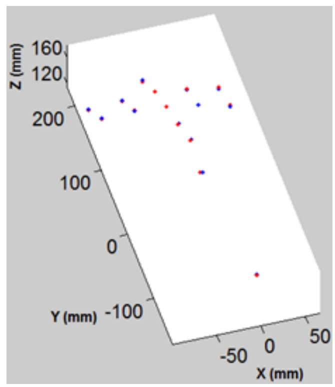


(d)

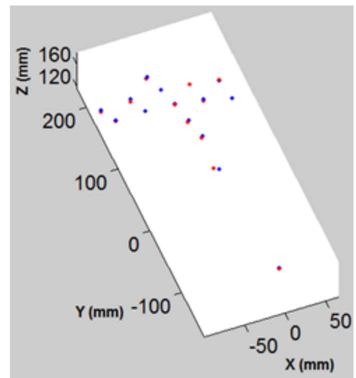


(e)

Figure 4.20: Example of registration for multiple-visit images from individual patient (initial visit vs subsequent visit). The fifteen control points (two manually selected fiducial points SN and UM and thirteen automatically calculated control points) from the reference image (initial visit) are in red color. Their corresponding points from the target image (subsequent visit) are in blue color. (a) The fifteen control points and their corresponding points from unmatched images (before registration). (b) The fifteen control points and their corresponding points from registered images achieved using the proposed algorithm. (c) The fifteen control points and their corresponding points from registered images achieved using the existing ICP algorithm without worst rejection. (d) The fifteen control points and their corresponding points from registered images achieved using the existing ICP algorithm with worst rejection rate 30%. (d) The fifteen control points and their corresponding points from registered images achieved using the existing ICP algorithm with worst rejection rate 60%.

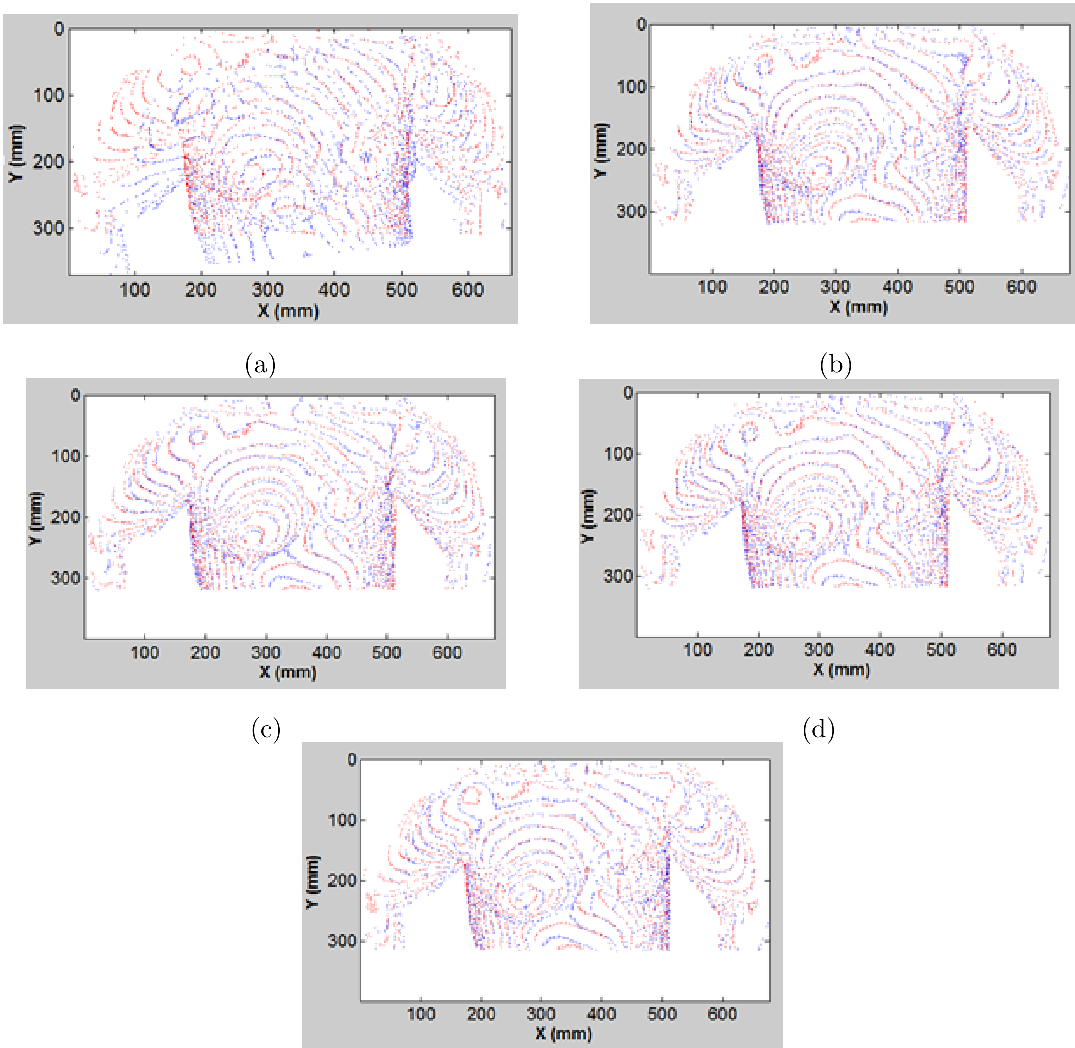


(a) (b) (c) (d) (e)

Figure 4.21: Example of registration for multiple-visit images from individual patient (initial visit vs subsequent visit). Reference image (initial visit) is in red, and target image (subsequent visit) is in blue. (a) 2D point fingerprints showing unregistered images. (b) 2D point fingerprints for registered images achieved using the proposed algorithm. (c) 2D point fingerprints for registered images achieved using the existing ICP algorithm without worst rejection. (d) 2D point fingerprints for registered images achieved using the existing ICP algorithm with worst rejection rate 30%. (d) 2D point fingerprints for registered images achieved using the existing ICP algorithm with worst rejection rate 60%.

Table 4.4 shows the average data of the 83 registrations for the multiple-visit images from the 34 patients. For each pair of the registered images, $E_1$ (RMS distance) and $E_2$ (the angle between surface normals) are computed based on the fifteen control points from the reference image and their corresponding points from the transformed target image. The surface normals are computed from patches around points with radius $10mm$ and $15mm$ respectively.

From Table 4.4, we can see that our proposed algorithm outperforms the existing ICP algorithm with all of the three worst rejection rates 0, 30%, and 60% for multiple-visit images. Comparing to our proposed algorithm, the relative errors of the existing ICP algorithm with worst rejection rate 30% are: 102.62% for average $E_1$, 15.47% and 16.92% for average $E_2$ with radius $10mm$ and $15mm$ respectively. When the rejection rates are 0 and 60%, the ICP even have worse performance: relative errors of average $E_1$ are 212.82% and 226.17%; improvements for average $E_2$ are between 41.24% and 68.28% with both patch radius $10mm$ and $15mm$. The proposed algorithm has the largest mutual information value $M$ 5.3031 which also represents the best performance. The experimental results demonstrate that our proposed algorithm has obvious improvement comparing to the existing ICP algorithm.

we performed a two-way paired $t$-test with a 99% confidence interval to compare the proposed algorithm and the existing ICP algorithm. Table 4.5 shows the $p$-values for all 83 registrations. For each pairwise comparison, $p\text{-value} < 0.01$. We reject the null hypothesis that the two means are equal. The paired $t$-test shows significant difference between the results from the proposed algorithm and existing ICP algorithm with all three rejection rates.

Table 4.4: Registration error comparison for multiple-visit images from individual patient for all 83 registrations

| **Algorithms** | | **Average $E_1$** | **Average $E_2$** | | **Average M** |
|---|---|---|---|---|---|
| | | | $R = 10mm$ | $R = 15mm$ | |
| **Proposed Algorithm** | | (2.3611 ±1.7463) mm | (3.8084 ±2.8119)° | (3.4854 ±2.6351)° | 5.3031 ±0.5385 |
| **Existing ICP Algorithm** | $WR = 0$ | (7.3860 ±4.3093) mm | (5.4381 ±3.4932)° | (4.9225 ±3.2102)° | (5.2873 ±0.5416) |
| | $WR = 30\%$ | (4.7842 ±2.5806) mm | (4.3977 ±3.0099)° | (4.0750 ±2.8287)° | 5.2957 ±0.5437 |
| | $WR = 60\%$ | (7.7012 ±7.2115) mm | (6.1840 ±5.9761)° | (5.8652 ±5.8785)° | (5.1463 ±0.6191) |
| **Relative Error $E_r$** | $WR = 0$ | 212.82% | 42.79% | 41.24% | −0.29% |
| | $WR = 30\%$ | 102.62% | 15.47% | 16.92% | −0.14% |
| | $WR = 60\%$ | 226.17% | 62.38% | 68.28% | −2.95% |

$WR$: worst rejection.

Table 4.5: $p$-values for paired $t$-test between proposed algorithm and existing ICP algorithm for all 83 registrations

| **$p$-values** | $E_1$ | $E_2$ | | **M** |
|---|---|---|---|---|
| | | $R = 10mm$ | $R = 15mm$ | |
| **Proposed Algorithm vs ICP/$WR = 0$** | $2.458X10^{-18}$ | $3.500X10^{-6}$ | $9.832X10^{-6}$ | $2.290X10^{-7}$ |
| **Proposed Algorithm vs ICP/$WR = 30\%$** | $4.023X10^{-24}$ | $6.683X10^{-18}$ | $1.408X10^{-14}$ | $4.752X10^{-7}$ |
| **Proposed Algorithm vs ICP/$WR = 60\%$** | $1.321X10^{-10}$ | $1.355X10^{-3}$ | $8.65X10^{-4}$ | $2.017X10^{-5}$ |

$WR$: worst rejection.

### 4.6.3 Robustness for BMI Variation

The effect of patient BMI on registration performance is investigated using data from 34 patients. For each pair of multiple-visit images of the same patient, the average BMI for the two images is used to classify the pair of images into four categories: underweight ($< 18.5$), normal ($18.5 \sim 24.9$), overweight ($25 \sim 29.9$), and obese ($\geq 30$). In the 83 registrations, 27 are normal, 25 are overweight, and 31 are obese. Average registration errors of the tests for each BMI category are listed in Table 4.6. The proposed algorithm is compared with the existing ICP algorithm with 30% rejection, which has the best performance in the three worst rejection rates.

In the Table 4.6, $E_1$ and $E_2$ for both the proposed algorithm and the existing ICP algorithm have the similar variation trend that rise with the increase in BMI. However, in each BMI category, our proposed algorithm can outperform the existing ICP algorithm based on average $E_1$ and $E_2$ . When BMI $\geq 30$ (obese), the proposed algorithm has the largest registration errors: average$E_1$ is $(2.7232 \pm 1.9759)mm$, average $E_2$ with radius $10mm$ and $15mm$ are $(4.2258 \pm 3.9269)$ degree and $(3.9947 \pm 3.6867)$ degree, which are extremely small. The mutual information $M$ is not comparable between BMI categories since the images in different BMI category have different densities of point cloud and patient postures. However, the value of the mutual information in the same BMI category for different algorithm represents the accuracy of the registration. The average mutual information values achieved from the proposed algorithm are larger than those obtained from existing ICP algorithm in all BMI categories.

we performed a two-way paired $t$-test with a 99% confidence interval to compare the proposed algorithm and the existing ICP algorithm with worst rejection rate 30%

for all BMI categories. Table 4.7 shows that the $p$-value $< 0.01$ for each pairwise comparison, . We reject the null hypothesis that the two means are equal. The paired $t$-test shows significant difference between the results from the proposed algorithm and existing ICP algorithm with worst rejection rate 30% for all BMI categories.

Table 4.6: Average registration errors for each BMI group for 83 registrations

| **BMI Categories** | **Algorithms** | **Average $E_1$** | **Average $E_2$** | | **Average M** |
|---|---|---|---|---|---|
| | | | $R = 10mm$ | $R = 15mm$ | |
| **Normal** ($18.5 \sim 24.9$) | Proposed Algorithm | (1.8332 ±0.8983)mm | (3.5798 ±1.7129)° | (3.2372 ±1.5170)° | 5.2995 ±0.5592 |
| | Existing ICP Algorithm ($WR = 30\%$) | (4.2769 ±2.0016)mm | (4.1775 ±1.8587)° | (3.7759 ±1.7684)° | 5.2934 ±0.5653 |
| **Overweight** ($25 \sim 29.9$) | Proposed Algorithm | (2.4823 ±2.0414)mm | (3.5376 ±2.0494)° | (3.1218 ±1.9233)° | 5.3562 ±0.4223 |
| | Existing ICP Algorithm ($WR = 30\%$) | (4.7227 ±2.8849)mm | (4.3300 ±2.5018)° | (3.8559 ±2.5073)° | 5.3488 ±0.4264 |
| **Obese** ($\geq 30$) | Proposed Algorithm | (2.7232 ±1.9759)mm | (4.2258 ±3.9269)° | (3.9947 ±3.6867)° | 5.2635 ±0.6123 |
| | Existing ICP Algorithm ($WR = 30\%$) | (5.2756 ±2.7546)mm | (4.6440 ±4.0807)° | (4.5121 ±3.7166)° | 5.2549 ±0.6176 |

$WR$: worst rejection

Table 4.7: $p$-values for paired $t$-test between proposed algorithm and existing ICP algorithm ($WR = 30\%$) for each BMI group

| **BMI Categories** | $E_1$ | $E_2$ | | **M** |
|---|---|---|---|---|
| | | $R = 10mm$ | $R = 15mm$ | |
| **Normal** ($18.5 \sim 24.9$) | $1.359X10^{-8}$ | $1.577X10^{-9}$ | $5.188X10^{-7}$ | $7.052X10^{-4}$ |
| **Overweight** ($25 \sim 29.9$) | $3.972X10^{-6}$ | $5.028X10^{-8}$ | $4.045X10^{-6}$ | $3.386X10^{-4}$ |
| **Obese** ($\geq 30$) | $7.065X10^{-13}$ | $1.063X10^{-4}$ | $1.014X10^{-4}$ | $9.020X10^{-3}$ |

$WR$: worst rejection

## 4.7 Conclusions

A rigid registration algorithm of 3D images from multiple clinical visits for the same patient has been developed and demonstrated using mannequin images and multiple-visit images from the same patient acquired at two different clinical visits.

Registration is achieved by maximizing the correspondence between the fifteen pair of control points from the two images. In the fifteen control points from each image, two fiducial points SN and UM are manually identified, and other thirteen control points are automatically calculated from the surface of the 3D image based on the coordinates of SN and UM. To overcome operator bias caused by manual fiducial points selection, we optimize the selection of SN and UM, and thereby the locations of all other thirteen control points in the target image. The mannequin images are used to simulate the location changes between SNs and UMs manually selected from two images to evaluate the convergence of our optimization method.

The simulation results show that our proposed algorithm can obtain convergence of SN and UM optimization for mannequin images.

The registration accuracy of our proposed algorithm is demonstrated by comparing to an existing ICP algorithm. For the mannequin images, our proposed algorithm outperforms the existing ICP algorithm with all of the three worst rejection rates: 0, 30%, and 60%. The improvement of 1592.86% for average $E_1$ (RMS distance) comparing to the existing ICP algorithm without worst rejection shows that our proposed algorithm is robust for the noise in the 3D images. The average $E_1$ $(0.2162 \pm 0.0588)mm$ for all registrations and the improvement between 8.91% and 18.91% for $E_2$ (angle between the surface normals of the two registered images) comparing to the existing ICP algorithm with worst rejection rates 30% and 60% show that the proposed algorithm has good performance for registration of images with exact rigid transformation. For multiple-visit images acquired from patients, our proposed algorithm has significant improvement comparing to the existing ICP algorithm. For the $E_1$ of 83 registrations, our proposed algorithm has improvement of 212.82%, 102.62% and 226.17% comparing to the ICP algorithm with three different worst rejection rates respectively. And also, the proposed algorithm has much better $E_2$ and largest mutual information value. Thus, the proposed algorithm can obviously outperform the existing ICP algorithm and do not need to consider the worst rejection rate, with strong evidence by $t$-test.

Patient's BMI may vary over time. The effect of patient BMI on registration performance is investigated using multiple-visit images from the patients. For our proposed algorithm, the largest registration error occurs when the BMI $\geq 30$ (obese). The average $E_1$ is $(2.7232 \pm 1.9759)$mm for this BMI category, which is extremely small. And also, in each BMI category, our proposed algorithm can outperform the existing ICP algorithm based on $E_1$, $E_2$, and mutual information $M$. Thus, our proposed algorithm is robust to the BMI variation, with strong evidence by $t$-test.

# Chapter 5

# Detection of the Lowest Breast Contour in 3D Images of the Female Torso

## 5.1 Introduction

### 5.1.1 Definition of the Lowest Breast Contour

The Lowest breast contour is the contour where the breast is touching the abdominal wall (Fig.5.1). Fig. 5.1 (a) shows the breast of ptosis degree 0, in which the lowest breast contour is visible in upright position. Fig. 5.1 (b) shows the breast of ptosis degree 1, in which the lowest breast contour is slightly visible in upright position. Fig. 5.1 (c) and (d) show the breast of ptosis degree 2 and 3, in which the lowest breast contours are not visible and up under the breasts in upright position, but are visible if the images are rotated so that the viewer is looking from below at the breasts.

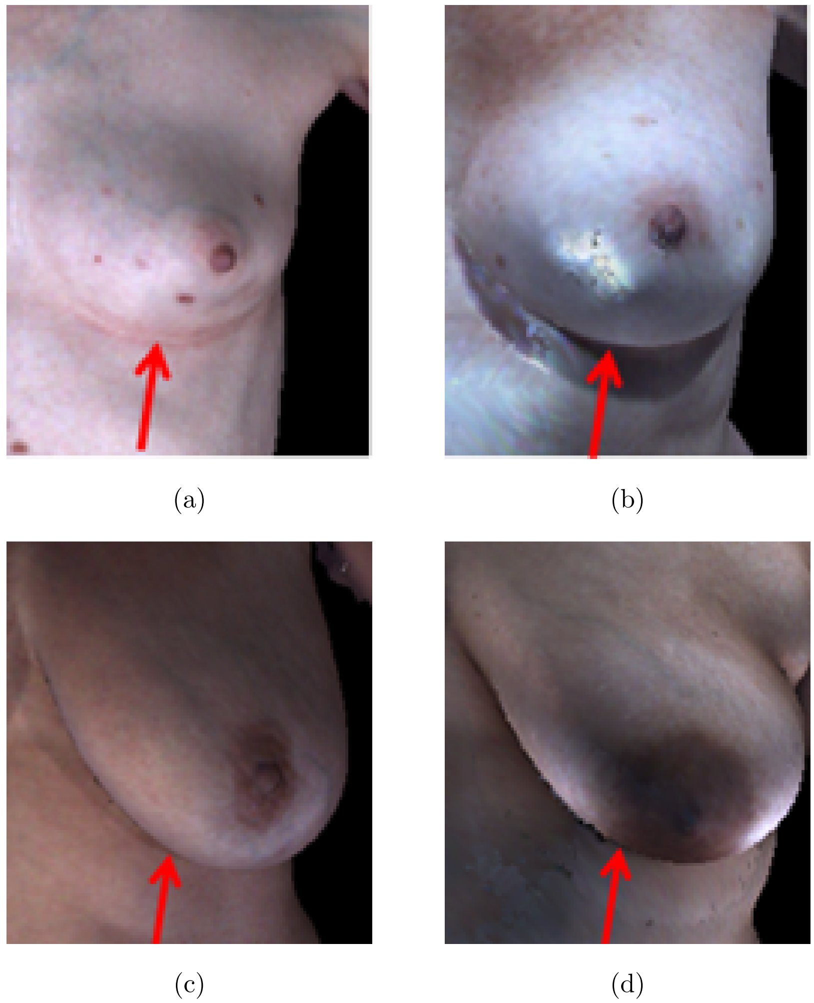


Figure 5.1: The lowest breast contours are indicated with red arrows for breasts with varying degrees of ptosis: (a) Ptosis grade 0. (b) Ptosis grade 1. (c) Ptosis grade 2. (d) Ptosis grade 3.

The lowest breast contour is an important attribute for quantitative assessment of breast aesthetics. The detected lowest breast contour enables computation of morphological measures such as volume [7, 18–20], and facilitates the identification of other characteristics of the breast morphology such as ptosis [8] and nipple [78]. This information is critical for pre-operative planning and post-operative assessment of outcomes in breast reconstruction.

### 5.1.2 Related Works

Previous studies on breast contour detection have been performed on 2D images and 2D range images encoding depth (depth-map images). Cardoso et al. [79, 80] described an automatic method for the detection of lower half of the breast contour in 2D images. The position of the external endpoint of the lower half of the breast contour was defined at the armpit of the body. The internal endpoint was estimated simply as the mid-point between the two external endpoints. After modeling the image as a weighted graph based on the gradient values in $z$ direction and prior shape information, the lower half of the breast contour was computed as the solution to the shortest-path problem between the internal and external endpoints. In subsequent studies [81, 82], this approach was extended to perform tracing of the lower half of the breast contour in depth-map images. Both 2D images and depth-map images cannot capture the overlapped regions, e.g. the underside regions of the breasts with high ptosis degree. They detected a 2D outline of the lower half of the breast, rather than the 3D breast contour in the 3D surface image. Lee et al. [83, 84] introduced a measure of the lower half of the breast contour in 2D images which enforced a mathematical shape constraint based on the catenary curve, a perfectly flexible and inextensible string of uniform density supported by two distinct points. First, they used a catenary curve to approximate the overall contour of the lower half of the breast, and extracted a shape parameter, which is a measure of the lower half of the breast contour representing the outlining catenary curve. The catenary-based shape measure was used by Lee et al. to evaluate the contours of the upper and lower breast in 3D images of patients [85]. The outlines of the upper and lower breast were first obtained from coronal sectional views that were created from multiple parallel planes to the chest wall, spaced at about 1cm intervals starting at the anterior most part of the breast. Then the breast contour was extracted by fitting catenary curves to the resulting outline in each sectional view. Although this method used 3D images as input, the obtained breast contours are curves in 2D planes, and do not directly mirror the 3D breast contours.

Due to the lack of the algorithms to directly compute the breast contour on the 3D surface mesh. In this chapter, we describe a curvature-based lowest breast contour detection algorithm in 3D images of the female torso [86], which employs the shape index [87] and minimum principle curvature.

## 5.2 Algorithm

### 5.2.1 Overview

Before we detect the lowest breast contour, we manually crop the 3D image acquired from the female torso and just keep the region below the neck and above the umbilicous. The regions which are automatically unlikely to contain breasts are removed (Fig. 5.3a).

The overview of our algorithm for the detection of the lowest breast contour in 3D images is illustrated in Fig. 5.2. First, we calculate the two principle curvatures for all points in the surface mesh of the 3D image. And then, we compute the shape index [87] from the two principle curvatures. After that, the possible contour points ($sPP$) are detected as the points with negative shape indices (i.e. exhibiting concave shape) and their minimum principle curvatures less than the mean of that for all points on the torso. The possible contour points include not only the points lying along the lowest breast contour, but also points in the randomly scattered regions (noise) on the torso that represent isolated incidences of low shape index and curvature values due to mesh undulation. A reference point $RP$, a point located at the breast mound area and roughly above the nipple position (the nipple is not necessary for determination of the $RP$), is determined for each breast to facilitate separating the lowest breast contour points from the other points on the torso that also display low curvature values. Then the cubic-spline curve fitting is applied to the detected points and the curve is identified as the lowest breast contour.

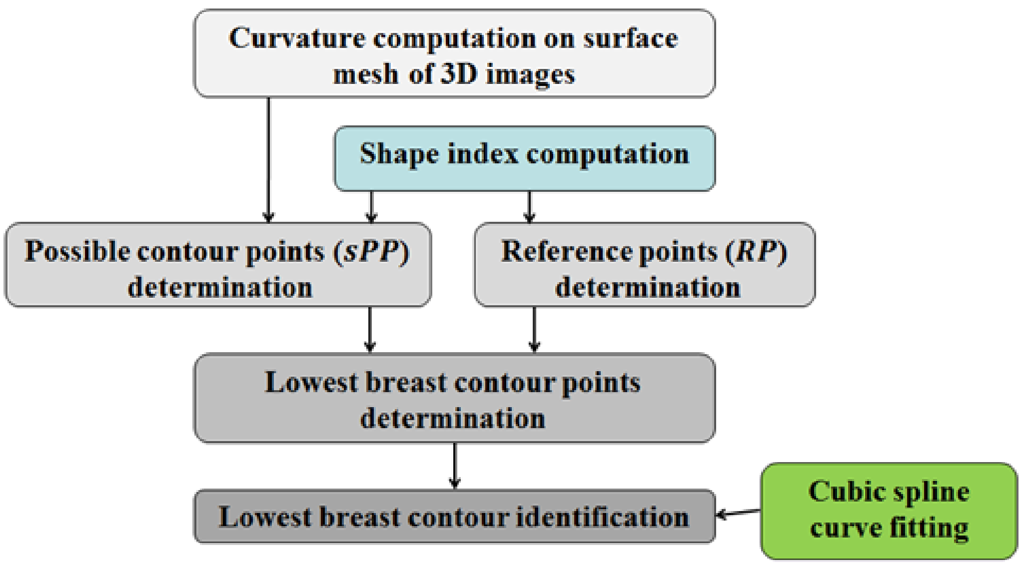


Figure 5.2: Overview of the detection algorithm for the lowest breast contour in 3D images of the female torso

### 5.2.2 Curvature Analysis

Curvature is defined as the amount that a surface deviates from being flat. At each point $p$ of a 3D surface one may find a normal plane, which contains the normal vector of the point $p$. The intersection of the normal plane and the 3D surface is a plane curve. The plane curves from different normal planes at point $p$ will generate different curvatures. The principal curvatures, $k_{max}$ and $k_{min}$, are the maximum and minimum values of the curvatures at $p$.

To calculate the principal curvatures on 3D surface mesh, we used a toolbox developed by Gabriel Peyre [88] based on the algorithms proposed by Cohen-Steiner et al. [89,90]. The curvature tensor for each vertex was estimated using the following expression [90]:

$$T(\upsilon) = \frac{1}{|B|} \sum_{edges\ e} \beta(e)|e \cap B|\bar{e}\bar{e}^t \tag{5.1}$$

where $\upsilon$ is an arbitrary vertex on the 3D mesh, $|B|$ is the surface area around $\upsilon$ over which the curvature tensor is estimated, $\beta(e)$ is the signed angle between the normals to the two oriented triangles incident to edge $e$ (positive if convex, negative if concave), $|e \cap B|$ is the length of $e \cap B$ (always between 0 and $|e|$), and $\bar{e}$ is a unit vector in the same direction as $e$. The tensor is evaluated at every vertex location $\upsilon$, for a neighborhood $B$ that approximates a geodesic disk around this vertex. In this study, we employed a 10-ring neighborhood for $B$, which is the author suggested size. The two principal eigen values, $k_{max}$ and $k_{min}$ calculated for this tensor vector, are the estimates of principal curvatures at $\upsilon$.

### 5.2.3 Shape Index

Shape index $S$ for each point on the surface mesh is given by equation 5.2 [87]. Table 5.1 defines the classification of different shaped regions of a surface based on the shape index.

$$S = \frac{2}{\pi} \tan^{-1}\left(\frac{k_{max} + k_{min}}{k_{max} - k_{min}}\right) \tag{5.2}$$

Table 5.1: Classification based on shape index $S$

| **Shape** | **Index Range** |
|---|---|
| Concave Ellipsoid | $S \in [-1, -5/8)$ |
| Concave Cylinder | $S \in [-5/8, -3/8)$ |
| Hyperboloid | $S \in [-3/8, 3/8)$ |
| Convex Cylinder | $S \in [3/8, 5/8)$ |
| Convex Ellipsoid | $S \in [5/8, 1]$ |

We employ a pseudo-color visualization method for viewing the shape index of the 3D mesh. Fig. 5.3a presents a representative 3D image of the torso, and the color-mapped shape index for the torso is presented in Fig. 5.3b. The region of the lower breast mound exhibits red color ($S > 0$, convex shape) and the region of the lowest breast contour exhibits blue color ($S < 0$, concave shape).

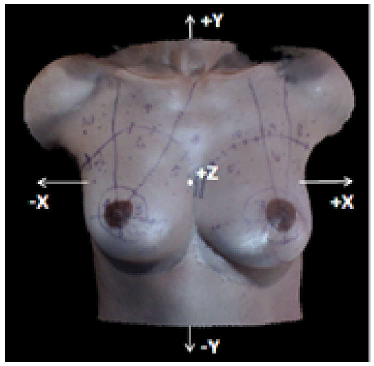


(a)

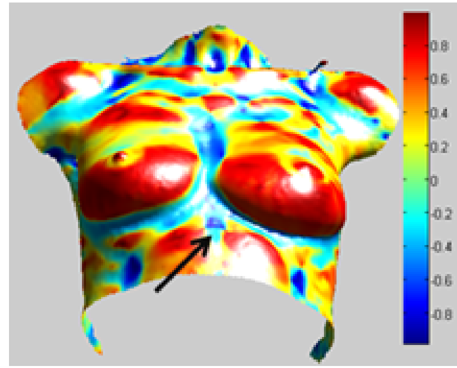


(b)

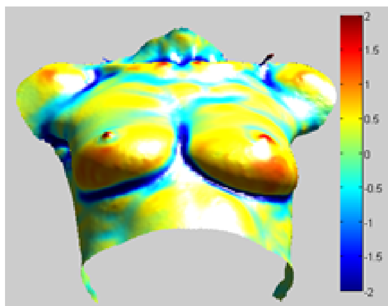


(c)

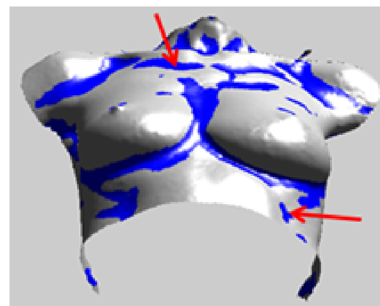

(d)

Figure 5.3: (a) Representative 3D image of the female torso (X, Y, and Z axes are displayed in the figure). (b) Color-mapped shape index of 3D surface mesh. Black arrow illustrates the region eliminated from $sPP$ by $k_{min} < k_{mean}$. Colorbar shows the correspondence between colors and shape index values. (c) Color-mapped minimum principle curvature $k_{min}$ of 3D surface mesh. The principle curvatures are shifted so that the $k_{mean}$ to be 0, i.e., the values above $k_{mean}$ are shown to be positive and the values below $k_{mean}$ are shown to be negative. Colorbar shows the correspondence between colors and shifted minimum principle curvature values. (d) Regions of possible contour points $sPP$ (blue) in the surface scan. Red arrows illustrate points on the torso that exhibit low curvature and thus are in the $sPP$ set, but do not lie along the lowest breast contour.

### 5.2.4 Possible Contour Points

Before we detect the points along the lowest breast contour, we first obtain a set of possible contour points $sPP$ using a preprocessing step, which employs the shape indices and minimum principle curvatures of the 3D mesh. We define a possible contour point as a point which has the negative shape index $S$ and the minimum principle curvature $k_{min}$ less than the mean of the minimum principal curvatures $k_{mean}$ for all points on the torso, i.e.,

$$k_{mean} = \frac{\sum_{i=1}^{num} (k_{min})_i}{num} \tag{5.3}$$

where $num$ is the total number of points in the 3D mesh of the torso, and for a point $p$,

$$\begin{cases} p \in sPP & if\ S < 0\ and\ k_{min} < k_{mean} \\ p \notin sPP & otherwise \end{cases} \tag{5.4}$$

For points in some regions which are relatively flat and highly unlikely to be points lying along breast contour, their $k_{max}$ and $k_{min}$ are near zero. However, in these regions, $k_{max} + k_{min} < 0$ may be met, thereby $S < 0$. We use another condition $k_{min} < k_{mean}$ to eliminate these points from $sPP$. In Fig. 5.3b, the region, which black arrow points to, meets $s < 0$, but not meets $k_{min} < k_{mean}$. Thus the combination of $s < 0$ and $k_{min} < k_{mean}$ filters the set $sPP$ such that it has fewer points that have low curvatures and are not long the lowest breast contour.

Fig. 5.3c shows the color-mapped minimum principle curvature $k_{min}$ of the 3D surface mesh. In the figure, we shift the minimum principle curvatures so that $k_{mean}$ to be 0, i.e., the values above $k_{mean}$ are shown to be positive and the values below $k_{mean}$ are shown to be negative. The possible contour points ($sPP$) are displayed in

Fig. 5.3d.

### 5.2.5 Determination of the Reference Points for Each Breast Mounds

After we obtain the possible contour points set $sPP$, we automatically locate an estimate for the reference point $RP$ (see Fig. 5.4b) for each breast using the shape index. $RP$ is located at the breast mound area and roughly above the nipple position (the nipple is not necessary for determination of the $RP$). It is used as a reference point to calculate angles for points in set $sPP$.

The $RP$ determination method is applicable to both breasts but for simplicity, is discussed here in terms of the right breast. We use the weighted shape index for each point to determine the $RP$, where weight is the $z$ coordinate of the point. To smooth the weighted shape index in case some points exhibit isolated shape change in shape index, we divided the points on right half torso into blocks based on their $x$ and $y$ coordinates ($x$, $y$, and $z$ directions are displayed in Fig. 5.3a) and compute the average of weighted shape index $ave\_S_i$ in each block. The block size we used is $5mm\ X\ 5mm$. The point cloud is dense in breast mound region in 3D images, the distances between adjacent points in this region are usually no more than $2mm$. A $5mmX5mm$ block include about 9 points, it is enough to smooth the weighted shape index for points. For each block $i$, the average of weighted shape index $ave\_S_i$ is computed using equation 5.5:

$$ave\_S_i = \frac{\sum_{j=1}^{n_i} S_{ij} z_{ij}}{n_i} \tag{5.5}$$

where $n_i$ is the number of points in block $i$, $S_{ij}$ and $z_{ij}$ are shape index and $z$ coordinate of point $j$ in block $i$ respectively. $z_{ij}$ is a shifted value so that all points on the right half torso have non-negative $z$ coordinate values:

$$z_{ij} = zo_{ij} - z_{min} \tag{5.6}$$

where $zo_{ij}$ is the original $z$ coordinate value of point $j$ in the block $i$, and $z_{min}$ is the minimum original $z$ coordinate value for all points on the right half torso. Fig. 5.4a shows the color mapped $ave\_S$ for each $5mm\,X\,5mm$ block of the torso. In the right half torso, let the block with the largest $ave\_S$ to be block $A$ (marked as black spot in Fig. 5.4a). Then we search a range $7X10$ blocks ($35mmX50mm$, i.e., $15mm$ from block $A$ in left and right directions) above this block and let the highest block (in $y$ direction) with $ave\_S > 0$ in this range to be block $B$. The coordinates of the $RP$ can be estimated as follows (only $x$ and $y$ coordinates of $RP$ are required for angle calculation for possible contour points in set $sPP$):

$$\begin{cases} x_{RP} = x_{AC} \\ y_{RP} = y_{BC} \end{cases} \tag{5.7}$$

Where $x_{RP}$ and $y_{RP}$ are $x$ and $y$ coordinates of $RP$ respectively, $x_{AC}$ is the $x$ coordinate of the center of block $A$, and $y_{RP}$ is the $y$ coordinate of the center of block $B$. The $15mm$ from block $A$ in left and right directions is used to bound the $RP$ not far from block $A$ in $x$ direction. $50mm$ above $A$ is used to avoid $RP$ location lower than the lowest breast contour in images of ptotic breasts. The automatically estimated $RP$ locations for two breasts are showed in Fig. 5.4b.

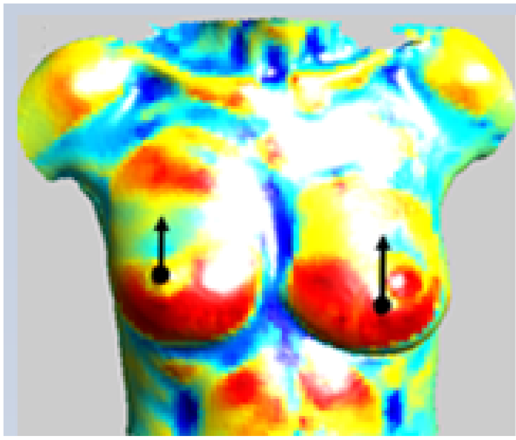

(a)

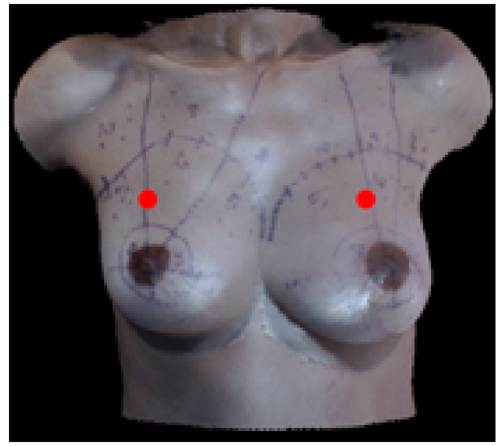

(b)

Figure 5.4: (a) Color-mapped $ave\_S$ in $5mmX5mm$ blocks. The black arrow means to search a range ($7X10$ blocks) above the block with the largest $ave\_S$ in the half torso. (b) Estimates of reference points $RPs$ (red) for the left and right breasts.

### 5.2.6 Determination of the Lowest Breast Contour

#### 5.2.6.1 Angle Calculation

For each point $p_i$ in the possible contour points set $sPP$ from the right half of the torso, we calculate the angle $\theta_i$ which is relative to $RP$ and defined by equation 5.8:

$$\theta_i = sign(x_{p_i} - x_{RP}) \cos^{-1} \left( \frac{\overrightarrow{v_1} \cdot \overrightarrow{v_2}}{|\overrightarrow{v_1} \cdot \overrightarrow{v_2}|} \right) \tag{5.8}$$

where $\overrightarrow{v_1}$ is a vector along $-y$ direction, $\overrightarrow{v_2} = (x_{p_i} - x_{RP}, y_{p_i} - y_{RP})$ in which $x_{p_i}$ and $y_{p_i}$ are $x$ and $y$ coordinates of point $p_i$ in $sPP$ and $x_{RP}$ and $y_{RP}$ are coordinates of $RP$. All points in set $sPP$ are sorted based on their angles to facilitate subsequent computations.

#### 5.2.6.2 Intermediate Point Determination

We divide points in $sPP$ into different sectors based on their angles and detect one lowest breast contour point in each sector. The normal breast base width is no more than $20cm$ [53]. The block with largest $ave\_S$ is generally located the lower part of the breast mound. The $RP$ is no more than $50mm$ higher than the block with largest $ave\_S$. So in the projection in XY plane, the distances from $RP$ to the lowest breast contour points are no more than $15cm$. We divide points in $sPP$ into different sectors at angle interval $5°$, then the average distance between two adjacent detected lowest breast contour points is no more than $13mm$. It is dense enough to fit a contour curve using cubic spline. If more accurate result is desired, a smaller angle interval can be selected.

From the sector below $RP$, i.e. $-2.5° \sim 2.5°$ in $sPP$ (Fig. 5.6a), we estimate an intermediate point of the lowest breast contour which is used to locate the contour position correctly. Points in this sector have x coordinates close to that of $RP$. The intermediate point is determined using following three steps: (1) calculate normals for all points in sector $-2.5° \sim 2.5°$ in $sPP$; (2) find the possible contour point $M$ displaying the largest shape change. (3) estimate the intermediate point from $M$.

For each point in the sector $-2.5° \sim 2.5°$ in $sPP$, the normal is calculated as the sum of the normalized normals of its one-ring triangles. One-ring triangles of a vertex $p$ in the triangular surface mesh are defined as all triangles which share vertex $p$ (Fig. 5.5). Let $A$, $B$, and $C$ be the three vertices of a triangle, then the normalized surface normal $\overrightarrow{n}$ of the triangle can be obtained by equation 5.9:

$$\overrightarrow{n} = \frac{\overrightarrow{AB} X \overrightarrow{AC}}{|\overrightarrow{AB} X \overrightarrow{AC}|} \tag{5.9}$$

where "$X$" means cross product of vectors,"$|\ |$" is the 2-norm, i.e., the length of the vector. The normal $\overrightarrow{N_p}$ of $p$ is computed as:

$$\overrightarrow{N_p} = \sum_{j=1}^{m} \overrightarrow{n_j} \tag{5.10}$$

where $m$ is the total number of one-ring triangles of $p$, and $\overrightarrow{n_j}$ is the normalized normal of $jth$ one-ring triangle of $p$.

The possible contour points in set $sPP$ include not only the points in the region containing the lowest breast contour, but also points in the randomly scattered regions (noise) on the torso that represent isolated incidences of low shape index and curvature values due to mesh undulation (Fig 5.3d). However, below RP, only the lowest breast contour area exhibits sharp change of the shape (Fig. 5.4b). In the sector $-2.5° \sim 2.5°$, we find a possible contour point $M$ displaying the largest shape change in a range with radius $10mm$ around the point to locate the region containing the lowest breast contour. We have tried $5mm$, $10mm$, $15mm$ and $20mm$ for radius size. Since the point cloud is sparse in lowest breast contour region for some 3D images, the distance between some adjacent points may be larger than $5mm$. Radius size with $5mm$ cannot find accurate result for some breasts. In $20mm$ case, the detected intermediate point may locate out of the lowest breast contour region since this size is too large. $10mm$ and $15mm$ can obtain accurate intermediate point estimation and results have no difference between them, we select $10mm$ as the radius size.

The point $M$ is estimated by angles between normals of points, i.e. the larger the angle between normals of two points, the larger the shape change between them. The angle between two normals can be calculated as:

$$A_{12} = \cos^{-1} \frac{\overrightarrow{n_1}\overrightarrow{n_2}}{|\overrightarrow{n_1}||\overrightarrow{n_2}|} \tag{5.11}$$

where $\overrightarrow{n_1}$ and $\overrightarrow{n_2}$ are the normals of the two points. For each point $p$ in the sector $-2.5° \sim 2.5°$ in $sPP$, we calculate the angles of normals between point $p$ and all other possible contour points within a range of $10mm$ in Euclidean distance to $p$, and let the maximum angle be the normal angle ($NOA$) of $p$. $M$ is selected as the possible contour point which have the maximum $NOA$ in the sector $-2.5° \sim 2.5°$.

The intermediate point (Fig. 5.6b) is selected based on that the lowest breast contour is an inward curving crease below the breast and the points on the contour exhibit low minimum principle curvatures. We determine the intermediate point as the point in $sPP$ which is in a range of $10mm$ in Euclidean distance to point M and has the minimum $k_{min}$ value.

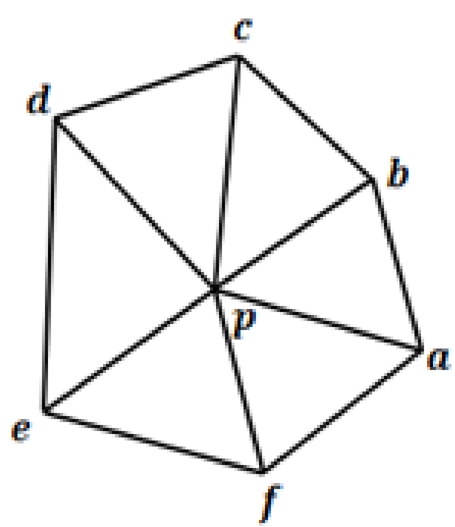


Figure 5.5: One-ring triangles of a vertex p

#### 5.2.6.3 Curvature Extension

From the estimated intermediate point of the lowest breast contour, we extend the contour points along two directions. $sPP$ points are divided into different 5° sector regions centered at $RP$ (Fig. 5.6a). In each sector, we detect the contour point, such that it has a minimum $k_{min}$ value in all $sPP$ points in this sector, and its Euclidean distance to the previously detected contour point in the previous interval $< 2L$, where $L$ is the arc length of current interval and can be calculated using equation 5.12. The distance $2L$ is the largest possible distance between the lowest breast contour in the adjacent sectors. It is used to avoid selecting noise points as the contour points which deflect from the lowest breast contour region.

$$L = \frac{5^\circ \pi}{180^\circ} R \tag{5.12}$$

where $R$ is the radius from $RP$ to the contour arc of the current interval, which is approximated as the Euclidean distance from $RP$ to the detected contour point in the previous interval since current interval has not yet undergone processing to separate the lowest breast contour point from noise. If there is no $sPP$ point in an interval at distance $< 2L$, the detection is terminated in that direction. The detected lowest breast contour points are displayed in Fig. 5.6b as green color. The resulting fitted cubic-spline curve generated from the detected contour points is identified as the lowest breast contour.

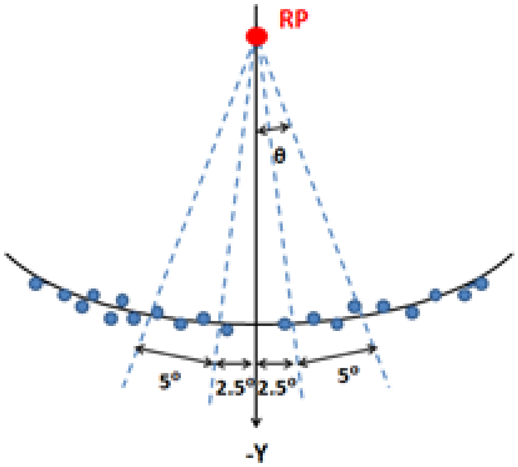


(a)

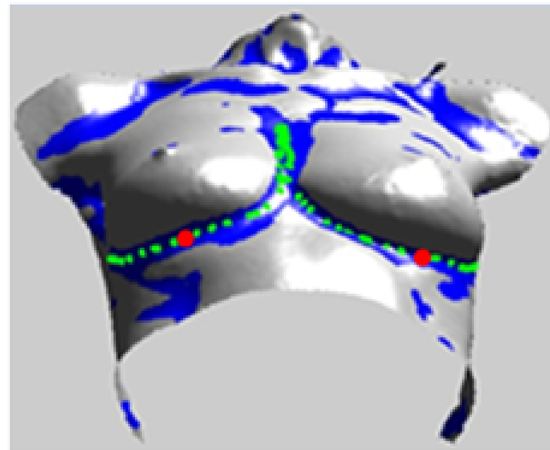

(b)

Figure 5.6: (a) $sPP$ points (blue) are divided into different 5° sector regions based on their angles $\theta$ relative to $RP$ (red). (b) Set of possible contour points $sPP$ (blue) and detected points along the lowest breast contours (green) displayed on surface. Red points are determined intermediate points.

## 5.3 Evaluation Metric

We demonstrate our proposed lowest breast contour detection algorithm for 3D images by comparing the automatically detected contours with manually selected contours. The manually selected contours are used as ground truth. Average distance and dice coefficient [91] between these two contours from the same breast are computed for comparison.

### 5.3.1 Average Distance

The average distance between two contours is the average of the distances from all points in two contours to the other one as follows. The automatically detected contour and manually selected contour from the same breast are not same in length. To evaluate the accuracy of our proposed algorithm, we keep the same length for comparison. For the end points of two contours, we calculate their angles relative to $RP$. The contours are cut at each end based on the shorter one, i.e. the one which has the smaller absolute angle value at this end.

We interpolate the same number of points from the automatically detected contour points and manually selected contour points with the same length using cubic spline method to obtain the interpolated point sets $A$ and $B$, respectively. In this research, 200 points are interpolated in each contour to provide enough points for accurate result evaluation. The distance $d(A_i)$ from a point $A_i$ in set $A$ to the other contour, i.e. set $B$ can be represented as:

$$d(A_i) = \min_{B_j \in B} \|A_i - B_j\| \tag{5.13}$$

where $\|\cdot\|$ is the Euclidean distance. And similarly, the distance $d(B_i)$ from a point $B_i$ in set $B$ to set $A$ can be represented as:

$$d(B_j) = \min_{A_i \in A} \|B_j - A_i\| \tag{5.14}$$

Then, the average distance $ave\_d$ between the automatically detected contour and the manually selected contour is calculated by equation 5.15:

$$ave\_d = \frac{\sum_{i=1}^{|A|} d(A_i) + \sum_{j=1}^{|B|} d(B_j)}{|A| + |B|} \tag{5.15}$$

where $|A|$ and $|B|$ are sizes of the set $A$ and $B$ respectively.

### 5.3.2 Dice Coefficient

Dice coefficient is a similarity measure that can be used to evaluate the results of our proposed algorithm for detecting the 3D lowest breast contour. We compute the dice coefficient between the automatically detected breast contour and the manually selected contour as follows. For each point in $A$ (or $B$), we compute the distance to the other contour point set $B$ (or $A$). Let num be the total number of the points in $A$ and $B$ with distances less than a given threshold, the dice coefficient $Dc$ is computed as $num$ over the sum of the total number of points in $A$ and $B$:

$$Dc = \frac{num}{|A| + |B|} \tag{5.16}$$

The dice coefficient is always in $[0, 1]$ range. A dice coefficient of 1 indicates high similarity (all points in $A$ and $B$ fall in the distance threshold), whereas 0 indicates little to no similarity (all points in $A$ and $B$ fall out the distance threshold).

## 5.4 Datasets

3D surface images from 77 participants were used in this study. There are 154 breasts in total. The lowest contours for 151 breasts of them were detected and evaluated. For the other 3 breasts, the lowest contours are missed due to holes or data missing on these areas in the 3D images. Since the two breasts for the same patient may have different ptosis grades, we categorize the 151 breasts into 5 groups based on breasts morphology, and not patients. Ethnicity, race, age, BMI, breast ptosis grade, and previous breast surgery information for the participants with breast ptosis grade 0, 1, 2, and 3 are listed in Table 5.2- 5.5 respectively. Table 5.6 contains the demographics for participants with breasts which cannot be rated ($CR$) due to the incomplete surgeries and no nipple reconstruction for these breasts. The stage of the incomplete surgery for each breast is listed in the Table 5.6.

Table 5.2: Demographics and characteristics for participants with breast ptosis grade 0

| **No.** | **Patient ID** | **Visit** | **Race /Ethnicity** | **Age** | **BMI** | **Breast (Right/Left)** | **Ptosis Grade** | **Surgery Type** |
|---|---|---|---|---|---|---|---|---|
| 1 | 7 | V1 | White/NH | 54 | 21.5 | Right | 0 | None |
| 2 | 7 | V1 | White/NH | 54 | 21.5 | Left | 0 | None |
| 3 | 48 | V2 | White/NH | 49 | 24.6 | Right | 0 | Implant/NR |
| 4 | 67 | V1 | White/H | 50 | 23.4 | Right | 0 | Mastopexy & Implant |
| 5 | 67 | V2 | White/H | 50 | 25.6 | Right | 0 | Mastopexy & Implant |
| 6 | 67 | V3 | White/H | 50 | 26.4 | Right | 0 | Mastopexy & Implant |
| 7 | 68 | V1 | White/NH | 54 | 22.4 | Right | 0 | None |
| 8 | 68 | V1 | White/NH | 54 | 22.4 | Left | 0 | None |
| 9 | 68 | V4 | White/NH | 54 | 22.8 | Right | 0 | Implant/NR |
| 10 | 68 | V4 | White/NH | 54 | 22.8 | Left | 0 | Implant/NR |
| 11 | 70 | V2 | White/NH | 52 | 35.4 | Right | 0 | Mastopexy & Implant |
| 12 | 70 | V4 | White/NH | 52 | 35.1 | Right | 0 | Mastopexy & Implant |
| 13 | 70 | V4 | White/NH | 52 | 35.1 | Left | 0 | Flap/NR |
| 14 | 76 | V2 | White/H | 43 | 19 | Right | 0 | Mixed |
| 15 | 76 | V2 | White/H | 43 | 19 | Left | 0 | Mixed |
| 16 | 78 | V1 | White/NH | 40 | 21.9 | Left | 0 | None |
| 17 | 78 | V2 | White/NH | 40 | 21.8 | Left | 0 | None |
| 18 | 103 | V2 | White/NH | 52 | 30 | Right | 0 | Flap/NR |

| | | | | | | | | |
|---|---|---|---|---|---|---|---|---|
| 19 | 109 | V1 | White/NH | 52 | 30.7 | Left | 0 | Flap |
| 20 | 113 | V1 | White/NH | 54 | 35.2 | Right | 0 | Implant |
| 21 | 113 | V2 | White/NH | 54 | 25.9 | Right | 0 | Implant |
| 22 | 113 | V3 | White/NH | 54 | 25.8 | Right | 0 | Implant |
| 23 | 113 | V3 | White/NH | 54 | 25.8 | Left | 0 | Flap |
| 24 | 126 | V1 | White/H | 34 | 25.4 | Right | 0 | None |
| 25 | 126 | V1 | White/H | 34 | 25.4 | Left | 0 | None |
| 26 | 126 | V2 | White/H | 34 | 25.4 | Right | 0 | Implant |
| 27 | 126 | V2 | White/H | 34 | 25.4 | Left | 0 | Implant |
| 28 | 126 | V3 | White/H | 34 | 24 | Right | 0 | Implant |
| 29 | 126 | V3 | White/H | 34 | 24 | Left | 0 | Implant |
| 30 | 127 | V1 | White/NH | 55 | 31.1 | Left | 0 | None |
| 31 | 131 | V1 | White/NH | 51 | 20.4 | Right | 0 | Implant |
| 32 | 131 | V1 | White/NH | 51 | 20.4 | Left | 0 | Implant |
| 33 | 131 | V2 | White/NH | 51 | 19.5 | Right | 0 | Implant |
| 34 | 131 | V2 | White/NH | 51 | 19.5 | Left | 0 | Implant |
| 35 | 131 | V3 | White/NH | 51 | 18.8 | Right | 0 | Implant |
| 36 | 131 | V3 | White/NH | 51 | 18.8 | Left | 0 | Implant |
| 37 | 133 | V2 | White/NH | 46 | 30.3 | Right | 0 | Implant |
| 38 | 159 | V1 | White/NH | 30 | 23.9 | Right | 0 | None |
| 39 | 159 | V1 | White/NH | 30 | 23.9 | Left | 0 | None |
| 40 | 163 | V3 | White/NH | 37 | 24 | Right | 0 | Mastopexy |
| 41 | 163 | V4 | White/NH | 37 | 25 | Right | 0 | Mastopexy |
| 42 | 193 | V3 | White/NH | 54 | 32.4 | Left | 0 | Reduction |
| 43 | A | NA | White/NH | 21 | 19 | Right | 0 | None |
| 44 | A | NA | White/NH | 21 | 19 | Left | 0 | None |
| 45 | B | NA | White/NH | 53 | 19.8 | Right | 0 | None |
| 46 | B | NA | White/NH | 53 | 19.8 | Left | 0 | Flap |

Notes: NH: Non-Hispanic or Latino; H: Hispanic; NR: Nipple reconstruction.

Table 5.3: Demographics and characteristics for participants with breast ptosis grade 1

| **No.** | **Patient ID** | **Visit** | **Race /Ethnicity** | **Age** | **BMI** | **Breast (Right/Left)** | **Ptosis Grade** | **Surgery Type** |
|---|---|---|---|---|---|---|---|---|
| 1 | 42 | V1 | White/NH | 49 | 28.2 | Left | 1 | None |
| 2 | 42 | V3 | White/NH | 49 | 28.4 | Left | 1 | Mastopexy |
| 3 | 42 | V4 | White/NH | 49 | 28.4 | Right | 1 | Flap/NR |
| 4 | 42 | V4 | White/NH | 49 | 28.4 | Left | 1 | Mastopexy |
| 5 | 48 | V1 | White/NH | 49 | 24.3 | Left | 1 | Mastopexy & Implant |
| 6 | 48 | V2 | White/NH | 49 | 24.6 | Left | 1 | Mastopexy & Implant |
| 7 | 57 | V3 | White/NH | 63 | 26.4 | Right | 1 | Mastopexy & Implant |
| 8 | 103 | V2 | White/NH | 52 | 30 | Left | 1 | Flap/NR |
| 9 | 117 | V3 | White/NH | 58 | 28.7 | Right | 1 | None |
| 10 | 127 | V1 | White/NH | 55 | 31.1 | Right | 1 | None |
| 11 | 193 | V2 | White/NH | 54 | 32 | Left | 1 | Reduction |
| 12 | 205 | V1 | White/NH | 57 | 29 | Right | 1 | None |
| 13 | 205 | V1 | White/NH | 57 | 29 | Left | 1 | None |
| 14 | 515 | V1 | White/NH | 55 | 22.4 | Right | 1 | None |
| 15 | 515 | V1 | White/NH | 55 | 22.4 | Left | 1 | None |

Notes: NH: Non-Hispanic or Latino; H: Hispanic; NR: Nipple reconstruction.

Table 5.4: Demographics and characteristics for participants with breast ptosis grade 2

| **No.** | **Patient ID** | **Visit** | **Race /Ethnicity** | **Age** | **BMI** | **Breast (Right/Left)** | **Ptosis Grade** | **Surgery Type** |
|---|---|---|---|---|---|---|---|---|
| 1 | 56 | V1 | White/NH | 54 | 25.9 | Right | 2 | None |
| 2 | 56 | V1 | White/NH | 54 | 25.9 | Left | 2 | None |

| | | | | | | | | |
|---|---|---|---|---|---|---|---|---|
| 3 | 56 | V2 | White/NH | 54 | 27.4 | Left | 2 | None |
| 4 | 70 | V1 | White/NH | 52 | 39.6 | Right | 2 | None |
| 5 | 72 | V1 | White/NH | 47 | 27.3 | Right | 2 | None |
| 6 | 82 | V2 | White/NH | 59 | 32.4 | Left | 2 | Reduction |
| 7 | 133 | V1 | White/NH | 46 | 34.4 | Right | 2 | None |
| 8 | 133 | V1 | White/NH | 46 | 34.4 | Left | 2 | None |
| 9 | 163 | V2 | White/NH | 37 | 26.3 | Right | 2 | None |
| 10 | 208 | V1 | White/NH | 60 | 29 | Left | 2 | None |
| 11 | 532 | V1 | White/NH | 50 | 30.9 | Left | 2 | Partial Mastectomy |
| 12 | 534 | V1 | White/H | 40 | 33.9 | Left | 2 | Partial Mastectomy |
| 13 | D | NA | White/NH | 44 | 27 | Right | 2 | None |
| 14 | D | NA | White/NH | 44 | 27 | Left | 2 | None |
| 15 | E | NA | White/H | 21 | 36 | Right | 2 | None |
| 16 | E | NA | White/H | 21 | 36 | Left | 2 | None |

Notes: NH: Non-Hispanic or Latino; H: Hispanic.

Table 5.5: Demographics and characteristics for participants with breast ptosis grade 3

| **No.** | **Patient ID** | **Visit** | **Race /Ethnicity** | **Age** | **BMI** | **Breast (Right/Left)** | **Ptosis Grade** | **Surgery Type** |
|---|---|---|---|---|---|---|---|---|
| 1 | 58 | V1 | White/NH | 31 | 33.2 | Right | 3 | None |
| 2 | 58 | V1 | White/NH | 31 | 33.2 | Left | 3 | None |
| 3 | 72 | V1 | White/NH | 47 | 27.3 | Left | 3 | Partial Mastectomy |
| 4 | 177 | V1 | White/NH | 55 | 25.5 | Right | 3 | None |
| 5 | 177 | V1 | White/NH | 55 | 25.5 | Left | 3 | None |
| 6 | 215 | V1 | MA/H | 49 | 37.4 | Right | 3 | None |

| | | | | | | | | |
|---|---|---|---|---|---|---|---|---|
| 7 | 215 | V1 | MA/H | 49 | 37.4 | Left | 3 | None |
| 8 | 532 | V1 | Hispanic/H | 50 | 30.9 | Right | 3 | None |
| 9 | 534 | V1 | White/H | 40 | 33.9 | Right | 3 | None |
| 10 | 538 | V1 | White/NH | 52 | 27 | Right | 3 | None |
| 11 | 689 | V1 | White/NH | 66 | 27.6 | Right | 3 | None |
| 12 | 689 | V1 | White/NH | 66 | 27.6 | Left | 3 | None |
| 13 | C | NA | White/NH | 45 | 27 | Right | 3 | None |

Notes: NH: Non-Hispanic or Latino; H: Hispanic.

Table 5.6: Demographics and characteristics for participants with breasts cannot be rated

| **No.** | **Pat. ID** | **Visit** | **Race /Ethnicity** | **Age** | **BMI** | **Breast (Right/Left)** | **Ptosis Grade** | **Surgery Type & Stage** |
|---|---|---|---|---|---|---|---|---|
| 1 | 7 | V2 | White/NH | 54 | 20.6 | Right | CR | Implant/Stage 2 |
| 2 | 7 | V2 | White/NH | 54 | 20.6 | Left | CR | Implant/Stage 2 |
| 3 | 38 | V2 | White/NH | 36 | 19.6 | Right | CR | Implant/Stage 2 |
| 4 | 38 | V2 | White/NH | 36 | 19.6 | Left | CR | Implant/Stage 2 |
| 5 | 42 | V1 | White/NH | 49 | 28.2 | Right | CR | Flap/Stage 0 |
| 6 | 42 | V3 | White/NH | 49 | 28.4 | Right | CR | Flap/Stage 2 |
| 7 | 48 | V1 | White/NH | 49 | 24.3 | Right | CR | Implant/Stage 2 |
| 8 | 56 | V2 | White/NH | 54 | 27.4 | Right | CR | Implant/Stage 2 |
| 9 | 57 | V3 | White/NH | 63 | 26.4 | Left | CR | Flap/Stage 3 |
| 10 | 67 | V1 | White/H | 50 | 23.4 | Left | CR | Implant/Stage 3 |
| 11 | 67 | V2 | White/H | 50 | 25.6 | Left | CR | Implant/Stage 3 |
| 12 | 67 | V3 | White/H | 50 | 26.4 | Left | CR | Implant/Stage 3 |
| 13 | 68 | V2 | White/NH | 54 | 21.9 | Right | CR | Implant/Stage 1 |
| 14 | 68 | V2 | White/NH | 54 | 21.9 | Left | CR | Implant/Stage 1 |
| 15 | 68 | V3 | White/NH | 54 | 22.3 | Right | CR | Implant/Stage 2 |
| 16 | 68 | V3 | White/NH | 54 | 22.3 | Left | CR | Implant/Stage 2 |

| | | | | | | | | |
|---|---|---|---|---|---|---|---|---|
| 17 | 70 | V1 | White/NH | 52 | 39.6 | Left | CR | Flap/Stage 1 |
| 18 | 70 | V2 | White/NH | 52 | 35.4 | Left | CR | Flap/Stage 3 |
| 19 | 78 | V1 | White/NH | 40 | 21.9 | Right | CR | Implant/Stage 2 |
| 20 | 78 | V2 | White/NH | 40 | 21.8 | Right | CR | Implant/Stage 3 |
| 21 | 81 | V1 | White/NH | 46 | 38.4 | Right | CR | Flap/Stage 3 |
| 22 | 81 | V1 | White/NH | 46 | 38.4 | Left | CR | Flap/Stage 3 |
| 23 | 81 | V2 | White/NH | 46 | 39.2 | Right | CR | Flap/Stage 3 |
| 24 | 81 | V2 | White/NH | 46 | 39.2 | Left | CR | Flap/Stage 3 |
| 25 | 82 | V2 | White/NH | 59 | 32.4 | Right | CR | Implant/Stage 2 |
| 26 | 83 | V1 | White/NH | 51 | 23.3 | Right | CR | Implant/Stage 1 |
| 27 | 83 | V1 | White/NH | 51 | 23.3 | Left | CR | Implant/Stage 1 |
| 28 | 83 | V2 | White/NH | 51 | 26 | Right | CR | Implant/Stage 2 |
| 29 | 83 | V2 | White/NH | 51 | 26 | Left | CR | Implant/Stage 2 |
| 30 | 91 | V1 | White/NH | 41 | 21.1 | Right | CR | Implant/Stage 1 |
| 31 | 91 | V1 | White/NH | 41 | 21.1 | Left | CR | Implant/Stage 1 |
| 32 | 91 | V2 | White/NH | 41 | 19.1 | Right | CR | Implant/Stage 3 |
| 33 | 91 | V2 | White/NH | 41 | 19.1 | Left | CR | Implant/Stage 3 |
| 34 | 101 | V1 | BAA/NH | 40 | 25.3 | Right | CR | Implant/Stage 1 |
| 35 | 101 | V1 | BAA/NH | 40 | 25.3 | Left | CR | Implant/Stage 1 |
| 36 | 103 | V1 | White/NH | 52 | 30.2 | Right | CR | Flap/Stage 1 |
| 37 | 103 | V1 | White/NH | 52 | 30.2 | Left | CR | Flap/Stage 1 |
| 38 | 109 | V1 | White/NH | 52 | 30.7 | Right | CR | Flap/Stage 1 |
| 39 | 113 | V1 | White/NH | 54 | 35.2 | Left | CR | Flap/Stage 1 |
| 40 | 113 | V2 | White/NH | 54 | 25.9 | Left | CR | Flap/Stage 2 |
| 41 | 117 | V3 | White/NH | 58 | 28.7 | Left | CR | Implant/Stage 2 |
| 42 | 127 | V2 | White/NH | 55 | 31.7 | Right | CR | Implant/Stage 1 |
| 43 | 127 | V2 | White/NH | 55 | 31.7 | Left | CR | Implant/Stage 1 |
| 44 | 127 | V3 | White/NH | 55 | 31.7 | Right | CR | Implant/Stage 2 |
| 45 | 127 | V3 | White/NH | 55 | 31.7 | Left | CR | Implant/Stage 2 |

| | | | | | | | | |
|---|---|---|---|---|---|---|---|---|
| 46 | 133 | V2 | White/NH | 46 | 30.3 | Left | CR | Implant/Stage 1 |
| 47 | 159 | V2 | White/NH | 30 | 24.6 | Right | CR | Implant/Stage 1 |
| 48 | 159 | V2 | White/NH | 30 | 24.6 | Left | CR | Implant/Stage 1 |
| 49 | 159 | V3 | White/NH | 30 | 23.8 | Right | CR | Implant/Stage 2 |
| 50 | 159 | V3 | White/NH | 30 | 23.8 | Left | CR | Implant/Stage 2 |
| 51 | 163 | V2 | White/NH | 37 | 26.3 | Left | CR | Flap/Stage 1 |
| 52 | 163 | V3 | White/NH | 37 | 24 | Left | CR | Flap/Stage 3 |
| 53 | 163 | V4 | White/NH | 37 | 25 | Left | CR | Flap/Stage 3 |
| 54 | 177 | V3 | White/NH | 55 | 26.2 | Right | CR | Implant/Stage 1 |
| 55 | 177 | V3 | White/NH | 55 | 26.2 | Left | CR | Implant/Stage 1 |
| 56 | 182 | V2 | White/NH | 43 | 25.7 | Right | CR | Flap/Stage 1 |
| 57 | 182 | V2 | White/NH | 43 | 25.7 | Left | CR | Flap/Stage 1 |
| 58 | 182 | V3 | White/NH | 43 | 23.9 | Right | CR | Flap/Stage 1 |
| 59 | 182 | V3 | White/NH | 43 | 23.9 | Left | CR | Flap/Stage 1 |
| 60 | 193 | V2 | White/NH | 54 | 32 | Right | CR | Flap/Stage 1 |
| 61 | 193 | V3 | White/NH | 54 | 32.4 | Right | CR | Flap/Stage 3 |

Notes: BAA: Black_AfricanAmerican; NH: Non-Hispanic or Latino; H: Hispanic.

CR: Cannot Rate.

Stage 0: Had mastectomy, no reconstruction;

Stage 1: Had tissue expander placement or flap procedure;

Stage 2: Had exchange procedure for either implant or flap;

Stage 3: Completed revision surgeries.

## 5.5 Results

We validate our proposed lowest breast contour detection algorithm using the 3D surface images for 77 participants, 151 breasts. Data for three representative participants are presented in Fig. 5.7. Cropped torsos for the three representative images are displayed in Fig. 5.7 (a), (c), and (e) respectively. For representative 1, both breasts are ptosis grade 0, and left breast had flap surgery. For representative 2, right breast has ptosis grade 2 without surgery, and left breast has ptosis grade 3 with partial mastectomy. For representative 3, right breast has incomplete implant surgery (stage 2), this breast cannot be rated since the nipple has not been reconstructed yet; left breast has ptosis grade 1 with mastopexy and implant surgery. The lowest breast contour detection results for the three representatives are displayed in Fig. 5.7 (b), (d), and (f) respectively. Blue points are manually selected contour points, which are used as ground truth for comparison. Green points are the lowest breast contour points detected using our proposed algorithm. The red curve is obtained via cubic-spline fitting of the detected contour points in green. As seen in Fig 5.7 (b), (d) and (f), high correspondence is achieved between the manually selected points and the automatically detected breast contour.

Table 5.7 presents the average distance and dice coefficients for automatically detected versus manually selected lowest breast contours for total 151 breasts. In the 151 breasts, 46 breasts have ptosis grade 0; 15 breasts have ptosis grade 1; 16 breasts have ptosis grade 2; 13 breasts have ptosis grade 3. These breasts which have nipples and can be rated are either pre-operative or have the following previous surgeries: mastopexy, reduction, partial mastectomy, implant, flap, and combination of implant and flap. And also, in the 151 breasts, 61 breasts have no nipples and cannot be rated due to the incomplete implant or flap surgeries. The 61 breasts include 4 surgery stages: (1) stage 0: had mastectomy, no reconstruction; (2) stage 1: had tissue expander placement or flap procedure; (3) stage 2: had exchange procedure for either implant or flap; (4) stage 3: completed revision surgeries. The mean of the average distances for the total 151 breasts between automatically detected

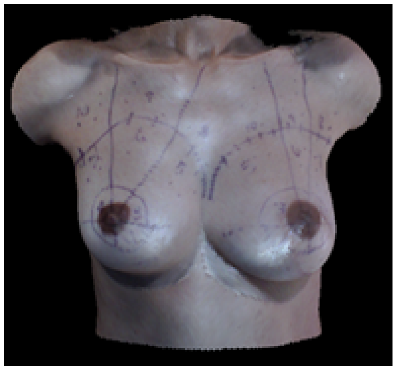

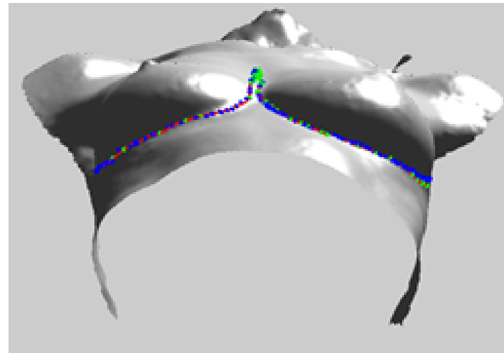

(a) (b)

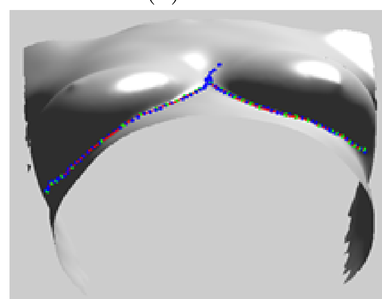

(c) (d)

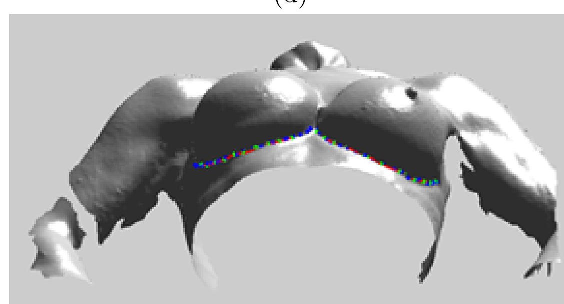

(e) (f)

Figure 5.7: (a) 3D image showing the breast area for representative 1. Both breasts are ptosis grade 0. Left breast had flap surgery. (b) Result for representative 1. Detected lowest breast contour points (green) and manually selected contour points (blue) displayed on surface. The contour (red) is obtained via cubic-spline fitting of the detected contour points in green. (c) 3D image showing the breast area for representative 2. Right breast has ptosis grade 2 without surgery. Left breast has ptosis grade 3 with partial mastectomy. (d) Result for representative 2. (e) 3D image showing the breast area for representative 3. Right breast has incomplete implant surgery (stage 2). This breast cannot be rated since the nipple has not been reconstructed yet. Left breast has ptosis grade 1 with mastopexy and implant surgery. (f) Result for representative 3.

and manually selected lowest breast contours is $(1.642 \pm 0.758)mm$. The distance threshold for dice coefficient represents the separation between the points on the two contours. We tested dice coefficients using 6 thresholds: $0.5mm$, $1.0mm$, $2.0mm$, $3.0mm$, $4.0mm$, and $5.0mm$. The mean of the dice coefficients is the average value for the 151 breasts at a given distance threshold. From Table 5.7 we can see that as the distance threshold for similarity between two contours is increased, the dice coefficient also increases. At a separation distance in the range of $4mm - 5mm$ between the automatically detected and manually annotated breast contours, we have very high dice coefficient values ($0.943 - 0.971$). At a resolution of $2mm - 3mm$ the similarity is around $0.715 - 0.872$, and is reduced only for very low threshold values of $1mm$ (40.5%), and $0.5mm$ (20.5%).

Table 5.7: Lowest breast contour detection error for total 151 breasts

| | **Average distance (mm)** | **Dice Coefficient** | | | | | |
|---|---|---|---|---|---|---|---|
| | | **Distance threshold** | | | | | |
| | | **0.5 mm** | **1.0 mm** | **2.0 mm** | **3.0 mm** | **4.0 mm** | **5.0 mm** |
| **Mean** | 1.642 | 0.205 | 0.405 | 0.715 | 0.872 | 0.943 | 0.971 |
| **Standard deviation** | 0.758 | 0.105 | 0.149 | 0.162 | 0.119 | 0.073 | 0.049 |

Table 5.8 present the average distance and dice coefficients for 46 breasts which have ptosis grade 0. The mean of the average distances between automatically detected contours and the ground truth is $(1.727 \pm 0.981)mm$. At a distance threshold in the range of $4mm - 5mm$, high dice coefficient values $0.941 - 0.967$ are obtained. At a separation distance of $2mm - 3mm$ the dice coefficient values are between $0.719 - 0.883$. At a low resolution of $1mm$ and $0.5mm$, the similarity is reduced to 42.2% and 22.7%.

Table 5.8: Lowest breast contour detection error for breasts with ptosis grade 0 (46 breasts)

| | **Average distance (mm)** | **Dice Coefficient** | | | | | |
|---|---|---|---|---|---|---|---|
| | | **Distance threshold** | | | | | |
| | | **0.5 mm** | **1.0 mm** | **2.0 mm** | **3.0 mm** | **4.0 mm** | **5.0 mm** |
| **Mean** | 1.727 | 0.227 | 0.422 | 0.719 | 0.883 | 0.941 | 0.967 |
| **Standard deviation** | 0.981 | 0.11 | 0.148 | 0.144 | 0.105 | 0.071 | 0.047 |

Table 5.9 present the average distance and dice coefficients for 15 breasts which have ptosis grade 1. The mean of the average distances is $(1.403 \pm 0.431)mm$. Very high dice coefficient values $0.962-0.989$ are obtained at distance threshold in a range of $4mm - 5mm$. At a separation distance of $2mm - 3mm$ the dice coefficient values are between $0.772 - 0.900$. At a low resolution of $1mm$ and $0.5mm$, the similarity is reduced to 44.8% and 21.9% respectively.

Table 5.9: Lowest breast contour detection error for breasts with ptosis grade 1 (15 breasts)

| | **Average distance (mm)** | **Dice Coefficient** | | | | | |
|---|---|---|---|---|---|---|---|
| | | **Distance threshold** | | | | | |
| | | **0.5 mm** | **1.0 mm** | **2.0 mm** | **3.0 mm** | **4.0 mm** | **5.0 mm** |
| **Mean** | 1.403 | 0.219 | 0.448 | 0.772 | 0.9 | 0.962 | 0.989 |
| **Standard deviation** | 0.431 | 0.117 | 0.146 | 0.133 | 0.102 | 0.056 | 0.021 |

Table 5.10 present the average distance and dice coefficients for 16 breasts which have ptosis grade 2. The mean of the average distances is $(1.617 \pm 1.089)mm$. At distance threshold in a range of $4mm - 5mm$, dice coefficient values are between

$0.948 - 0.968$. At that of $2mm - 3mm$ the dice coefficient values are between $0.743 - 0.893$. At a low resolution of $1mm$ and $0.5mm$, the dice coefficients are 44.6% and 21.7% respectively.

Table 5.10: Lowest breast contour detection error for breasts with ptosis grade 2 (16 breasts)

| | **Average distance (mm)** | **Dice Coefficient** | | | | | |
|---|---|---|---|---|---|---|---|
| | | **Distance threshold** | | | | | |
| | | **0.5 mm** | **1.0 mm** | **2.0 mm** | **3.0 mm** | **4.0 mm** | **5.0 mm** |
| **Mean** | 1.617 | 0.217 | 0.446 | 0.743 | 0.893 | 0.948 | 0.968 |
| **Standard deviation** | 1.089 | 0.128 | 0.195 | 0.202 | 0.125 | 0.09 | 0.076 |

Table 5.11 present the average distance and dice coefficients for 13 breasts which have ptosis grade 3. The mean of the average distances is $(1.290 \pm 0.279)mm$. At separation distance in a range of $4mm - 5mm$, very high dice coefficient values $0.970 - 0.984$ are obtained. At that of $2mm - 3mm$ the similarity is around $0.823 - 0.930$. At a low separation distance of $1mm$ and $0.5mm$, the dice coefficient values are 46.8% and 21.3%.

Table 5.11: Lowest breast contour detection error for breasts with ptosis grade 3 (13 breasts)

| | **Average distance (mm)** | **Dice Coefficient** | | | | | |
|---|---|---|---|---|---|---|---|
| | | **Distance threshold** | | | | | |
| | | **0.5 mm** | **1.0 mm** | **2.0 mm** | **3.0 mm** | **4.0 mm** | **5.0 mm** |
| **Mean** | 1.29 | 0.213 | 0.468 | 0.823 | 0.93 | 0.97 | 0.984 |
| **Standard deviation** | 0.279 | 0.062 | 0.101 | 0.09 | 0.069 | 0.046 | 0.037 |

Table 5.12 present the average distance and dice coefficients for 61 breasts which cannot be rated due to the incomplete surgeries. The mean of the average distances is $(1.718 \pm 0.553)mm$. At separation distance in a range of $4mm - 5mm$, dice coefficient values are between $0.932 - 0.967$. At that of $2mm - 3mm$ the similarity is around $0.667 - 0.840$. At a low separation distance of $1mm$ and $0.5mm$, the dice coefficient values are 35.8% and 18.0%.

Table 5.12: Lowest breast contour detection error for breasts which cannot be rated (61 breasts)

| | **Average distance (mm)** | **Dice Coefficient** | | | | | |
|---|---|---|---|---|---|---|---|
| | | **Distance threshold** | | | | | |
| | | **0.5 mm** | **1.0 mm** | **2.0 mm** | **3.0 mm** | **4.0 mm** | **5.0 mm** |
| **Mean** | 1.718 | 0.18 | 0.358 | 0.667 | 0.84 | 0.932 | 0.967 |
| **Standard deviation** | 0.553 | 0.097 | 0.135 | 0.168 | 0.133 | 0.078 | 0.05 |

Fig. 5.8 shows the average distances between detected lowest breast contours and ground truth for five categories. The average distances between automatically detected contour and the ground truth for breasts in these five categories are in a range $1.290mm \sim 1.727mm$. Fig. 5.9 shows the mean of the dice coefficients for different distance threshold for five categories. For the $2mm - 3mm$ distance threshold, the dice coefficient values for the five categories are around $0.667 - 0.930$; for the threshold range of $4mm - 5mm$, the dice coefficient are $0.932 - 0.989$; At a low separation distance of $1mm$ and $0.5mm$, the dice coefficient values are $0.180 - 0.468$.

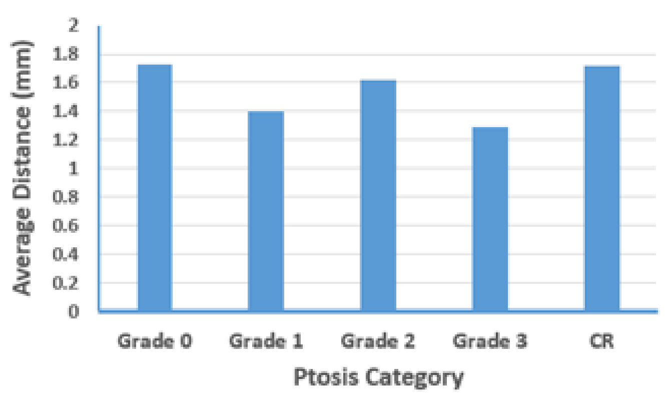


Figure 5.8: Average distances between detected lowest breast contours and ground truth for five categories.

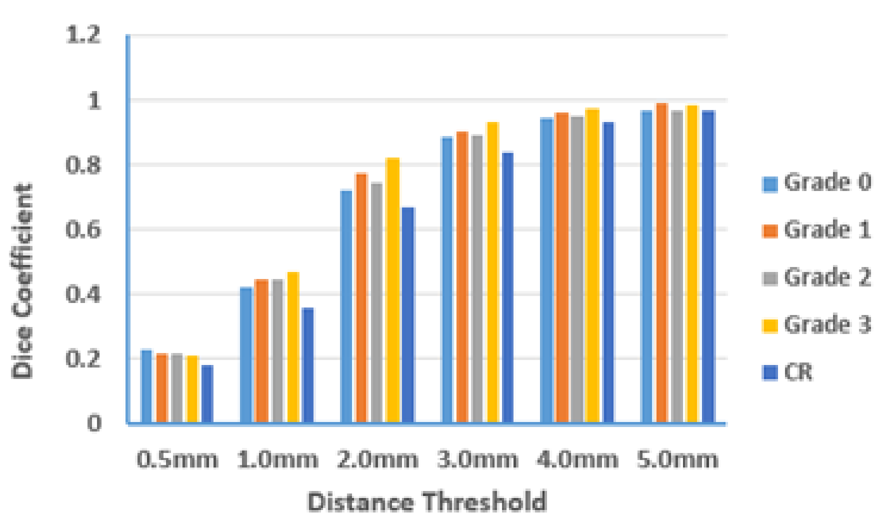


Figure 5.9: Dice coefficients for different distance threshold for five categories.

## 5.6 Conclusions

We have developed a curvature-based automated lowest breast contour detection algorithm for 3D images of the female torso. Our approach employs shape index and the minimum principle curvature and can detect the lowest breast contour compare to the manually selected contour with an average accuracy of $(1.642 \pm 0.758)mm$, for the 151 breasts which include breasts of ptosis grades 0, 1, 2, 3 and even those of not being able to be rated due to incomplete surgeries and without nipples. The mean of the average distances for the total 151 breasts between automatically detected contour and the ground truth is $(1.642 \pm 0.758)mm$, which is relatively small. For the $2mm - 3mm$ distance threshold, the mean of the dice coefficients for the 151 breasts between automatically detected contours and the ground truth is around $0.715 - 0.872$; for the threshold range of $4mm - 5mm$, the mean of the dice coefficient is $0.943 - 0.971$, which is relatively high.

Our proposed algorithm also shows robustness for all five categories:

For ptosis grades 0, 1, 2, and 3, the breasts in these four categories have nipples and are pre-operative or have previous surgeries as mastopexy, reduction, partial mastectomy, implant, flap, and combination of implant and flap. The mean of the average distances between automatically detected contour and the ground truth for breasts in these four categories is in a range $(1.290 \pm 0.279)mm \sim (1.727 \pm 0.981)mm$. For the $2mm - 3mm$ distance threshold, the mean of the dice coefficients for the four categories is around $0.719 - 0.930$; for the threshold range of $4mm - 5mm$, the mean of the dice coefficient is $0.941 - 0.989$.

For the 61 breasts which have no nipples and cannot be rated due to the incomplete implant or flap surgeries, this category include all four intermediate stages of surgeries. The mean of the average distances between automatically detected contour and the ground truth for this category is $(1.718 \pm 0.553)mm$. For the $2mm - 3mm$ distance threshold, the mean of the dice coefficients is around $0.667 - 0.840$; for the threshold range of $4mm - 5mm$, the mean of the dice coefficient is $0.932 - 0.967$.

Accurate detection of the lowest breast contour is important for breast esthetics during breast reconstruction for woman with breast cancer. The detected lowest breast contours facilitate computation of morphological measures such as volume, and facilitates the identification of other characteristics of the breast morphology such as ptosis and nipple, which are important information for pre-operative planning and post-operative assessment of outcomes in breast reconstruction.

# Chapter 6

# Multi-View 3D Data Fusion for Visualization of the Inframammary Fold in Women with Ptotic Breasts

## 6.1 Introduction

Inframammary fold (IMF) is the feature of human anatomy which is a natural boundary of a breast from below, i.e., the boundary at which the breast meets the chest wall (Fig. 6.1). It is a critical landmark for breast surgery and morphometry.

The last decade has seen a steady increase in the use of 3D imaging for visualization and quantification of breast aesthetics in cosmetic and reconstructive breast surgery. 3D images of the female torso acquired in the upright position not only enable a 180° panoramic visualization of the breasts, but also permit objective evaluation of breast aesthetics related to symmetry, projection, ptosis and volume.

Objective measurements typically involve the use of anatomical landmarks (fiducial points) on the torso, such as the sternal notch, nipples, transition point and the IMF, and are performed on images acquired in the upright position.

However, an inherent limitation of photography is the inability to image areas that are occluded. Thus, when acquiring images of women with highly ptotic (sagging) breasts (ptosis grade $\geq 2$), the anatomical IMF is occluded and cannot be visualized in the upright position which is conventionally used for surgical planning and outcome assessment (see Fig.6.1a). Consequently, it is impossible to delineate the anatomical IMF in the 3D images of women with ptotic breasts in an upright position, and we can only detect the lowest contour of the breast touching the abdomen (i.e., the contour delineation the boundary at which the breast is touching the abdominal wall and is up under the breast in women with high degrees of ptosis).

Delineation of the anatomical IMF on the upright view image is critical since the IMF is a defining element in the shape and structure of the female breast [92]. Evaluation of the IMF and its position is an important aesthetic consideration after breast reconstruction or augmentation [93]. The IMF is an important landmark that can be used to grade breast ptosis [94, 95] and facilitate volume calculation [96–98]. The distances from the sternal notch, nipple, lowest visible point, and breast base to the IMF are usually measured to evaluate the breast shape at a time point or to estimate changes in shape over time [95–103]. The inframammary fold position change is also quantified and compared at a time point or longitudinally along with analysis of breast and chest wall asymmetries [99, 101, 102]. These estimates can be useful in pre-operative planning of the surgical procedure, with potential for obtaining an aesthetically acceptable breast shape, and ultimately, can serve to optimize patient satisfaction in cosmetic and reconstructive breast surgeries [100]. The IMF facilitates breast reconstruction [92, 93] and the inframammary incision is the simplest and most straightforward access incision approach in breast augmentation [104]. It provides the best access with surgical control and direct visualization to the subglandular, subfascial, and subpectoral planes without violating the breast parenchyma during augmentation.

However, in women with high degrees of ptosis ($\geq 2$), the anatomical position of the IMF on the chest wall is occluded due to the sagging breast. In such cases, the anatomical IMF cannot be visualized in the upright position, and the physician has to manually lift the breast to localize the IMF. However, such manipulations are impossible in static images of the torso acquired in the upright position, and this limits the ability to perform a number of quantitative assessments involving the IMF on images of women with ptotic breasts [99, 103].

To overcome this problem, we proposed a data fusion technique with 3D multi-view (upright and supine) images to visualize the anatomical IMF in an upright image, which utilizes the visibility of IMF in supine images (Fig. 6.1b).

(a) (b)

Figure 6.1: IMF (dashed yellow line) plotted in 3D images from women with highly ptotic breasts. (a) Virtual IMF is plotted in upright image from women with highly ptotic breasts. The real IMF is not visible in the upright 3D image. (b) Real IMF is visible and coincides with the lowest breast contour in the supine image from women with highly ptotic breasts

## 6.2 Algorithm

### 6.2.1 Overview

The overview of multi-view 3D data fusion technique for visualization of the IMF in upright images from women with ptotic breasts is illustrated in Fig. 6.2. The multi-view (upright and supine) images are processed as follows. First, we identify the points along the lowest breast contour touching the abdomen on the surface mesh in both the upright and supine images employing surface curvature analysis. Cubic-spline fitting of the identified points is then used to estimate the lowest breast contour. Next we register the upright and supine 3D images and employ the transformation parameters obtained from registration to superimpose the detected lowest breast contour from the supine image onto the upright image. The anatomical IMF is visible in the supine position for breasts which are ptotic in the upright position. So the detected lowest breast contours in the supine images are the anatomical IMF. Thus the fusion technique enables visualization of the anatomical IMF position for ptotic breasts in the upright images.

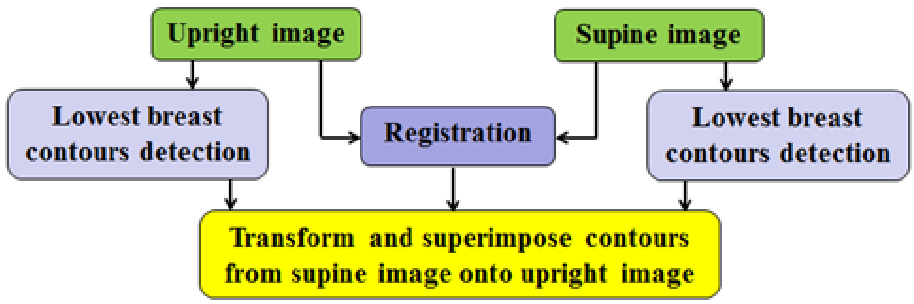


Figure 6.2: Overview of multi-view 3D data fusion for visualization of the IMF in upright images from women with ptotic breasts

### 6.2.2 Detection of Lowest Breast Contour

We apply our automated lowest breast contour detection algorithm for 3D images of the female torso described in Chapter 5 to detect contours from multi-view images. This approach employs shape index and the minimum principle curvature and can obtain accurate lowest breast contour.

### 6.2.3 Registration of 3D Torso Images

In Chapter 4, we have described our registration algorithm for multiple-visit images during breast reconstruction, in which two fiducial points, the sternal notch (SN) and umbilicus (UM) were manually identified as two control points and other thirteen control points were automatically selected based on the location of SN and UM.

To overcome operator bias caused by manual fiducial points selection and location change of UM between multiple-visit images caused by breast reconstruction surgery, we optimize the selection of the locations of SN and UM, and consequently the locations of all other thirteen control points in the target image.

In this multi-view 3D data fusion technique, we adapt our previously developed registration algorithm for the transformation of 3D images taken in the supine position to an upright position, i.e., from $0°$ to $90°$. In this study, the UM could not be used as a control point, since movement of the torso from the upright to the supine position is likely to result in the displacement of the soft tissues in the abdominal region which can result in some displacement of the UM position between the upright and supine position. Thus due to the non-rigidity of the UM position across the upright and supine position, in this study we use the midline point M positioned along the medial axis at the midpoint of the line joining the left and right nipples as the second control point (see Fig. 6.3). Let $d$ represent the straight line distance between SN and M. The other thirteen control points are equally spaced ($\frac{d}{6}$) along $x$ and $y$ directions. To improve precision, $z$ coordinates of the thirteen points were determined using linear interpolation in the surface mesh. Thus we obtained a total of fifteen control points.

The fifteen control points obtained based on SN and M are used during registration instead of those obtained based on SN and UM in previously developed registration algorithm. Image alignment is based on the coordinates of SN and M, we translated and rotated image about $Z$, $X$, and $Y$-axes such that SN is at the origin, the line joining SN-M is coincident to $Y$-axis, and the surface is forward facing. We optimize the registration of the SN and M by searching for the most optimal corresponding points between supine and upright images to overcome the operator bias introduced by manual fiducial points identification and discrepancies of identified M between different images caused by, e.g., breast asymmetry in the same image and breast shape changes in different images.

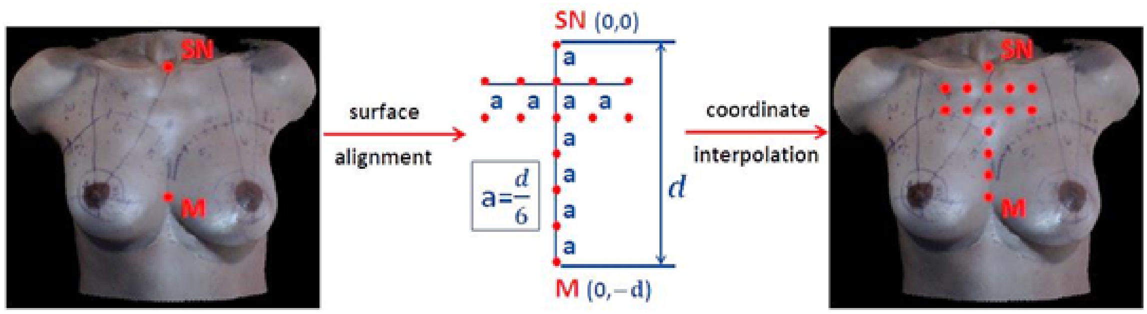


Figure 6.3: Control points selected on the torso for 3D correspondence

## 6.3 Datasets

Supine and upright images from mannequin and five participants were used for multi-view 3D data fusion. Age, race/ethnicity, BMI, breast ptosis grade, and previous breast surgery information for the five participants are listed in Table 6.1.

Table 6.1: Demographics and characteristics of participants

| **Participants** | **Age** | **Race/Ethnicity** | **BMI** | **Weight Status** | **Ptosis Grade** | **Previous breast surgery** |
|---|---|---|---|---|---|---|
| A | 21 | White/NH | 19 | Normal | 0 | None |
| B | 53 | White/NH | 19.8 | Normal | 0 | Left breast flap |
| C | 45 | White/NH | 27 | Overweight | 3 | None |
| D | 44 | White/NH | 27 | Overweight | 2 | None |
| E | 21 | White/H | 36 | Obese | 2 | None |

Notes: NH: Non-Hispanic or Latino; H: Hispanic.

## 6.4 Results

Results for mannequin images are presented in Fig. 6.4. Fig. 6.4 (c)-(d) show the detected lowest breast in the forward facing and backward facing views of the 3D upright images. Blue lines represent the lowest breast contours detected in the upright images. Red contours are the detected lowest breast contours transformed from the supine images and superimposed on the upright images. Fig. 6.4(e) shows 2D projections of detected contours displayed on the fingerprint projection of the 3D upright images. Contours detected from the supine images are superimposed on the upright images. Fig. 6.4(f) shows 2D fingerprint of 3D supine images with detected contours. Contours detected from the upright images are superimposed on the supine image. Morphology of breasts for mannequin has no change between upright position and supine position. We can see that the detected lowest breast contours (i.e., IMF) from upright image and supine image are exactly matched after transformation and superimposition.

Results for five participants, (i) No ptosis, (ii) Ptosis grade of 2, and (iii) Ptosis grade of 3 are presented in Fig. 6.5-6.9, respectively. The anatomical IMF is visible in the supine position for breasts which are both not ptotic and ptotic in the upright position. The detected lowest breast contours in the supine images are anatomical IMF. So the red contours in Fig. 6.5-6.9, (c)-(d) are anatomical IMF transformed from the supine images and represent the positions of the anatomical IMF in the upright images.

As seen in Fig. 6.5-6.6, for non-ptotic breasts (ptosis degree <1), the anatomical IMF is visible in both the upright (Fig. 6.5-6.6 (a)) and the supine (Fig. 6.5-6.6(b)) images, and coincides with the detected lowest breast contour. These data validate that the lowest breast contour detected in the supine image closely estimates the position of the anatomical IMF.

For a ptosis grade of 2, the anatomical IMF is occluded in the upright images (Fig. 6.7-6.8(a)), but can be visualized in the supine images (Fig. 6.7-6.8(b)). As seen in Fig. 6.7-6.8, (c)-(f), the lowest breast contours, i.e., anatomical IMF (red), detected from the supine image is higher than the lowest breast contour (blue) that is detected from the upright image. These results demonstrate that 3D data fusion of information from the supine images can be used to visualize structures that are occluded from the upright images.

For breasts of ptosis grade 3 in Fig. 6.9, the anatomical IMF is also occluded in the upright image (Fig. 6.9(a)), but can be visualized in the supine image (Fig. 6.9(b)). Due to data missing during image acquisition along the lowest contour area of left breast for the upright image (Fig. 6.9(a)), we were unable to run the proposed algorithm to estimate the left lowest breast contour for this image. But the detected lowest contours of right breasts for both the upright and supine images are presented in Fig. 6.9 (c)-(f), and demonstrate that the 3D data fusion technique can be used to visualize the occluded IMF in the upright images of women with high breast ptosis.

## 6.5 Conclusions

We have designed a data fusion technique with 3D multi-view (upright and supine) images to visualize the IMF which is typically occluded from the upright view for women with ptotic breasts. The detected lowest contour of the breast touching the abdomen in the supine image (that represents the anatomical IMF) is transformed and superimposed onto the upright image. Our experimental results on mannequin images show that the IMFs from upright position and supine position can be exactly matched using the data fusion technique. The results on participants with non-ptotic breasts demonstrate that the lowest breast contour detected in the supine image can closely estimate the position of the anatomical IMF in the upright image. And the results on participants with breasts of ptosis grades 2 and 3 validate that the lowest breast contour detected in the supine image (the anatomical IMF) can be used to visualize the anatomical IMF position for ptotic breasts in the upright image.

The upright view image is conventionally used for surgical planning and outcome assessment in plastic surgery, both for breast reconstruction after oncologic surgery and for cosmetic augmentation/reduction procedures. An inherent limitation of the 3D upright view image is the inability to image areas that are occluded. Thus, some important landmarks and structures (e.g., the anatomical IMF) are occluded and cannot be visualized in the upright position. However, delineation of the anatomical IMF is critical since its position is an important consideration for both outcome esthetic evaluation and surgical planning in plastic surgery, and will ultimately serve to optimize patient satisfaction in cosmetic and reconstructive breast surgeries. The proposed data fusion technique with 3D multi-view (upright and supine) images to visualize the IMF in the upright image is a critical landmark for breast surgery and morphometry, and has potential for future clinical implementation.

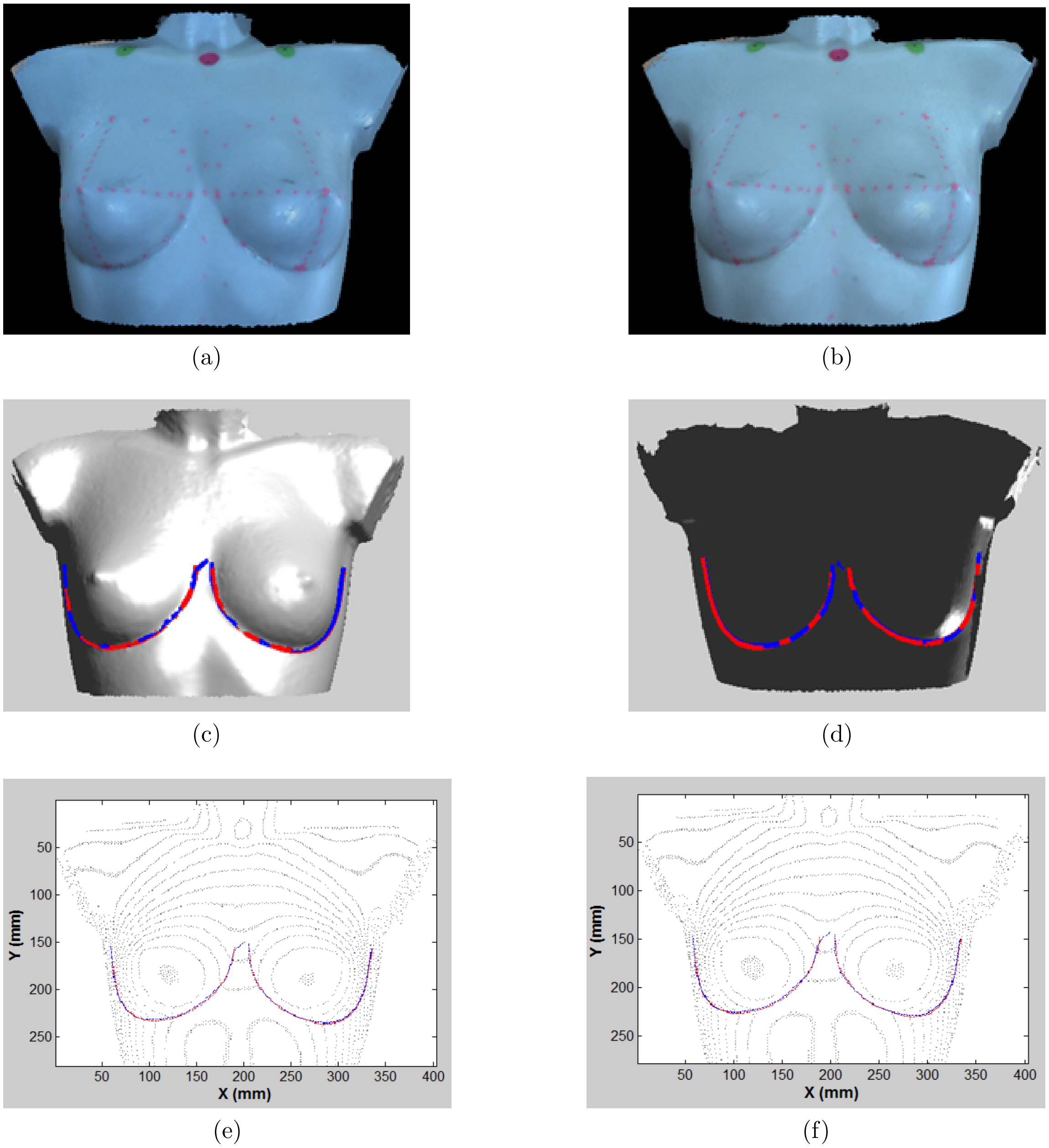


Figure 6.4: Mannequin images. (a) Upright position. (b) Supine position. (c) The detected lowest breast contours displayed in the upright image (front). (d) The detected lowest breast contours displayed in the upright image (back). (e) 2D projection of detected contours displayed on fingerprint projection of the upright image. (f) 2D projection of detected contours displayed on fingerprint projection of the supine image. Blue lines represent the lowest breast contours (i.e., the anatomical IMF) detected in the upright image, whereas red lines are the lowest breast contours (i.e., the anatomical IMF) detected from the supine image.

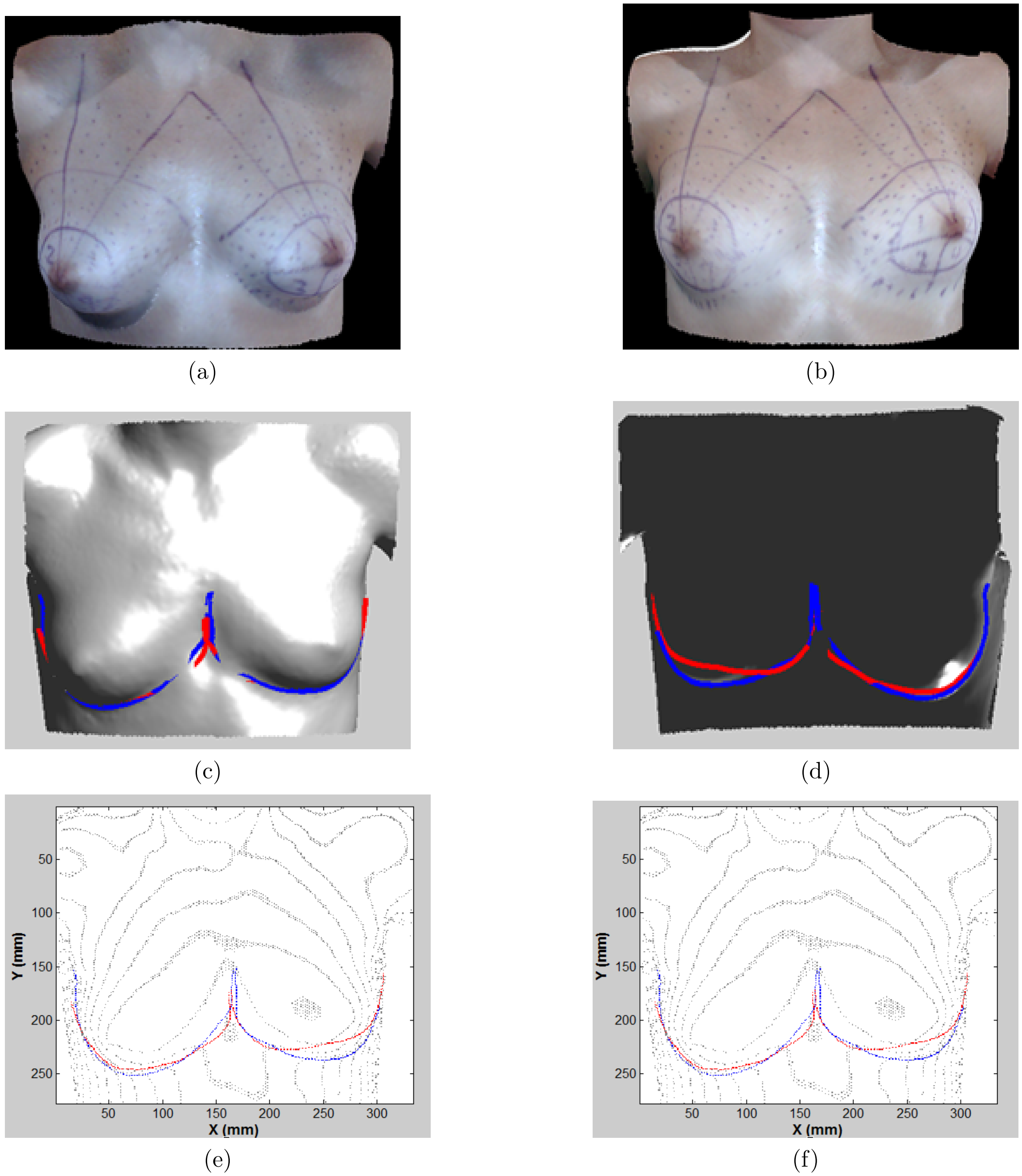


Figure 6.5: Subject with no ptosis. (a) 3D image in the upright position. (b) 3D image in the supine position. (c) The detected lowest breast contours displayed in the upright image (front). (d) The detected lowest breast contours displayed in the upright image (back). (e) 2D projection of detected contours displayed on fingerprint projection of the upright image. (f) 2D projection of detected contours displayed on fingerprint projection of the supine image. Blue lines represent the lowest breast contours detected in the upright images, whereas red lines are the lowest breast contours detected from the supine image (i.e., the anatomical IMF).

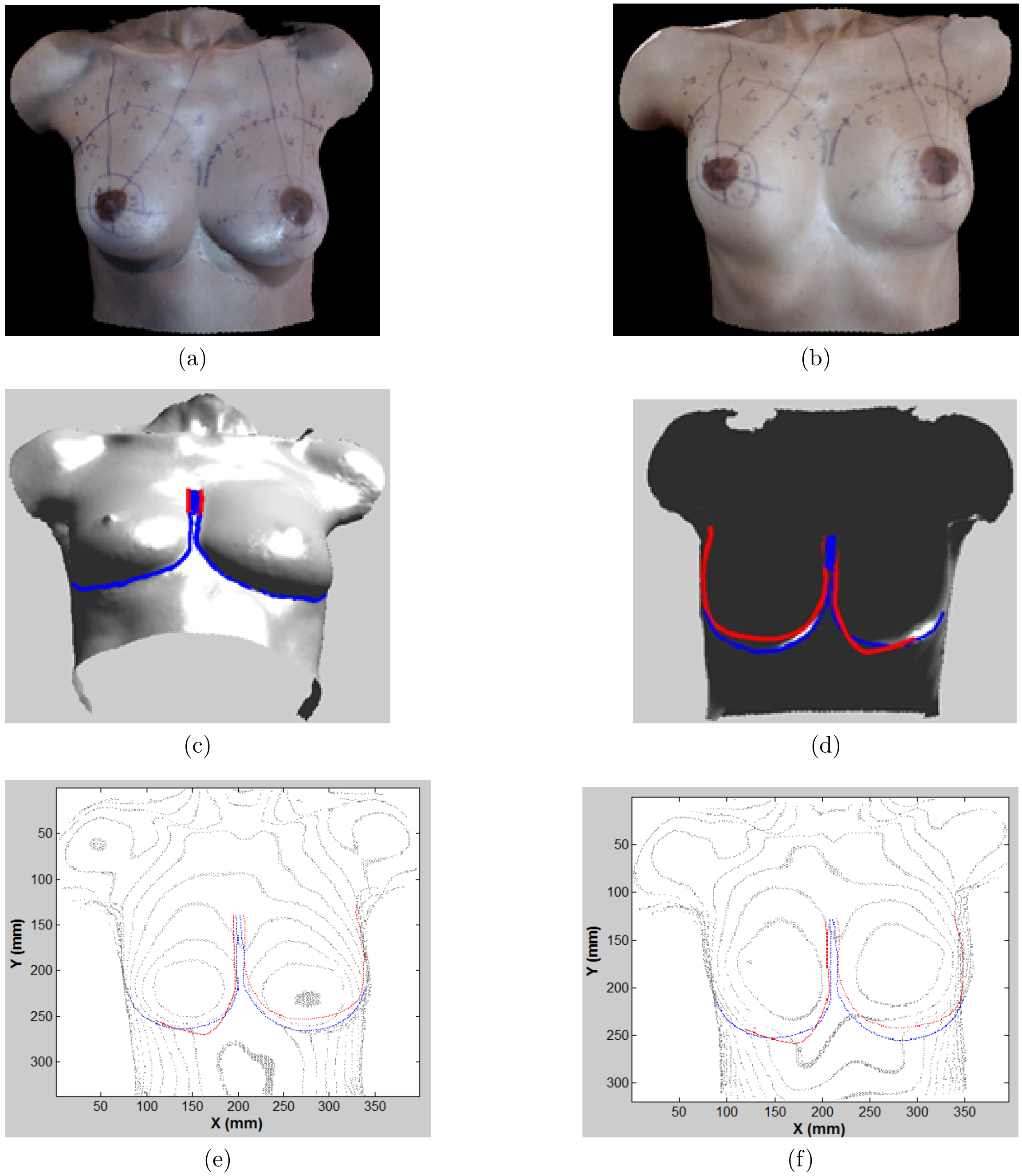


Figure 6.6: Another subject with no ptosis. (a) 3D image in the upright position. (b) 3D image in the supine position. (c) The detected lowest breast contours displayed in the upright image (front). (d) The detected lowest breast contours displayed in the upright image (back). (e) 2D projection of detected contours displayed on fingerprint projection of the upright image. (f) 2D projection of detected contours displayed on fingerprint projection of the supine image. Blue lines represent the lowest breast contours detected in the upright images, whereas red lines are the lowest breast contours detected from the supine image (i.e., the anatomical IMF).

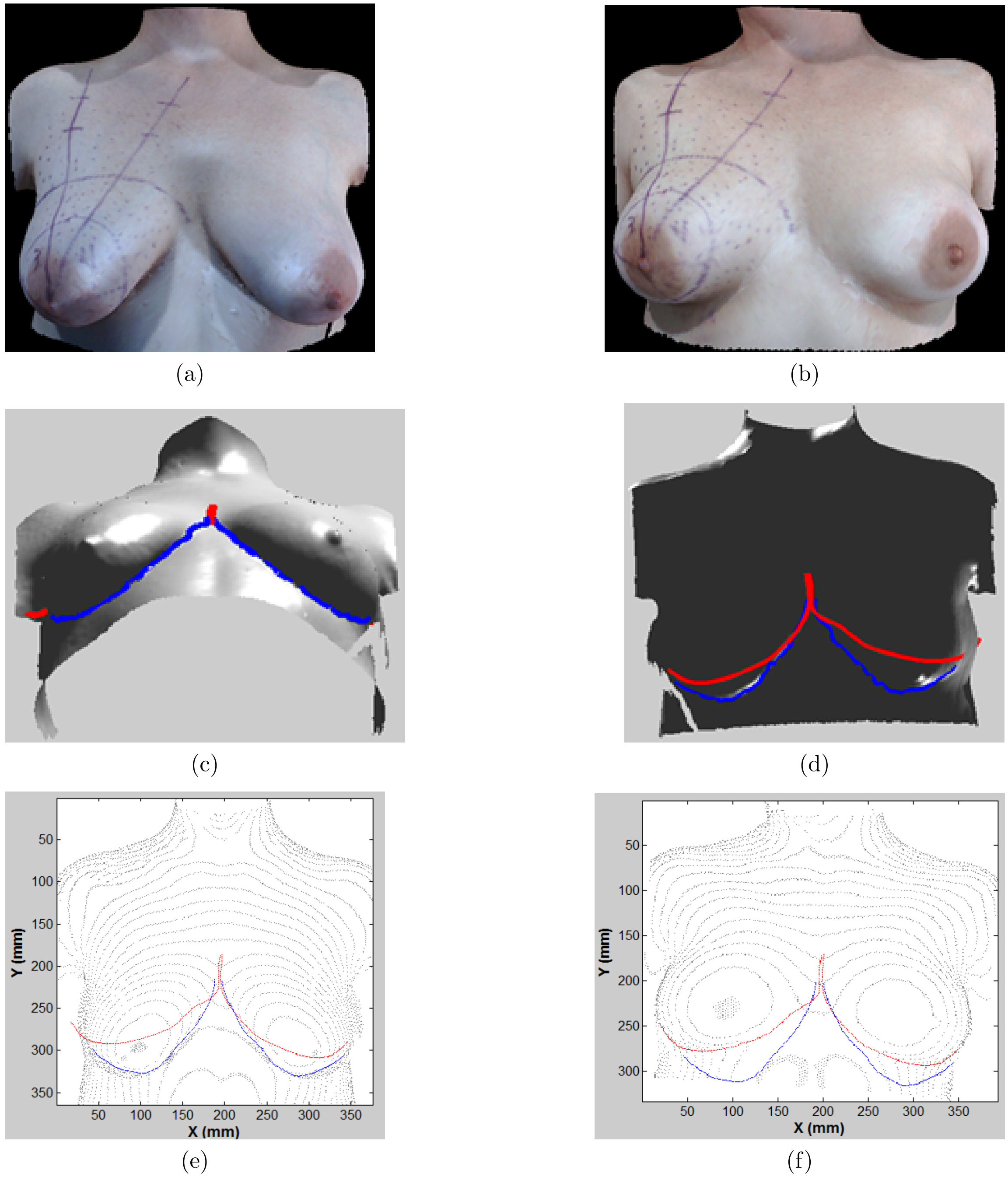


Figure 6.7: Subject with moderate ptosis (Grade 2). (a) 3D image in the upright position. (b) 3D image in the supine position. (c) The detected lowest breast contours displayed in the upright image (front). (d) The detected lowest breast contours displayed in the upright image (back). (e) 2D projection of detected contours displayed on fingerprint projection of the upright image. (f) 2D projection of detected contours displayed on fingerprint projection of the supine image. Blue lines represent the lowest breast contours detected in the upright images, whereas red lines are the lowest breast contours detected from the supine image (i.e., the anatomical IMF).

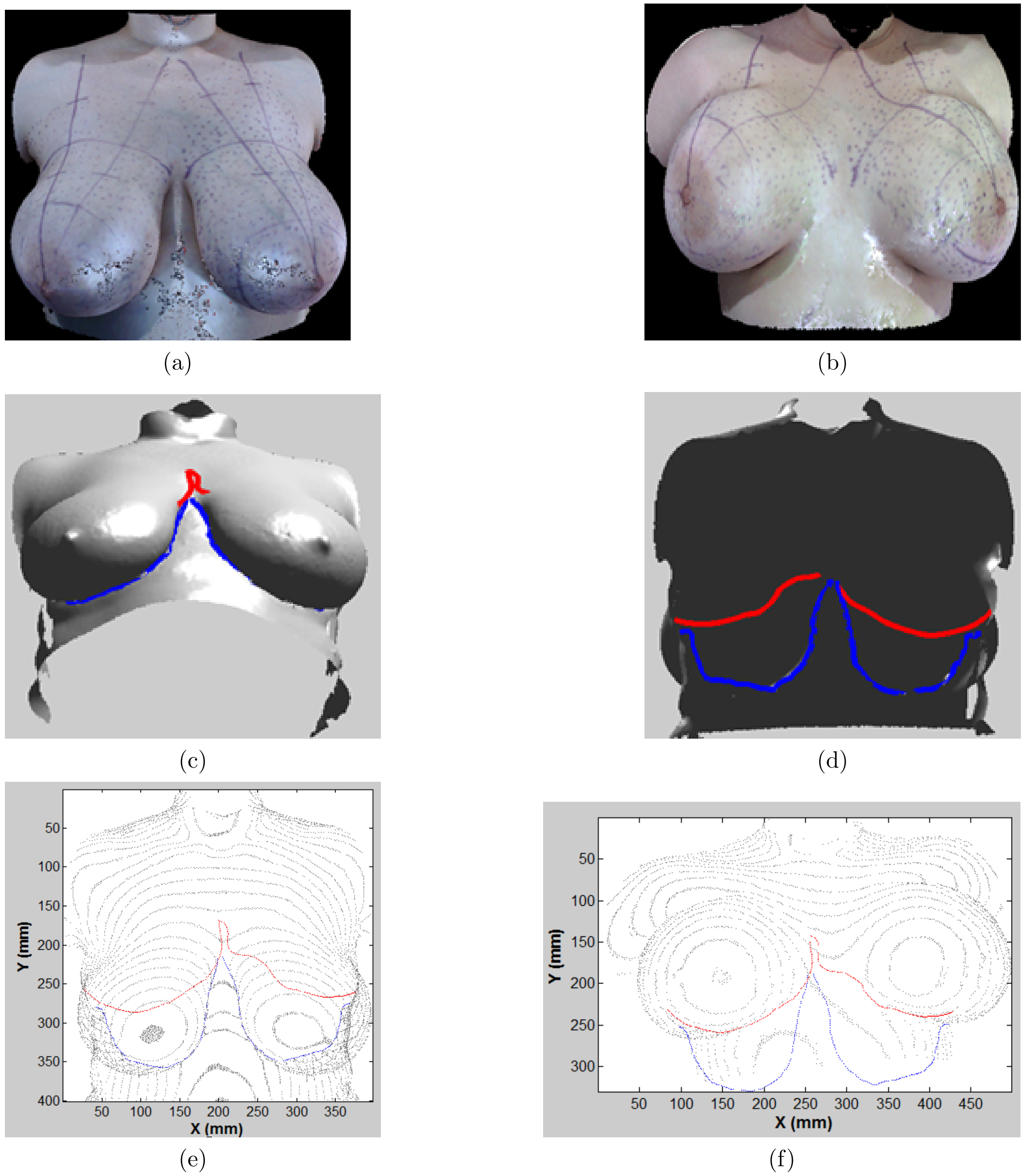


Figure 6.8: Another subject with moderate ptosis (Grade 2). (a) 3D image in the upright position. (b) 3D image in the supine position. (c) The detected lowest breast contours displayed in the upright image (front). (d) The detected lowest breast contours displayed in the upright image (back). (e) 2D projection of detected contours displayed on fingerprint projection of the upright image. (f) 2D projection of detected contours displayed on fingerprint projection of the supine image. Blue lines represent the lowest breast contours detected in the upright images, whereas red lines are the lowest breast contours detected from the supine image (i.e., the anatomical IMF).

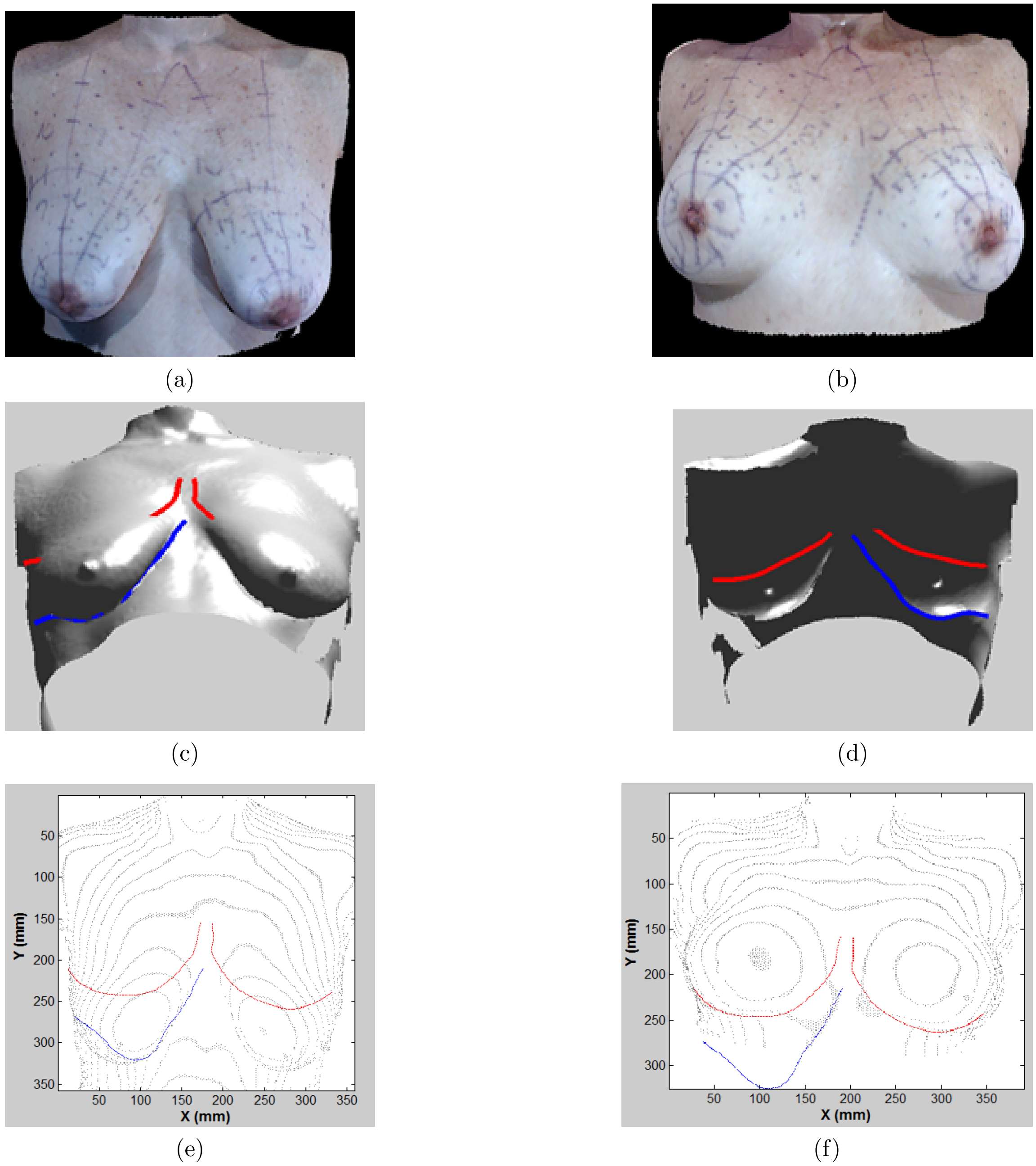


Figure 6.9: Subject with high ptosis (Grade 3). (a) 3D image in the upright position. (b) 3D image in the supine position. (c) The detected lowest breast contours displayed in the upright image (front). (d) The detected lowest breast contours displayed in the upright image (back). (e) 2D projection of detected contours displayed on fingerprint projection of the upright image. (f) 2D projection of detected contours displayed on fingerprint projection of the supine image. Blue lines represent the lowest breast contours detected in the upright images, whereas red lines are the lowest breast contours detected from the supine image (i.e., the anatomical IMF). The lowest contour of left breast for upright image is missed due to data missing on this area.

# Chapter 7

# Summary and Future Work

## 7.1 Summary

The long-term goal of this work is to develop algorithms to facilitate quantitative and objective measures of aesthetic outcomes with high reliability, thereby providing critical information for pre-operative planning and post-operative aesthetic evaluation of outcomes in breast reconstruction.

In Chapter 2, we reviewed the literature on the various breast aesthetics outcome assessment methods currently used: subjective ratings by human observers; physical measurements on the patient's body (anthropometry); measurements on 2D photographs (photogrammetry); measurements using $2\frac{1}{2}D$ images (depth-map) measurements using 3D images of the breasts (stereophotogrammetry); and measurements using other multi-dimensional imaging approaches.

In Chapter 3, we introduced the image acquisition technique: a custom-designed imaging system which is composed of two parts: 3dMDtorso$^{TM}$ Imaging System and

Tri W-G TG2732 bariatric motorized tilt table. The tilt table is mounted to enable acquisition of 3D images of the patients breasts in a range of positions from standing upright to supine, and any reclining angles in between. Thus we can acquire the multiple-visit images and multi-view images (upright and supine positions) used in this project.

In Chapter 4, we proposed a rigid registration algorithm of 3D images from multiple clinical visits for the same patient. Two fiducial points, SN and UM are manually identified as two control points and other thirteen control points are automatically selected based on the location of SN and UM. To overcome operator bias caused by manual fiducial points selection and location change of UM between multiple-visit images caused by breast reconstruction surgery, we optimize the registration of the SN and UM by searching for the most optimal corresponding points between two images. The average root mean squared (RMS) error of our proposed algorithm is $2.3611mm$ for the 83 registrations for the multiple-visit images from 34 patients. It outperforms an existing ICP algorithm with all of the three worst rejection rates 0 ($7.3860mm$), 30% ($4.7842mm$), and 60% ($7.7012mm$) for the same datasets. Our proposed algorithm also shows robustness across a range of patient BMI's.

In Chapter 5, we developed a curvature-based lowest breast contour detection algorithm for 3D images of the female torso. Our approach employs shape index and the minimum principle curvature. For the 151 breasts which include breasts of ptosis grades 0, 1, 2, 3 and breasts unrated for ptosis due to the absence of a surgically extracted nipple. The mean of the average distances between automatically detected contours and the ground truth (manually selected contours) is $1.642mm$. The breasts with nipples and rated as ptosis grades 0, 1, 2, and 3 by surgeons, include pre-operative natural breasts, have previous surgeries such as mastopexy, reduction, partial mastectomy, implant, flap, and combination of implant and flap. Unrated breasts without nipples from incomplete implant or flap surgeries include four intermediate stages of surgeries: (1) stage 0: had mastectomy, no reconstruction; (2) stage 1: had tissue expander placement or flap procedure; (3) stage 2: had exchange procedure for either implant or flap; (4) stage 3: completed revision surgeries.

In Chapter 6, we described an application of the registration algorithm and the lowest breast contour detection algorithm as a multi-view 3D data fusion technique for visualization of the IMF in upright images from women with ptotic breasts. We detect the lowest breast contour algorithm in both the upright and supine images and register these two images. The transformation parameters obtained from registration are employed to superimpose the detected lowest breast contour from the supine image onto the upright image. The anatomical IMF is visible and coincides with the lowest breast contour in the supine position for breasts which are ptotic in the upright position. Thus the fusion technique enables visualization of the anatomical IMF position for ptotic breasts in the upright images.

## 7.2 Future Work

A system for objective assessment of breast aesthetics is critical in order for breast cancer survivors and surgeons to make right decisions for different reconstructive procedures. We have developed algorithm to register 3D images from multiple clinical visits for same patients, and that to detect lowest breast contours from 3D images for women. However, substantial future work is needed to fully quantitatively understand breast outcomes and provide objective data to breast cancer survivors and surgeons.

Current quantitative assessments of breast morphology provide a global evaluation of breast morphology at a given time point such as breast ptosis, breast symmetry, and breast volume. But few works are available to correlate local morphological changes in breast over time, which is valuable to better assess the surgical outcomes. Future work will focus on comparing changes in breast morphology occurring during the time course of several reconstructive procedures. With the help of our multiple-visit images registration algorithm and lowest breast contour detection algorithm, and further designed algorithms, we can longitudinally analyze the local morphological breast changes in different surgery stages for the same patient, and compare intra- and inter-patient surgical outcomes, and across various surgery types.

# Bibliography


[1] J. I. Bostwick. *Plastic and reconstructive breast surgery*. Quality Medical Publishing, Inc., St. Louis, Missouri, 1999.

[2] L. R. Rubin, A. Klassen, S. J. Cano, K. Hurley, and A. L. Pusic. Motivations for breast surgery: A qualitative comparison study of breast reconstruction, augmentation, and reduction patients. *The Breast Journal*, 15(6):666–667, 2009.

[3] M. Eric, N. Mihic, and D. Krivokuca. Breast reconstruction following mastectomy; patient's satisfaction. *Acta Chirurgica Belgica*, 109(3):159–166, 2009.

[4] K. H. Breuing and S. M. Warren. Immediate bilateral breast reconstruction with implants and inferolateral alloderm slings. *Annals of Plastic Surgery*, 55(1):232–239, 2005.

[5] C. A. Salzberg. Nonexpansive immediate breast reconstruction using human acellular tissue matrix graft. *Annals of Plastic Surgery*, 57(1):1–5, 2006.

[6] S. S. Kroll, M. A. Schusterman, G. P. Reece, M. J. Miller, G. R. Evans, G. L. Robb, and B. J. Baldwin. Choice of flap and incidence of free flap success. *Plastic and Reconstructive Surgery*, 98(3):459–463, 1996.

[7] D. Chen, D. R. Chittajallu, G. Passalis, and I. A. Kakadiaris. Computational tools for quantitative breast morphometry based on 3d scans. *Annals of Biomedical Engineering*, 38(5):1703–1718, 2010.

[8] M. S. Kim, G. P. Reece, E. K. Beahm, M. J. Miller, N. Atkinson, and M. K. Markey. Objective assessment of aesthetic outcomes of breast cancer treatment: measuring ptosis from clinical photographs. *Annals of Biomedical Engineering*, 37(1):49–59, 2007.

[9] A. Losken, I. Fishman, D. D. Denson, H. R. Moyer, and G. W. Carlson. An objective evaluation of breast symmetry and shape differences using 3-dimensional images. *Annals of Plastic Surgery*, 55(6):571–575, 2005.

[10] M. Kawale, J. Lee, S. Y. Leung, M. C. Fingeret, G. P. Reece, M. A. Crosby, E. K. Beahm, M. K. Markey, and F. A. Merchant. 3d symmetry measure invariant to subject pose during image acquisition. *Breast Cancer: Basic and Clinical Research*, 5:131–142, 2011.

[11] L. Kovacs, M. Eder, R. Hollweck, A. Zimmermann, M. Settles, A. Schneider, K. Udosic, K. Schwenzer-Zimmerer, N. A. Papadopulos, and E. Biemer. New aspects of breast volume measurement using 3-dimensional surface imaging. *Annals of Plastic Surgery*, 57(6):602–610, 2006.

[12] C. W. Loughry, D. B. Sheffer, T. E. Price, R. L. Einsporn, Jr., R. G. Bartfai, W. M. Morek, and N. M. Meil. Breast volume measurement of 598 women using biostereometric analysis. *Ann. Plast Surg.*, 22:380–385, 1989.

[13] A. Edsander-Nord, M. Wickman, and G. Jurell. Measurement of breast volume with thermoplastic casts. *Scan. J. Plast. Reconstr. Surg. Hand Surg.*, 30:129–132, 1996.

[14] E. Tezel and A. Numanoglu. Practical do-it-yourself device for accurate volume measurement of breast. *Plastic and Reconstructive Surgery*, 105:1019–1023, 2000.

[15] M. Mineyev, D. Kramer, L. Kaufman, J. Carlson, and S. Frankel. Measurement of breast implant volume with magnetic resonance imaging. *Ann. Plast. Surg.*, 34:348–351, 1995.

[16] C. L. Kalbhen, J. J. McGill, P. M. Fendley, K. W. Corrigan, and J. Angelats. Mammographic determination of breast volume: comparing different methods. *American Journal of Roentgenology*, 173:1643–1649, 1999.

[17] G. Passalis, T. Theoharis, M. Miller, and I.A. Kakadiaris. Non-invasive automatic breast volume estimation for post-mastectomy breast reconstructive surgery. In *The 25th Annual lnternational Conference of the IEEE EMBS*, volume 2, pages 1319–1322, Cancun, Mexico, September 2003.

[18] 3dMD. 3dmdtorso system. `http://www.3dmd.com/3dMDtorso/`, 2014.

[19] L. Kovacs, M. Eder, R. Hollweck, A. Zimmermann, M. Settles, A. Schneider, K. Udosic, K. Schwenzer-Zimmerer, N. Papadopulos, and E. Biemer. New aspects of breast volume measurement using 3-dimensional surface imaging. *Annals of Plastic Surgery*, 57(6):602–610, 2006.

[20] A. Losken, H. Seify, D. Denson, A. Paredes, and G. Carlson. Validating three-dimensional imaging of the breast. *Annals of Plastic Surgery*, 54(5):471–476, 2005.

[21] Breastcancer.org. What is mastectomy? http://www.breastcancer.org/treatment/surgery/mastectomy/what_is, 2014.

[22] Allison W. Kurian, Daphne Y. Lichtensztajn, Theresa H. M. Keegan, David O. Nelson, Christina A. Clarke, and Scarlett L. Gomez. Use of and mortality after bilateral mastectomy compared with other surgical treatments for breast cancer in california, 1998-2011. *The Journal of the American Medical Association*, 312(9):902–914, 2014.

[23] Bernd Gerber, Annette Krause, Toralf Reimer, Heiner Mller, Ingrid Kchenmeister, Joseph Makovitzky, Gnther Kundt, and Klaus Friese. Skin-sparing mastectomy with conservation of the nippleareola complex and autologous reconstruction is an oncologically safe procedure. *Annals of Surgery*, 238(1):120–127, 2003.

[24] WebMD. Preventive mastectomy for breast cancer. http://www.webmd.com/breast-cancer/guide/preventive-mastectomy, 2014.

[25] Anne F. Klassen, Andrea L. Pusic, Amie Scott, Jennifer Klok, and Stefan J. Cano. Satisfaction and quality of life in women who undergo breast surgery: A qualitative study. *BMC Womens Health*, 9(11), 2009.

[26] P. Ananthakrishnan and A. Lucas. Options and considerations in the timing of breast reconstruction after mastectomy. *Cleveland Clinic Journal of Medicine*, 75(S1):30–33, 2008.

[27] American Cancer Society. Breast reconstruction after mastectomy. http://www.cancer.org/acs/groups/cid/documents/webcontent/002992-pdf.pdf.

[28] U. Ahcan, D. Bracun, K. Zivec, R. Pavlic, and P. Butala. The use of 3d laser imaging and a new breast replica cast as a method to optimize autologous breast reconstruction after mastectomy. *Breast*, 12(2):183–189, 2012.

[29] G. M. Galdino, M. Nahabedian, M. Chiaramonte, J. Z. Geng, S. Klatsky, and P. Manson. Clinical applications of three-dimensional photography in breast surgery. *Plast. Reconstr. Surg.*, 110(1):58–70, 2002.

[30] G. Catanuto, A. Spano, A. Pennati, E. Riggio, G. M. Farinella, G. Impoco, S. Spoto, G. Gallo, and M. B. Nava. Experimental methodology for digital breast shape analysis and objective surgical outcome evaluation. *J. Plast. Reconstr. Aesthet. Surg.*, 61(3):314–318, 2008.

[31] R. M. Goldwyn. *Plastic and reconstructive surgery of the breast.* Little Brown, Boston, 1976.

[32] L. Kovacs, A. Zimmermann, N. A. Papadopulos, and E. Biemer. Re: Factors determining shape and symmetry in immediate breast reconstruction. *Ann. Plast. Surg.*, 53:192–194, 2004.

[33] H. Henseler, J. Smith, A. Bowman, B. S. Khambay, X. Ju, A. Ayoub, and A. K. Ray. Subjective versus objective assessment of breast reconstruction. *Journal Of Plastic, Reconstructive And Aesthetic Surgery*, 65(9):1209–1215, 2012.

[34] M. S. Kim, J. C. Sbalchiero, G. P. Reece, and M. J. Miller. Assessment of breast aesthetics. *Plast. Reconstr. Surg.*, 121(1):186–194, 2008.

[35] K. C. Sneeuw, N. K. Aaronson, J. R. Yarnold, M. Broderick, J. Regan, G. Ross, and A. Goddard. Cosmetic and functional outcomes of breast conserving treatment for early stage breast cancer. 1. comparison of patients' ratings, observers' ratings, and objective assessments. *Radiother. Oncol.*, 25:153–159, 1992.

[36] M. Cohen, B. Evanoff, L. T. George, and K. E. Brandt. A subjective rating scale for evaluating the appearance outcome of autologous breast reconstruction. *Plastic and Reconstructive Surgery*, 116:440–449, 2005.

[37] Nicola Brown and Joanna Scurr. The need for a standardised anthropometric protocol for objective assessment of pre- and postoperative breast surgery. *Gland Surgery*, 1(3):142–145, 2012.

[38] J. Penn. Breast reduction. *Br. J. Plast. Surg.*, 7(4):357–371, 1955.

[39] Melvyn Westreich. *Breast Augmentation*, chapter 3, pages 27–44. Springer Berlin Heidelberg, 2009.

[40] D. K. Avar, A. C. Aygit, E. Benlier, H. Top, and O. Takinalp. Anthropometric breast measurement: a study of 385 turkish female students. *Aesthet. Surg. J.*, 30(1):44–50, 2010.

[41] Y. J. Liu and J. G. Thomson. Ideal anthropomorphic values of the female breast: correlation of pluralistic aesthetic evaluations with objective measurements. *Ann. Plast. Surg.*, 67:7–11, 2011.

[42] E. Van Limbergen, E. van der Schueren, and K. Van Tongelen. Cosmetic evaluation of breast conserving treatment for mammary cancer. 1. proposal of a quantitative scoring system. *Radiother. Oncol.*, 16:159–167, 1989.

[43] H. P. Oliveira, P. Patete, G. Baroni, and J. S. Cardoso. Development of a bcct quantitative 3d evaluation system through low-cost solutions. In *The 2nd International Conference on 3D Body Scanning Technologies*, pages 16–27, Lugano, Switzerland, October 2011. Hometrica Consulting, Switzerland.

[44] M. D. Silva, H. P. Oliveira, and J. S. Cardoso. Super-resolution on depth-map images. In *The 1st PhD. Students Conference in Electrical and Computer Engineering*, pages 1–2, Porto, Portugal, June 2012.

[45] H. P. Oliveira, M. D. Silva, A. Magalhes, M. J. Cardoso, and J. S. Cardoso. Is kinect depth data accurate for the aesthetic evaluation after breast cancer surgeries? *Lecture Notes in Computer Science*, 7887:261–268, 2013.

[46] H. P. Oliveira, J. S. Cardoso, A. Magalhaes, and M.J. Cardoso. Methods for the aesthetic evaluation of breast cancer conservation treatment: A technological review. *Medical Imaging Reviews*, 9(1):32–46, 2013.

[47] H. P. Oliveira, J. S. Cardoso, A. T. Magalhes, and Cardoso M.J. Depth-map images for the aesthetic evaluation of breast cancer treatment. In *The 1st PhD. Students Conference in Electrical and Computer Engineering*, pages 1–2, Porto, Portugal, June 2012.

[48] H. P. Oliveira, J. S. Cardoso, A. T. Magalhes, and Cardoso M.J. Simultaneous detection of prominent points on breast cancer conservative treatment images. In *19th IEEE International Conference on Image Processing*, pages 2841–2844, Orlando, FL, September 2012.

[49] M. Alexandre and D. Silva. Kinect based system applied to breast cancer conservative treatment. Master's thesis, Universidade do Porto, February 2012.

[50] L. Kovacs, A. Zimmermann, N. A. Papadopulos, and E. Biemer. Re: Factors determining shape and symmetry in immediate breast reconstruction. *Ann. Plast. Surg.*, 53:192–194, 2004.

[51] M. Y. Nahabedian. Invited discussion: validating three-dimensional imaging of the breast. *Ann. Plast. Surg.*, 54:477–478, 2005.

[52] C. N. Creasman, D. Mordaunt, T. Liolios, C. Chiu, A. Gabriel, and G. P. Maxwell. Four-dimensional breast imaging, part i: introduction of a technology-driven, evidence-based approach to breast augmentation planning. *Aesthet. Surg. J.*, 31(8):914–924, 2011.

[53] Craig N. Creasman, David Mordaunt, Tom Liolios, Catherine Chiu, Allen Gabriel, and G Patrick Maxwell. Four-dimensional breast imaging, part ii: clinical implementation and validation of a computer imaging system for breast augmentation planning. *Aesthet. Surg. J.*, 31(8):925–938, 2011.

[54] A. Gabriel, S. Fritzsche, C. Creasman, W. Baqai, D. Mordaunt, and G. P. Maxwell. Incidence of breast and chest wall asymmetries: 4d photography. *Aesthet. Surg. J.*, 31(5):506–510, 2011.

[55] A. Losken. Commentary on: Four-dimensional breast imaging, parts i and ii. *Aesthet. Surg. J.*, 31(8):939–940, 2011.

[56] Hongliang Yu. *Automatic Rigid and Deformable Medical Image Registration.* PhD thesis, WORCESTER POLYTECHNIC INSTITUTE, May 2005.

[57] M. V. Wyawahare, P. M. Patil, and H. K. Abhyankar. Image registration techniques: an overview. *International Journal of Signal Processing, Image Processing and Pattern Recognition*, 2(5):11–28, 2009.

[58] G. K. L. Tam, Z. Q. Cheng, Y. K. Lai, F. C. Langbein, Y. Liu, D. Marshall, R. R. Martin, X. Sun, and P. L. Rosin. Registration of 3d point clouds and meshes: A survey from rigid to non-rigid. *IEEE Trans. Vis. Comput. Graph*, 19(7):1199–1217, 2013.

[59] P. J. Besl, N. D. McKay, and N. Yokoya. A method for registration of 3-d shapes. *IEEE Trans. Pattern Analysis and Machine intelligence*, 14(2):239–256, 1992.

[60] G. Blais and M. D. Levine. Registering multiview range data to create 3d computer objects. *IEEE Trans. Pattern Analysis and Machine Intelligence*, 17(8):820–824, 1995.

[61] T. Masuda and N. Yokoya. A robust method for registration and segmentation of multiple range images. *Computer Vision and Image Understanding*, 61(3):295–307, 1995.

[62] C. Dorai, G. Wang, A. K. Jain, and C. Mercer. Registration and integration of multiple object views for 3d model construction. *IEEE Trans, Pattern Anal. Machine Intelligence*, 20(1):83–89, 1998.

[63] K. Masuda, T. Sakaue and N. Yokoya. Registration and integration of multiple range images for 3d model construction. In *The 13th International Conf. on Pattern Recognition*, volume 1, pages 879–883, Vienna, Austria, August 1996.

[64] Y. Sun, J. Paik, A. Koschan, D. Page, and M. Abidi. Point fingerprint: a new 3-d object representation scheme. *IEEE Transactions on Systems, Man and Cybernetics*, 33(4):712–717, 2003.

[65] G. Zou, J. Hua, M. Dong, and H. Qin. Surface matching with salient keypoints in geodesic scale space. *Journal of Computer Animation and Virtual Worlds*, 19:399–410, 2008.

[66] P. Wen. Medical image registration based-on points, contour and curves. In *International Conference on Biomedical Engineering and Informatics*, pages 132–136, Sanya, Hainan, China, May 2008.

[67] S. D. Fox and D. M. Lyons. An approach to stereo-point cloud registration using image homographies. In *SPIE Conf. on Intelligent Robots and Computer Vision XXVII: Algorithms and Techniques*, volume 8301, San Francisco, CA, January 2012.

[68] F. Boughorbel, A. Koschan, B. Abidi, and M. Abidi. Gaussian fields: a new criterion for 3d rigid registration. *Pattern Recognition*, 37(7):1567–1571, 2004.

[69] F. Boughorbel, A. Koschan, B. Abidi, and M. Abidi. Gaussian energy functions for registration without correspondences. In *The 17th International Conf. on Pattern Recognition*, volume 3, pages 24–27, Cambridge, UK, August 2004.

[70] F. Boughorbel. Automatic registration of 3d datasets using gaussian fields. In *IEEE International Conference on Image Processing*, pages 804–807, Genoa, Italy, September 2005.

[71] F. Boughorbel, M. Mercimek, A. Koschan, and M. Abidi. A new method for the registration of three-dimensional point-sets: The gaussian fields framework. *Image and Vision Computing*, 28(1):124–137, January 2010.

[72] G. Li, H. Kim, J. K. Tan, and S. Ishikawa. Surface orientation driven 3d rigid registration method. In *IEEE International Conf. on Systems, Man, and Cybernetics*, pages 1418–1421, Seoul, Korea, October 2012.

[73] L. Zhao, S. K. Shah, G. P. Reece, M. A. Crosby, E. K. Beahm, M. C. Fingeret, M. K. Markey, and F. A. Merchant. Semi-automated registration of 3d torso images from breast reconstruction surgery. In *The 3rd International Conf. on 3D Body Scanning Technologies*, pages 179–188, Lugano, Switzerland, October 2012.

[74] P. W. Josien, J. B. Pluim, and M. A. Viergever. Mutual information based registration of medical images: a survey. *IEEE Transactions on Medical Imaging*, 22(8):986–1004, August 2003.

[75] C. Machover. Computer graphics pioneers: the gilois school of computer graphics. *ACM Computer Graphics*, 35(4):12–16, November 2001.

[76] H. Kjer and J. Wilm. Evaluation of surface registration algorithms for pet motion correction, June 2010.

[77] J. Lee, M. Kawale, F. Merchant, J. Weston, M. Fingeret, D. Ladewig, G. P. Reece, M. A. Crosby, E. K. Beahm, and M. K. Markey. Validation of stereophotogrammetry of the human torso. *Breast Cancer*, 5:15–25, 2011.

[78] H. Mirzaalian, M. R. Ahmadzadeh, and F. Kolahdoozan. Breast contour detection on digital mammogram. In *Proceedings of the Information and Communication Technologies (ICTTA '06)*, pages 1804 – 1808, Damascus, Syria, April 2006. IEEE.

[79] J. S. Cardoso, L. F. Teixeira, and M. J. Cardoso. Automatic breast contour detection in digital photographs. In *Proceedings of International Conference on Health Informatics*, volume 2, pages 91–98, Funchal, Madeira, Portugal, 2008. INSTICC - Institute for Systems and Technologies of Information, Control and Communication.

[80] J. S. Cardoso, R. Sousa, L. F. Teixeira, and M. J. Cardoso. Breast contour detection with stable paths. In *Biomedical Engineering Systems and Technologies, International Joint Conference*, volume 25, pages 439–452, Funchal, Madeira, Portugal, 2008. Springer.

[81] H.P. Oliveira, J.S. Cardoso, A. Magalhes, and Cardoso M.J. Depth-map images for the aesthetic evaluation of breast cancer treatment. In *Proceedings of the 1st PhD. Students Conference in Electrical and Computer Engineering*, pages 1–2, Porto, Portugal, 2012.

[82] H. P. Oliveira, J. S. Cardoso, T. Magalhes, and J. S. Cardoso. Simultaneous detection of prominent points on breast cancer conservative treatment images. In *19th IEEE International Conference on Image Processing*, pages 2841–2844, Orlando, Florida, 2012.

[83] J. Lee, S. Chen, G. P. Reece, M. A. Crosby, E. K. Beahm, and M. K. Markey. A novel quantitative measure of breast curvature based on catenary. *IEEE Transactions on Biomedical Engineering*, 59(4):1115–1124, 2012.

[84] J. Lee, G. S. Muralidhar, G. P. Reece, and M. K. Markey. A shape constrained parametric active contour model for breast contour detection. In *Engineering in Medicine and Biology Society, Proceedings of the 34th Annual International Conference of the IEEE*, pages 4450–4453, San Diego, California, 2012.

[85] J. Lee, G. P. Reece, and M. K. Markey. Breast curvature of the upper and lower breast mound: 3d analysis of patients who underwent breast reconstruction. In *3rd International Conference on 3D Body Scanning Technologies*, pages 171–179, Lugano, Switzerland, 2012.

[86] L. Zhao, G. P. Reece, M. C. Fingeret, and F. A. Merchant. Multi-view 3d data fusion for visualization of the inframammary fold in women with ptotic breasts. In *Proc. of 5th International Conference on 3D Body Scanning Technologies*, pages 29–38, Lugano, Switzerland, 2014.

[87] H. Cantzler and R. B. Fisher. Comparison of hk and sc curvature description methods. In *Proc. of 3rd International Conference on 3-D Digital Imaging and Modelling*, pages 285–291, Quebec City, Canada, 2001.

[88] Gabriel Peyre. Toolbox graph. `http://www.mathworks.com/matlabcentral/fileexchange/5355-toolbox-graph`, 2013.

[89] D. Cohen-Steiner and M. Jean-Marie. Restricted delaunay triangulations and normal cycle. In *Proceedings of the nineteenth Conference on Computational Geometry*, pages 237–246, New York, 2003.

[90] P. Alliez, D. Cohen-Steiner, M. Desburn, O. Devillers, and B. Levy. Anisotropic polygonal remeshing. *ACM Transactions on Graphics*, 22(3):485–493, 2003.

[91] M. Murguia and J. L. Villasenor. Estimating the effect of the similarity coefficient and the cluster algorithm on biogeographic classifications. *Annales Botanici Fennici*, 40(6):415–421, 2003.

[92] C. D. Muntan, M. J. Sundine, R. D. Rink, and R. D. Acland. Inframammary fold: A histologic reappraisal. *Plastic and Reconstructive Surgery*, 105(2):549–556, 2000.

[93] G. P. Gui, K. A. Behranwala, N. Abdullah, J. Seet, P. Osin, A. Nerurkar, and S. R. Lakhani. The inframammary fold: Contents, clinical significance and implications for immediate breast reconstruction. *British Journal of Plastic Surgery*, 57(2):146–149, 2004.

[94] M. S. Kim, G. P. Reece, E. K. Beahm, M. J. Miller, E. N. Atkinson, and M. K. Markeyemail. Objective assessment of aesthetic outcomes of breast cancer treatment: Measuring ptosis from clinical photographs. *Computers in Biology and Medicine*, 37(1):49–59, 2007.

[95] Y. J. Liu. Aesthetics of the female breast: Correlation of pluralistic evaluations with volume and surface area. *Yale Journal of Biology and Medicine*, 82(4):181–229, 2009.

[96] C. N. Creasman, D. Mordaunt, T. Liolios, C. Chiu, A. Gabriel, and G. P. Maxwell. Four-dimensional breast imaging, part i: Introduction of a technology-driven, evidence-based approach to breast augmentation planning. *Aesthetic Surgery Journal*, 31(8):914–924, 2011.

[97] M. Eder, M. Klppel, D. Mller, N. A. Papadopulos, H. G. Machens, and L. Kovacs. 3-d analysis of breast morphology changes after inverted t-scar and vertical-scar reduction mammaplasty over 12 months. *Journal of Plastic, Reconstructive & Aesthetic Surgery*, 66(6):776–786, 2013.

[98] L. Kovacs, M. Eder, R. Hollweck, A. Zimmermann, M. Settles, A. Schneider, M. Endlich, A. Mueller, K. Schwenzer-Zimmerer, N. A. Papadopulos, and E. Biemer. Comparison between breast volume measurement using 3d surface imaging and classical techniques. *Breast*, 16(2):137–145, 2007.

[99] C. N. Creasman, D. Mordaunt, T. Liolios, C. Chiu, A. Gabriel, and G. P. Maxwell. Four-dimensional breast imaging, part ii : Clinical implementation

and validation of a computer imaging system for breast augmentation planning. *Aesthetic Surgery Journal*, 31(8):925–938, 2011.

[100] Y. J. Liu and J. G. Thomson. Ideal anthropomorphic values of the female breast correlation of pluralistic aesthetic evaluations with objective measurements. *Annals of plastic surgery*, 67(1):7–11, 2011.

[101] L. Kovacs, M. Eder, A. Zimmermann, D. Mller, T. Schuster, N. A. Papadopulos, E. Biemer, M. Klppel, and H. G. Machens. Three-dimensional evaluation of breast augmentation and the influence of anatomic and round implants on operative breast shape changes. *Aesthetic Plastic Surgery*, 36(4):879–887, 2012.

[102] M. Eder, F. V. Waldenfels, M. Sichtermann, T. Schuster, N. A. Papadopulos, H. G. Machens, E. Biemer, and L. Kovacs. Three-dimensional evaluation of breast contour and volume changes following subpectoral augmentation mammaplasty over 6 months. *Journal of Plastic, Reconstructive & Aesthetic Surgery*, 64(9):1152–1160, 2011.

[103] J. Lee, M. Kawale, F. A. Merchant, J. Weston, M. C. Fingeret, D. Ladewig, G. P. Reece, M. A. Crosby, E. K. Beahm, and M. K. Markey. Validation of stereophotogrammetry of the human torso. *Breast cancer: basic and clinical research*, 5:15–25, 2011.

[104] B. S. Atiyeh, S. A. Dibo, M. Nader, and N. J. Papazian. Preoperative assessment tool for the planning of inframammary incision and implant profile in breast augmentation. *Aesthetic Plastic Surgery*, 38(5):878–886, 2014.